The Thesis Committee for Brandon Jamal Tripp
Certifies that this is the approved version of the following thesis:

Dependence of Transport Properties on Grain Size Distribution

APPROVED BY
SUPERVISING COMMITTEE:

Supervisor:

Hugh Daigle

Maša Prodanović

Dependence of Transport Properties on Grain Size Distribution

by

Brandon Jamal Tripp, B.S.C.E.

Thesis

Presented to the Faculty of the Graduate School of

The University of Texas at Austin

in Partial Fulfillment

of the Requirements

for the Degree of

Master of Science in Engineering

The University of Texas at Austin

December 2016

Acknowledgements

The journey towards the completion of my masters of science degree was a fulfilling and rewarding experience that required the support of many for one individual to succeed. As the journey concludes, I am able to reflect on the challenges, successes, and a multitude of experiences that I am unable to compile into words. Nonetheless, I am fortunate to have traveled the path that I have chosen to follow and I look forward to the adventures of the future.

I would like to acknowledge my thesis advisor Dr. Hugh Daigle who provided financial support to fund the completion of my education. Furthermore, Dr. Daigle provided me with the flexibility to select between research topics that galvanized my heart and fostered my growth in the industry.

I would like to acknowledge Dr. Matthew Balhoff for introducing me to The University of Texas at Austin and allowing me the opportunity network with multiple professors and students. Additionally, I would like to thank Dr. Bahoff, for his continued support, advice, and words of encouragement as I completed my graduate degree and research.

I would like to acknowledge Dr. Maša Prodanović for providing her guidance and insight as the second reader of my thesis report; I am grateful for Dr. Prodanović's time and comments as I completed my research document.

I would like to provide special acknowledgements to Dr. Behzad Ghanbarian. Dr. Ghanbarian provided continued support and guidance as I completed my thesis research; in addition to the tangibles, Dr. Ghanbarian maintained an open door policy throughout my graduate research and provided me with continued motivation. Dr. Ghanbarian

challenged me and ensured my development as I completed my research project; Dr. Ghanbarian was an invaluable asset throughout my graduate career.

Lastly, I would like to acknowledge the Texas Advanced Computing Center (TACC); TACC enabled me to complete multiple permeability simulations simultaneously for my thesis research.

Abstract

Dependence of Transport Properties on Grain Size Distribution

Brandon Jamal Tripp, M.S.E.

The University of Texas at Austin, 2016

Supervisor: Hugh Daigle

The topic of this thesis is investigating the relationship between grain size distribution and absolute permeability for medium silt to very fine-grained sandstones that are typical reservoir rocks in deepwater, offshore environments. I analyzed the relationship between grain size, mean grain size, median grain size, and grain size mode; grain size standard deviation; and absolute permeability through the amalgamation of numerical modeling and experimental core data for marine clay from the Pacific Ocean and Gulf of Alaska. The Pacific Ocean core sample was selected to represent porous media exhibiting narrow grain size distributions; the Gulf of Alaska samples were selected to represent porous media exhibiting broad grain size distributions. I constructed porous media composed of random packings of spheres with grain size distributions modeled on the grain size distribution of the Pacific Ocean core, and determined permeability by performing Lattice-Boltzmann simulations. The narrow grain size distributions exhibited a power law relationship between grain size standard deviation and permeability relationship. I then compared these results to measured data on the Gulf of Alaska samples, which exhibited very broad grain size distributions. The Gulf of

Alaska samples had a different relationship between permeability and the standard deviation of the grain size distribution, although the relationship was still a power law. This illustrates how the breadth of the grain size distribution must be considered in empirical permeability relationships.

Table of Contents

List of Tables

List of Figures

List of Illustrations

1. Introduction

To meet the increasing global energy demand, knowledge of transport properties, such as permeability, is essential to predict behavior of global oil and natural gas reservoirs. Permeability is a secondary property of sedimentary reservoir rocks influenced by primary reservoir rock properties – grain shape, grain size, grain orientation, packing and sorting – in addition to the defined primary reservoir properties, permeability is influenced by pore volume connectivity (Berg, 1986). Permeability defines the flow regimes, bilinear, early linear, early elliptical/pseudoradial, fracture interference, and compound linear, for conventional and unconventional oil and natural gas reservoirs; as a result, permeability defines the reservoir volume element. Researchers have presented multiple empirical, quasi-empirical, and physically-based models to determine reservoir permeability; however, multiple models are extension of the semi-empirical Kozeny-Carman equation. Researchers use the Kozeny-Carman because of the model's simplicity; nonetheless, the Kozeny-Carman equation has multiple limitations. The Kozeny-Carman equation is not accurate for electrochemical reactions, flow velocity, particle shape, particle size distribution, and anisotropy. In addition to the limitations described, the modified Kozeny-Carman equation defines permeability utilizing a characteristic grain size, mean grain size, median grain size, or mode grain size; however, the characteristic grain is not representative of the variable grain sizes encompassed inside the porous medium. The motivations for the present research was to mitigate limitations, associated with prevalent permeability models (Background 2.2.1.2) and to define permeability as a function of the porous medium's grain size distribution. Mitigating the limitations associated with the Kozeny-Carman equation and defining permeability as a function of a porous medium's grain size distribution provides enhanced permeability estimates; furthermore, such a permeability model would more effectively represent the characteristics of the reservoir rock.

The defined research topic was proposed to analyze the relationship between grain size, mean grain size, median grain size, and grain size mode; grain size standard deviation; and absolute permeability through the amalgamation of numerical modeling and experimental core data for sediments from the Pacific Ocean and Gulf of Alaska. The Pacific Ocean mudstone core was selected to characterize porous media exhibiting narrow grain size distributions; the Gulf of Alaska samples were selected to characterize porous media exhibiting broad grain size distributions. The numerical models used to demonstrate porous media exhibiting narrow grain size distributions exhibited a power law relationship between standard deviation and permeability values; however, the analysis of standard deviation and permeability values did not exhibit a conclusive correlation between narrow and broad grain size distributions. The Pacific Ocean sample was extracted from an isolated segment of the Pacific Ocean very far from any sediment source; this resulted in a narrow grain size distribution with predominantly clay-sized particles. The Gulf of Alaska cores, on the other hand, consisted of glaciomarine sediments and exhibited very broad grain size distributions consisting of nearly equal parts sand-, silt-, and clay-sized particles. The numerical simulations used to demonstrate porous media exhibiting narrow grain size distributions exhibited a power law relationship between grain size standard deviation and permeability values; however, samples with broad grain size distributions did not exhibit a conclusive correlation between standard deviation and permeability values. Narrow and broad grain size distributions both exhibited power law porosity-permeability relationships. Standard deviation, permeability and porosity, permeability relationships exhibited similar power law relationships irrespective of the utilization of mean, median, or mode to determine permeability estimates.

2. Background

2.1 GEOLOGY

Sandstones are important topics of research discussion for geologists, petroleum engineers, and petrophysicists. Sandstone reservoirs contain approximately 50 percent of the world's oil and natural gas reserves (Berg, 1986). The understanding of the primary properties, composition, texture, stratification, and morphology, and secondary properties, porosity, permeability, fluid saturation, and bulk density, of sandstones are critical when analyzing a sandstone reservoir and predicting the reservoir's capacity for oil or natural gas production. Additional properties associated with hydrocarbon reservoirs are tertiary properties such as resistivity, spontaneous potential, radioactivity, and sonic travel time; geophysical logs measure tertiary properties (Berg, 1986). In this section I will provide additional detail about primary properties, secondary properties, and interrelationships between the two properties. Permeability is an essential property required to analyze the potential of hydrocarbon reservoirs to produce; however, permeability is often inferred through indirect downhole measurements. Therefore, understanding permeability's relationship with other properties is essential for accurate permeability prediction.

Primary properties are referred to as definitive properties because they provide the fundamental characteristics of the reservoir. Sandstone reservoirs are composed of mineral particles primarily consisting of quartz, feldspar, and different rock fragments; fractions of the pore space located between mineral particles are occupied with clay minerals, and very fine particles of feldspar and quartz. The mineral particles that compose sandstones can potentially represent a large standard deviation in reference to the mean particle size; the interrelationships among the mineral particles define the texture of the sandstone. The primary characteristics defining the texture of sandstones are grain size, orientation, packing, shape, and sorting (Berg, 1986). The layering, stratification, of a sandstone rock is the result of sedimentary processes and biological or

physical alterations after deposition. Typically, sandstone layering is produced by alterations between coarse and fine mineral particles; additionally, regular and irregular grain distributions produce layering. The final primary property of sandstone to be analyzed is morphology; morphology defines the breadth, shape, and size of a sandstone grain (Berg, 1986). The morphology of sandstone grains is used to estimate the reservoir volume and economic potential of a petroleum reservoir.

Secondary (dependent) properties are dependent on the primary properties (composition, texture, stratification, and morphology) of a reservoir. Porosity is an important secondary property that is defined as the ratio of pore volume to total volume of rock. The porosity of a porous medium depends on a magnitude of factors: chemical diagenetic processes, grain shape, grain size, packing, physical diagenetic processes, and sorting (Berg, 1986). Chemical and physical diagenetic processes have increasing and decreasing effects on the porosity of a porous medium. There are multiple different types of diagenetic processes. Diagenetic processes that increase the porosity of a porous medium include clay dehydration, dissolution, and microfracturing. Diagenetic processes that decrease the porosity of a porous medium include compaction, cementation, clay precipitation, and pressure solution (Berg, 1986). Cementation is a chemical diagenetic process that has a significant effect on sandstone reservoirs; specifically, quartz cementation is responsible for considerable porosity reduction in well-sorted, quartz-rich sandstones buried to depths exceeding 3,000 meters (Bjørlykke, 1993). The porosities of sandstone and shale sedimentary rocks vary with depth. Sandstones typically exhibit less porosity reduction with depth than shales (Berg, 1986). Reservoir sandstones are typically mixtures of quartz, clays, and other minerals; therefore, the porosity, depth relationship of the reservoir will be contained within the envelope of the intersecting sandstone and shale porosity-depth relationships.

The permeability of a porous medium quantifies the medium's fluid transmissibility; Henry Darcy published a relationship between flow rate and

permeability for the flow of water in sand packs (Darcy, 1856; Brown, 2002; Peters, 2012). Single-phase flow for a horizontal or vertical system can be defined by Equation 2.1 (Peters, 2012):

$$q = -\frac{kA}{\mu}\frac{dP}{dx}, \tag{2.1}$$

where q represents volumetric fluid flux, k represents permeability, A represents the cross-sectional area normal to the direction of flow, μ represents the fluid viscosity of the flowing fluid, and $\frac{dP}{dx}$ represents the pressure gradient along the length of the fluid flow path. The integration of Equation 2.1 provides the absolute permeability for single-phase, steady state linear flow of a fluid in a horizontal or vertical porous medium; the integration of Equation 2.1 results in the formulation of Equation 2.2:

$$qdx = -\frac{kA}{\mu}dP$$

$$\int_0^L qdx = \int_{P_1}^{P_2} -\frac{kA}{\mu}dP$$

$$qL = -\frac{kA}{\mu}(P_2 - P_1)$$

$$q = \frac{kA}{\mu}\frac{\Delta P}{L}$$

$$k = \frac{q\mu L}{A\Delta P}. \tag{2.2}$$

The absolute permeability of a fluid is defined as the permeability when a porous medium is completely saturated with a non-reactive, single-phase fluid (Peters, 2012). Permeability depends on the connectivity of the pore volume space; additionally, permeability is a function of grain shape, gain size, and matrix geometry (Berg, 1986).

The ability to estimate permeability from other more easily measured properties in contrast to direct measurements reduces capital expenditure for exploration and production projects.

2.2 Modeling Permeability in Porous Media

Permeability is a petrophysical property of substantial interest to multiple disciplines: hydrology, soil physics, geotechnical engineers, and petroleum engineers. Permeability is of significant importance to petroleum engineers because the parameter determines a reservoir's hydrocarbon producing potential for conventional oil and natural gas reservoirs and the effectiveness of enhanced oil recovery techniques. Because of the importance of permeability in many applications, researchers have examined multiple permeability correlations that can be categorized into broad categories: empirical, quasi-empirical, and physically-based models; processed based models; direct simulation models; and stochastic models.

2.2.1 Empirical, Quasi-empirical, and Physically-based Models

2.2.1.1 Hazen Equation

Hazen (1892, 1911) developed an empirical relationship for predicting the permeability of saturated sands depicted in Equation 2.3:

$$k = C_H D_{10}^2, \tag{2.3}$$

where C_H is the Hazen empirical coefficient and D_{10} is the diameter for the grain size distribution such that 10 percent of the particles are smaller than D_{10}. Hazen's permeability relationship was developed utilizing unconsolidated, clean sands exhibiting a uniformity coefficient less than approximately 2; the uniformity coefficient is defined in Equation 2.4:

$$C_U = \frac{D_{60}}{D_{10}}, \tag{2.4}$$

where D_{60} represents the grain diameter exhibiting 60 percent passing, and D_{10} represents the grain diameter exhibiting 10 percent passing. The Hazen empirical coefficient C_H is typically assumed to be equal to 100; however, multiple values for different soils have been reported in the literature:

- 41 to 46 (Taylor, 1948)
- 100 to 150 (Leonards, 1962)
- 100 to 1,000 (Mansur and Kaufman, 1962)
- 100 to 150 (Terzaghi and Peck, 1964)
- 90 to 120 (Cedergren, 1967)
- 1 to 42 (Lambe and Whitman, 1969)
- 40 to 120 (Holtz and Kovacs, 1981)
- 50 to 200 (Terzaghi et al., 1996)
- 100 to 150 (Das, 1997)
- 80 to 120 (Coduto, 1999).

The Hazen empirical coefficient values reported by Mansur and Kaufman (1962) were not explicitly stated, but were implicitly determined from Mansur and Kaufman's log-log plot of D_{10}^2 versus permeability. Their data suggest values of the Hazen empirical coefficient between 100 and 1000. When D_{10} values exceed approximately 0.04 cm, k is not proportional to D_{10}^2 (Carrier, 2003). Inconsistent permeability, particle diameter correlations and variable empirical coefficient values contribute to the inaccuracies of the Hazen equation.

To improve the accuracy of the Hazen equation, Hazen used an additional coefficient to adjust for temperature; Hazen's temperature coefficient is depicted in Equation 2.5:

$$C_T = (0.70 + 0.03T)\,, \tag{2.5}$$

where C_T represents the temperature coefficient and T represents the temperature in degrees Celsius. Hazen's empirical permeability correlation was developed for the design of sand filters at 10 degrees Celsius. Amer and Awad (1974) provided additional enhancements to the Hazen equation as depicted in Equation 2.6:

$$k = D_{60}^{0.6} D_{10}^{1.72} \left[\frac{e^3}{(1+e)}\right], \tag{2.6}$$

where e represents the void ratio, volume of void to volume of solid.

Despite the improvements made to Hazen's original equation; there are multiple limitations to Hazen's permeability correlation. The Hazen equation is not accurate for electrochemical reactions, flow velocity, particle shape, particle size distribution, and anisotropy. The Hazen equation assumes no electrochemical reactions between grain particles and water; as a result, the Hazen equation is inappropriate for soils with significant clay fractions. Analyzing the flow regime of Hazen's experiments, the Hazen equation assumes laminar flow; as a result, the kinetic energy term in the Bernoulli equation is negligible. The assumption of laminar flow applies to silts, sands, and gravelly sands; however, increasing pore sizes results in turbulent flow regimes and the inaccurate utilization of the Hazen equation. Hazen analyzed the effects of flow regime in his permeability research:

> "For gravels with effective sizes above 3 mm the friction varies in such a way as to make the application of a general formula very difficult. As the size increases beyond this point, [flow volume] with a given head does not increase as rapidly as the square of he effective size; and with coarse gravels the [flow volume] varies as the square root of the head instead of directly with the head as in sands. The

influence of temperature also becomes less marked with the coarse gravels." (Hazen 1892)

Apart from pore size restrictions, the Hazen equation is inappropriate for soils containing platy particles such as mica and clay. For highly irregular particle shapes, if the measured specific surface area is significantly greater than the calculated specific surface area, the calculated specific surface area should be used for permeability calculations (Carrier, 2003). The specific surface area is defined as the surface area of a particle divided by its mass; the calculated specific surface area is determined assuming a constant geometric shape for grain particles. Coupled with the limitation in particle shape, the Hazen equation assumes a relatively narrow grain size distribution.

2.2.1.2 Kozeny-Carman Equation

The semi-empirical Kozeny-Carman equation is used in multiple industries to determine fluid flow through porous media. The Kozeny equation relates permeability to porosity as depicted in Equation 2.7:

$$k = \frac{\Phi^3}{c(1-\Phi)^2 S^2}, \tag{2.7}$$

where Φ represents total porosity, c represents the Kozeny constant, and S represents the specific surface area based on the solid volume. To account for tortuous fluid flow paths, Carman modified the Kozeny equation as depicted in Equation 2.8:

$$k = \frac{\Phi^3}{k_0(1-\Phi)^2 S^2} = \frac{\Phi^3}{36k_0(1-\Phi)^2} d^2, \tag{2.8}$$

where d represents the mean diameter for theoretical spherical grains with equivalent specific surface areas. The constant k_0 is given by

$$k_0 = c\tau^2, \tag{2.9}$$

where k represents the Kozeny-Carman constant, c represents the shape factor, and τ represents tortuosity. Tortuosity is defined as the ratio of the actual flow path traveled, L_t, to the flow path traveled assuming a linear capillary tube, L; tortuosity is defined mathematically in Equation 2.10:

$$\tau = \frac{L_t}{L}. \tag{2.10}$$

Despite the acceptance of Equation 2.8, to enhance the accuracy of permeability estimates, multiple researchers have modified the Kozeny-Carman equation for different media:

- $k = \frac{d^2}{16c}\frac{\Phi^3}{(1-\Phi)^2}$ (McGregor, 1965)
- $k = C\Phi^n d^2$ (Bourbie et al., 1987)
- $k = \frac{\Phi^3 d^2}{72\tau^2(1-\Phi)^2}[\frac{(\gamma C_d^3 + 3C_d^2+1)^2}{(1+C_d^2)^2}]$ (Panda and Lake, 1994; Shih et al., 1998)
- $k = \frac{\Phi^{n+1}}{C(1-\Phi)^n}$ (Rodriguez et al., 2004)
- $k = \frac{\Phi_{eff}^3}{c\Gamma^2 S^2}$ (Koponen et al., 1997)
- $k = \frac{Cd^2(\Phi-\Phi_c)^3}{(1+\Phi_c-\Phi)^2}$ (Mavko and Nur, 1997)
- $k = C\frac{\Phi^{2+n}}{(1-\Phi)^2}$ (Bayles et al., 1989)

- $k = \frac{\Phi r^2}{8\Gamma^2}[\frac{2\Phi}{3\Gamma^2(1-\Phi)}]^{\frac{2}{D-1}}$ (Pape et al., 2000)
- $\sqrt{\frac{k}{\Phi}} = \Gamma(\frac{\Phi}{\alpha-\Phi})^n$ (Civan, 2001)
- $k = C\frac{\Phi^n}{1-\Phi}$ (Costa, 2006),

where C represents permeability factor, n represents an empirical exponent, γ represents the skewness of the probability size distribution, C_d represents the coefficient of variation of the particle size distribution, Φ_{eff} represents effective porosity, Φ_c represents percolation threshold, r represents grain radius, D represents fractal dimension, and Γ represents the interconnectivity parameter.

Despite the multiple manipulations of the Kozeny-Carman equation, theoretical models and experiments demonstrate that the Kozeny-Carman constant is variable and depends on porosity and pore microstructure (Kaviany, 1995; Happel, 1983). Carman determined the value of the Kozeny-Carman constant to be 4.8 ± 0.3 for uniform spheres (Carman, 1956). Mathavan and Viraraghavan (1992) determined the Kozeny-Carman constant to be 3.4 for peat beds (Mathavan and Viraraghavan, 1992). Kyan et al. (1970) determined the Kozeny-Carman constant was dependent on porosity; additionally, Kyan et al. determined that for porosity values exceeding 0.95, the Kozeny-Carman constant increased approximately exponentially (Kyan et al., 1970). Davies and Dollimore (1980) determined a relationship for the Kozeny-Carman constant for aggregate sedimentation depicted in Equation 2.11 (Davies and Dollimore, 1980):

$$k = \frac{1}{[2\Phi^{n-3}(1-\Phi)]}, \tag{2.11}$$

where n represents the Richardson-Zaki parameter. The Richardson-Zaki parameter is a function of Reynolds number and the ratio of particle diameter and column diameter; the

column diameter represents the diameter of the cylindrical column used to conduct particle sedimentation experiments.

Examining Equation 2.9, Wyllie and Gregory (1955) analyzed the effects of porosity and particle shape on the Kozeny-Carman constant for unconsolidated porous media. Wyllie and Gregory (1955) determined that the surface area parameter S depicted in Equation 2.9 is a function of sphere size when aggregates are represented as uniform spheres; however, the surface area of aggregates with plane sides is a function of aggregate size and porosity. Wyllie and Gregory (1955) analyzed cylinder, disks, cubes, prisms, and spheres for grain shapes; Wyllie and Gregory determined that the Kozeny-Carman constant is a function of porosity and aggregate shape in unconsolidated porous media.

The semi-empirical Kozeny-Carman equation is extensively used to analyze flow in porous media; however, the Kozeny-Carman equation has many limitations. Multiple variations of the Kozeny-Carman equation was used by different researchers to enhance the accuracy of the equation for different scenarios; the Kozeny-Carman constant increases the uncertainty of the Kozeny-Carman equation. Wyllie and Gregory determined the Kozeny-Carman constant is a variable dependent on particle shape and porosity. Furthermore, the Kozeny-Carman equation is subject to the limitations of the Hazen equation (Equation 2.3).

2.2.1.3 Fractal Models

Guarracino (2007) derived a relationship between the saturated hydraulic conductivity, K_s, and the van Genuchten shape parameter, α. The objective of Guarracino's (2007) research was to develop a simplified relationship to determine the saturated hydraulic conductivity utilizing the van Genuchten shape parameter in contrast to the use of the Burdine (1953) and Mualem (1976) models.

Guarracino's (2007) saturated hydraulic conductivity model used van Genuchten's (1980) models for water content as a function of pressure head and unsaturated hydraulic conductivity as a function of pressure head depicted in Equation 2.12 and Equation 2.13; the unsaturated hydraulic conductivity expression was determined utilizing the Burdine (1953) and Mualem (1976) predictive conductivity models:

$$\theta(h) = (\theta_s - \theta_r)[1 + (\alpha h)^n]^{-m} + \theta_r, \tag{2.12}$$

$$K(h) = K_s \frac{\{1 - (\alpha h)^{n-1}[1 + (\alpha h)^n]^{-m}\}^2}{[1 + (\alpha h)^n]^{\frac{m}{2}}}, \tag{2.13}$$

where $\theta(h)$ represents water content as a function of pressure head; θ_s represents saturated water content; θ_r represents residual water content; K_s represents saturated hydraulic conductivity; and α, n, and m represent empirical fitting parameters. Equation 2.14 depicts a relationship for m:

$$m = 1 - \frac{1}{n}. \tag{2.14}$$

To examine the soil matrix, Guarracino (2007) examined a representative volume element of length L and volume L^3. The derivation of the relationship between the saturated hydraulic conductivity and the van Genuchten shape parameter assumes the porosity of the soil matrix could be represented as an accumulation of parallel capillary tubes with variable pore radii; the minimum pore radius is defined as r_{min} and the maximum pore radius is defined as R. In addition, Guarracino (2007) assumes the adherence of the matrix's pore size distribution to fractal theory; as a result, the

maximum pore radius is assumed to be significantly greater than the minimum pore radius as depicted in Equation 2.15:

$$\int_{r_{min}}^{R} f(r)dr = 1 - \left(\frac{r_{min}}{R}\right)^{D} \approx 1, \tag{2.15}$$

where r represents the pore radius, r_{min} represents the minimum pore radius, R represents the maximum pore radius, and D represents the fractal dimension; the fractal dimension is constrained to a value exceeding 2 but below 3. Generally, the ratio $\frac{r_{min}}{R}$ is less than 0.01; as a result, fractal theory can be successfully applied to soil matrices (Katz and Thompson, 1985; Yu and Li, 2001). Utilizing the described assumptions, the Hagen-Poiseuille equation, and Darcy's law, Guarracino (2007) derived a quadratic relationship between saturated hydraulic conductivity and van Genuchten shape parameter depicted in Equation 2.16:

$$K_s = \frac{2-D}{4-D}\frac{\sigma^2 \cos^2(\beta)}{2\rho g \mu}\Phi\alpha^2, \tag{2.16}$$

where σ represents surface tension, β represents the contact angle between the water and solid matrix, ρ represents the water density, and g represents the acceleration due to gravity.

The use of Equation 2.16 to determine the saturated hydraulic conductivity requires knowledge of the contact angle between water and the solid matrix, porosity, fractal dimension, and Van Genuchten shape parameter values; Guarracino (2007) assumed a contact angle of 0 and used saturated water content to estimate porosity values. Guarracino (2007) used constant surface tension, contact angle, density, and viscosity values to determine van Genuchten shape parameter, saturated hydraulic conductivity, and saturated water content values for 12 soil textural classes.

Guarracino (2007) used regression analysis between estimated and experimentally determined saturated hydraulic conductivity values to approximate a constant fractal dimension value. Guarracino (2007) determined a fractal dimension value of approximately 1.996 from regression analysis; additionally, Guarracino used vales of 72.75 $\frac{dynes}{cm}$ for surface tension, 0.10 poise for the dynamic viscosity of water, 0.998 $\frac{g}{cm^3}$ for water density, and 980 $\frac{cm}{s^2}$ for the gravitational constant. Using constant values for multiple variables depicted in Equation 2.16, Guarracino (2007) obtained moderate agreement between predicted and observed values. Nonetheless, Guarracino (2007) assumed multiple constant values to obtain the agreement between the observed and predicted values. Practically, the values Guarracino (2007) assumed to be constant are dynamic; therefore the calculated saturated hydraulic conductivity values have variable amounts of uncertainty.

Because of the variability of the Kozeny-Carman constant, Xu and Yu (2008) derived an analytical expression for permeability utilizing fractal theory assuming a homogeneous porous medium with circular pores. Xu and Yu's (2008) derived permeability relationship removed the empirical constant used in the Kozeny-Carman equation; Equation 2.17 and Equation 2.18 depict the relationship derived by Xu and Yu:

$$k = C_f\left(\frac{\Phi}{1-\Phi}\right)^{\frac{(1+D_T)}{2}}\lambda_{max}^2, \tag{2.17}$$

$$C_f = \frac{(\pi D_f)^{\frac{(1-D_T)}{2}}[4(2-D_f)]^{\frac{(1+D_T)}{2}}}{128(3+D_T-D_f)}, \tag{2.18}$$

where D_f represents the pore area fractal dimension, D_T represents the tortuosity fractal dimension, and λ_{max} represents the maximum pore diameter. Equations 2.19 through Equation 2.22 define fractal dimension parameters and variables used to define fractal parameters:

$$D_f = d_E - \frac{\ln \Phi}{\ln \frac{\lambda_{min}}{\lambda_{max}}}, \quad (2.19)$$

$$D_T = 1 + \frac{\ln \bar{\tau}}{\ln \frac{L_0}{\bar{\lambda}}}, \quad (2.20)$$

$$\bar{\lambda} = \frac{D_f \lambda_{min}}{D_f - 1}, \quad (2.21)$$

$$\bar{\tau} = \frac{1}{2}\left[1 + \frac{1}{2}\sqrt{1-\Phi} + \sqrt{1-\Phi}\,\frac{\sqrt{\left(\frac{1}{\sqrt{1-\Phi}}-1\right)^2 + \frac{1}{4}}}{1-\sqrt{1-\Phi}}\right], \quad (2.22)$$

where D_f represents the pore area fractal dimension, d_E represents a dimensional constant equal to 2 or 3 in two or three dimensions respectively, Φ represents total porosity, λ_{min} represents the minimum pore diameter, λ_{max} represents the maximum pore diameter, D_T represents the tortuosity fractal dimension, τ represents the average tortuosity, $\bar{\lambda}$ represents the average pore diameter, and L_0 represents the flow path traveled assuming a linear capillary tube. Analyzing Equations 2.19 and 2.20, the pore area fractal dimension increases with increased porosity values; however, the tortuosity fractal dimension decreases with increased porosity values.

Xu and Yu's (2008) fractal permeability model was compared to experimental results for mono- and bidisperse porous media. Comparing the fractal permeability model and the Kozeny-Carman equation, the fractal permeability model achieved improved agreement with experimental results. Despite improved results when compared against the Kozeny-Carman equation, the fractal permeability was derived assuming a homogeneous porous medium and circular pore space geometries; the assumptions used by Xu and Yu (2008) do not reflect naturally occurring porous media.

2.2.1.4 Mercury Injection

Katz and Thompson (1986) proved the validity of utilizing mercury injection to characterize the pore space controlling electrical conductivity and absolute permeability. Katz and Thompson developed a novel approach to determine absolute permeability depicted in Equation 2.23:

$$k = cl_c^2 \frac{\sigma}{\sigma_0}, \tag{2.23}$$

where c represents a constant approximately equal to 0.0044, l_c represents a characteristic length, σ represents rock conductivity, and σ_0 represents the conductivity of brine. The characteristic length is determined experimentally from the threshold pressure in a mercury injection procedure; the threshold pressure defines when displacing mercury initially develops a connected path spanning the porous medium (Katz and Thompson 1986). The significance of Katz and Thompson's (1986) permeability model depicted in Equation 2.23 was the reduction of variable empirical constants used to define permeability.

To develop Equation 2.24, Katz and Thompson (1986) used the percolation arguments of Ambegaokar et al. (1971). The percolation arguments developed by Ambegaokar et al. (1971) were applied to electron transport in amorphous semiconductors; the percolation arguments are typically applicable to systems characterized with broad conductance distributions with limited conductances. Madden (1976) and Seeburger and Nur (1984) determined that the pore space of reservoir rocks could be characterized as a random, broad distribution of pore sizes (Madden, 1976; Seeburger and Nur, 1984). The implication of Madden (1979) and Seeburger and Nur's (1984) research is that transport properties of porous media should be examined as a broad distribution of local conductances. Ambegaokar et al. (1971) determined that transport in random systems with broad conductance distributions is controlled by

conductances with magnitudes exceeding a characteristic value; the characteristic values is defined as the required conductance such that the set of conductances forms an infinitely connected conduit (Ambegaokar et al., 1971; Katz and Thompson, 1987). Examining the porous medium as a broad conductance distribution, the analysis of transport properties simplifies to the analysis of the percolation threshold.

Katz and Thompson (1987) used the success of Equation 2.23 to determine a relationship for the conductivity formation factor utilizing mercury injection experiments; the relationship determined is depicted in Equation 2.24:

$$\frac{\sigma}{\sigma_0} = \frac{l^e_{max}}{l_c} \Phi S(l^e_{max}), \tag{2.24}$$

where l^e_{max} represents the characteristic width required for electrical conductance, l_c represents a characteristic length, and $S(l^e_{max})$ represents the fractional volume of connected pore space associated with pore widths equal to and exceeding the minimum pore width required for electrical conductance. The variables l_c, l^e_{max}, and $S(l^e_{max})$ are determined from mercury injection experiments.

Despite the agreement between measured and calculated conductivity formation factor and permeability values, Equation 2.23 and Equation 2.24 contain uncertainty. Mercury injection experiments have 15 percent uncertainty in determining the characteristic length of the porous medium. Mercury injection experiments seek the path of least resistance; as a result, Katz and Thompson (1987) measured permeability parallel to the bedding of the porous media (Katz and Thompson, 1987). Nonetheless, porous media anisotropies can alter the preferential conduit of the mercury injection resulting in an inappropriate comparison between calculated and experimentally determined conductivity formation factor and permeability values.

2.2.1.5 Core Calibration

Nasta et al. (2013) determined a relationship for soils between hydraulic conductivity utilizing Brooks-Corey's water retention functions and an empirical tortuosity constant that was determined from calibration with core analysis. To derive the hydraulic conductivity relationship, Nasta et al. (2013) used parametric relations developed by Brooks and Corey depicted in Equation 2.25 and Equation 2.26; additionally, Nasta et al. (2013) assumed the porous medium was constructed of capillary tubes with variable radii within a probability distribution function, a completely saturated porous medium, and a residual water saturation equal to 0.

$$\theta(h) = (\theta_s - \theta_r)(\frac{h_b}{h})^{\lambda} + \theta_r \text{ for } h < h_b, \tag{2.25}$$

$$\theta(h) = \theta_s \text{ for } h_b \leq h \leq 0, \tag{2.26}$$

where θ represents the soil water content, θ_s represents the saturated water content, θ_r represents the residual water content, h_b represents the bubbling matric head of the Brooks-Corey (1964) water retention functions, and λ represents the pore size distribution index of the Brooks-Corey water retention functions. Utilizing the Brooks-Corey (1964) water retention functions and Darcy's Law, Nasta et al. (2013) derived Equation 2.27 for hydraulic conductivity:

$$K_s = 9.579\ x\ 10^5 \tau \frac{\lambda}{\lambda+2} \frac{\theta_s}{h_b^2} \tag{2.27}.$$

Additional assumptions used to derive Equation 2.28 are a water temperature of 20° C, water density of 0.998 $\frac{g}{cm^3}$, dynamic water viscosity of 0.0102 $\frac{g}{cm}$, and a gravitational constant of 980.66 $\frac{cm}{s^2}$.

Nasta et al. (2013) compared calculated values utilizing Equation 2.27 to models developed by Mishra and Parker (1990) and Guarracino (2007). Nasta et al. (2013) exhibited moderate correlation between experimentally determined and calculated hydraulic conductivity values. Equation 2.27 utilizes multiple assumptions that are not applicable to naturally occurring porous media; as a result, the hydraulic conductivity relationship contains variable uncertainty.

2.2.1.6 Statistical Modeling

Sprunt, et al. (1993) used 1.5 inch diameter deepwater, Plio-Pleistocene sand core samples to determine multiple absolute permeability relationships; permeability measurements were measured at confining pressures of 400 and 2850 psi. The samples used to conduct the permeability measurements were described as slight laminations, approximately homogeneous, or variable laminations, the core sample exhibited one or multiple laminations with thickness exceeding 5 millimeters (Sprunt et al., 1993). Sprunt et al. (1993) used 61 samples to conduct their analysis: 29 samples were classified as slight laminations and 32 samples were classified as variable laminations. Examining the means of slightly laminated samples, the average of the means exhibit characteristics of a very fine-grained sand; the grain classification of the sample set ranges from medium grained silt to fine grained sand (Sprunt et al., 1993). The variable lamination samples were separated into two categories: coarse and finer. The variable, coarse lamination samples typically exhibited finer grain sizes compared to slight lamination samples. The mean of the variable, coarse sample set exhibited a grain size classification of coarse-grained silt; however, the means of individual samples varied from medium grained silt to very fine-grained sand. The mean of the variable, finer sample set exhibited a grain size classification of medium-grained silt; however, the means of individual samples varied from medium grained to coarse-grained silt (Sprunt et al., 1993). To validate the

experimental design and assumptions, Sprunt et al. (1993) analyzed multiple permeability relationships: porosity, mean grain size, and standard deviation.

To validate the inadequateness of porosity, permeability models used to predict permeability, Sprunt et al. (1993) analyzed the relationship for slightly laminated samples. Analyzing the porosity, permeability relationship, the regression analysis resembles a cloud of points in comparison to a linear trend; their analysis validated the need for permeability models with enhanced accuracy.

The results of the porosity-permeability regression model prompted Sprunt et al. (1993) to continue their regression analysis comparing grain size-permeability relationships and grain size standard deviation-permeability relationships. Categorically, slightly laminated samples exhibited strong permeability correlations with grain size and grain size standard deviation; therefore, one concludes the plausibility of constructing empirical permeability relationships using mean grain size, median grain size, mode grain size, or grain size standard deviation. The variable lamination samples were separated into two categories: coarse and finer. The coarsely laminated samples exhibited good permeability correlations with grain size; however, the slightly laminated samples exhibited a stronger permeability-grain size correlation. More finely laminated samples did not display a strong correlation between permeability and grain size.

Sprunt et al.'s (1993) research of permeability correlations was a significant contribution, but their research was restricted in scope. The standard deviation of the samples analyzed in their research had a maximum breadth of approximately 90 microns from the mean grain size; the depth of investigation analyzed is exceptionally constrained and does not adequately represent the broad grain size standard deviation that is experienced in petroleum systems. To extend this research, narrow and broad standard deviations will be analyzed from representative Pacific Ocean core to obtain an enhanced understanding of the relationship between permeability and grain size standard deviation.

2.2.1.7 Pore Network Models

The microstructure of porous media and the physical characteristics of the matrix and pore space fluids determine macroscopic properties of the media: permeability, formation factor, relative permeability and capillary pressure. In principle, one should be able to determine macroscopic properties by averaging equations defining pore scale physical processes. The objective of pore network models is the prediction of macroscopic transport properties from the associated microscopic properties. The premise of pore network models is a representation of the void space of a porous medium as a network of interconnected pores. Large pores, pore bodies, are connected through a series of small pores, pore throats (Øren et al., 1998). Pore network models can be used to describe and interpret experimental results for single and multiphase flows: "the effects of wettability in two- and three- phase flow, multiphase flow in fractures, mass transfer, and the influence of flow rate on residual oil saturation" (Blunt, 2001). Accurate representation of the pore space allows for the estimation of macroscopic transport properties.

The permeability of pore network models are estimated by implementing a constant pressure gradient across the pore network; conjugate gradient methods are used to relax the pore network and determine pore body pressures (Øren et al., 1998). The pressure distribution of the pore network model is used to calculate flow throughout the pore network model; mass conservation is implemented at individual pore bodies. The total flow rate of the network model is used with Darcy's Law to determine the permeability of the pore network.

2.2.2 Processed Based Models

2.2.2.1 Finney Pack

Bryant and Blunt (1992) used packed monosized spheres to represent a simplistic porous medium of an unconsolidated, well-sorted sandstone medium. This simple porous

medium was constructed utilizing the Finney (1968) pack; they used the Finney pack to determine relative permeability as a function of porosity for monosized spherical grains (Bryant and Blunt 1992). The Finney (1968) pack is defined as a dense random packing of monosized spheres consisting of 8,000 ball bearings. Finney (1968) constructed a monosized spatially random sphere pack utilizing 17,000 precision ball bearings; Finney measured the coordinates of approximately 8,000 ball bearings located in the center of the sphere pack to determine the spatial position in the sphere pack (Finney, 1968). The spatial positions of the 8,000 ball bearings allowed for Bryant and Blunt (1992) to numerically reconstruct a precise replica of the Finney (1968) pack without error. To determine the relative permeability of the sphere pack as a function of porosity, additional complexities needed to be added to the numerical model constructed by Bryant and Blunt (1992); additionally complexities were required to diverge porosity values within the numerical model.

To add additional complexity to the sandstone model, Bryant and Blunt (1992) allowed the spheres to swell while maintaining constant positions of the sphere centers. Bryant and Blunt (1992) assumed that swelling of the spheres allowed for the approximation of the quartz cementation process. Research has proven that quartz cementation is a prominent influence of absolute porosity and permeability reduction in well-sorted, quartz-rich sandstones buried deeper than three kilometers; as a result, Bryant and Blunt's (1992) approximation was accurate (Bjorlykke, 1993). The quartz cementation process coats the spherical grains with additional material, fusing together sandstone grains and resulting in a lower absolute porosity of the porous medium Additional porous medium complexity simulated in the numerical model was compaction. Bryant and Blunt (1992) simulated compaction in the porous medium by modifying the spatial dimensions of the sphere centers along the vertical axis; the distances between sphere centers along the vertical axis were reduced to simulate compaction in the sandstone model.

To analyze the numerical model to calculate absolute and relative permeability values, Bryant and Blunt (1992) invoked the use of the Delaunay construction of the Voronoi tessellation. The Delaunay tessellation divides the porous medium into a series of tetrahedrons; the vertices of the tetrahedrons are the centers of the ball bearings. The Delaunay tessellation created a network model used to describe the porous medium; the network model was composed of pores (void spaces) and the connection pore throats (narrow constrictions). Bryant and Blunt (1992) defined pores as the interior of the Delaunay tetrahedrons and defined pore throats and the faces of the tetrahedrons. They only performed the Delaunay tessellation on the central 3367 spheres of the sphere pack; the simplification of the porous medium resulted in approximately 15,000 pores and 30,000 pore throats. The simplified porous medium was used to determine permeability and porosity values.

The pore volume of the network model constructed by Bryant and Blunt (1992) is the volume of the Delaunay tetrahedrons minus the volume of the sphere volumes contained within the Delaunay tetrahedron. The amalgamation of pore volumes within the network model is used to calculate the porosity of the porous medium. However, to calculate the absolute and relative permeability of the porous medium, Bryant and Blunt (1992), assigned equivalent radii and hydraulic conductivities to pore throats and pore volumes. They modeled the pore connectivity as cylinders whose length and radii are hydrodynamically equivalent to the pore volume represented by the network model. As a result, the absolute permeability of network model defined by the Delaunay tessellation is the fluid conductivity of the cylinder network. Bryant and Blunt (1992) reported that their model was in excellent agreement with experimental measurements of Fontainebleau sandstones, bead packs, and sand packs for absolute permeability as a function of absolute porosity.

Bryant and Blunt's (1992) research of relative permeability in simple porous media was a significant contribution to the petroleum industry; however, multiple

technological advances have been made since their original experimental design. In addition to technological advances, there are multiple assumptions within the Bryant and Blunt (1992) model that can be improved upon: monosized spheres, unconsolidated spheres, quartz cementation approximation, compaction approximation, and cylindrical pore throats. Heterogeneous porous media customarily exhibit a lognormal permeability distribution (Collins and Jordan, 1961). Because permeability is a secondary porous medium characteristic defined by primary characteristics of the porous medium, it is inferred that the texture of porous media typically exhibit a lognormal grain size distribution with overlapping grains in contrast to the uniform grain size distribution with spherical grains in point contact exhibited by Bryant and Blunt's (1992) numerical model.

Øren and Bakke (2002) developed a process based model to reconstruct three-dimensional sandstones utilizing two-dimensional thin section images to stochastically model the results of sandstone construction processes: sedimentation, compaction, and diagenesis. Using stochastic methods to model different sandstone processes, sedimentation, compaction, and diagenesis, variable unconsolidated and consolidated sandstones can be constructed. Øren and Bakke (2002) used Fontainebleau sandstone samples to verify their process based pore network model.

Quantitatively comparing the experimental microstructure of the Fontainebleau sandstone sample to the process based reconstruction, intrinsic properties, specific internal surface and connectivity, were adequately replicated in the process based reconstruction model. Øren and Bakke (2002) calculated permeability utilizing the Navier-Stokes equations coupled with Darcy's Law; calculated permeability values for the process based reconstruction model achieved good agreement with experimental results. The Fontainebleau sandstone samples exhibited narrow grain size distributions; as a result, the ability of the process based reconstruction model's ability to reconstruct complex porous media is uncertain.

Mehmani et al. (2014) used an iterative process based model to reconstruct the Wilcox's cementation and dissolution processes and estimate drainage capillary pressure, wetting phase saturation curves. Mehmani et al. (2014) hypothesized the accurate estimation of transport properties during depositional stages with knowledge of the formation's chemical and mechanical history (Mehmani et al., 2014). Deterministic methods were used to construct the network model; as a result, diagenetic processes were implemented sequentially: deposition, cementation, and dissolution.

Mehmani et al. (2014) modeled diagenetic processes in four distinct stages: initial deposition of rock grains, shale clasts, quartz, and non-dissolved feldspars; uniform distribution of chlorite cement; quartz overgrowth, and feldspar dissolution (Mehmani et al., 2014). The network model used a monodisperse grain pack exhibiting a grain radius of 272 micrometers; drainage capillary pressures were estimated using an invasion percolation algorithm (Mehmani et al., 2014). The porosity and permeability estimates determined from the network model correlated with geologic processes; the network model porosity estimate exhibited excellent agreement with the Wilcox tight gas sandstone core.

Bosl et al. (1998) determined absolute permeability of modified porous media utilizing variable diagenetic process and methods. The porous media models consist of a dense uniform sphere distribution with diagenetic cement deposited in the pore space; the spatial location of the spherical grains is determined from Finney's (1968) experimental measurements. Bosl et al. (1998) simulated diagenesis for the porous media models utilizing variable methods: uniform cement deposition on the grain surface, cement deposition on grain contacts, cement deposition excluding grain contacts, variable pore space cement deposition, and combinations of the described methods (Bosl et al., 1998). To estimate permeability for the porous media models, Bosl et al. (1998) used Ladd's (1994) Lattice Boltzmann algorithm to analyze permeability, porosity relationships for the diagenesis methods.

Comparing numerically constructed models to experimental results, Bosl et al. (1998) achieved good agreement with the experimental Finney pack model. The uniform cement deposition diagenetic model provides good agreement with cemented, sintered glass bead experimental results; however, the model overestimated the permeability of North Sea sandstones (Bosl et al., 1998). Bosl et al. (1998) concluded the overestimated permeability values for the North Sea sandstones is due to the North Sea sandstones' diagenetic process; Bosl et al. suggested the North Sea sandstones experienced a diagenetic process different from the assumed uniform cement deposition on the grain surface. Nonetheless, the Lattice Boltzmann algorithm used provided valid results for permeability estimates.

2.2.2.2 Tomography Imaging

To understand the effects of geologic processes on porous media, the pore scale properties of porous media have to be investigated and accurately defined. Imaging techniques are tools used to characterize the microstructure of porous media; additionally, imaging techniques are coupled with numerical models to determine transport properties of porous media. Enhanced image models enable the estimation of enhanced transport properties.

Imagining techniques used to determine pore scale properties initiated with two-dimensional imaging techniques such as petrographic microscopy, fluorescence light microscopy, and scanning electron microscopy. The two-dimensional imaging techniques evolved to three-dimensional tomography imaging techniques used to presently characterize porous media. Tomography imaging techniques are superior to microscopy imaging techniques because of the quantitative information derived from three-dimensional imaging (Wildenschild and Sheppard, 2013). Present three-dimensional imaging tomography techniques used to characterize the pore scale of porous media include focused ion beam nanotomography, X-ray microcomputed tomography, phase

contrast microtomography, ptychographic tomography, transmission X-ray microtomography, and X-ray fluorescence microtomography (Wildenschild and Sheppard, 2013; Bultreys et al., 2016). Tomography imaging techniques have been essential to the advancement of pore scale modeling.

Alyafei et al. (2015) analyzed the effects of image resolution on pore network models utilizing computed microtomography; computed microtomography is a nondestructive imaging technique used to provide three-dimensional images of the microstructure of porous media. The objective of the study was to determine the optimal image resolution required to accurately represent the porous medium. Enhanced image resolution provides additional detail regarding the microstructure of the porous medium; as a result, the accuracy of calculated transport properties are increased. However, enhanced image resolution results in increased model size; consequently, additional computational time is required.

To analyze the effects of image resolution, Alyafei et al. (2015) used two methods to determine flow and transport properties of the porous medium. There are two approaches to determine flow and transport properties utilizing three-dimensional pore space representation: computing the flow field utilizing finite difference or particle-based methods, direct simulation, and utilizing quasi-static pore network models (Alyafei et al., 2015). The pore network model was constructed utilizing a maximal ball algorithm to extract the pore network from the computed microtomography images; the maximal ball algorithm defines the largest spheres contained in the pore space as pores and the series of smaller spheres connecting the larger spheres as pore throats (Dong and Blunt, 2009). Alyafei et al. (2015) utilize multiple pore network models to determine the effects of image resolution on transport properties: pore space and permeability.

Alyafei et al. (2015) analyzed the effect of estimated petrophysical properties examining computed microtomography images of multiple resolutions, 2.7 micrometer to 22 micrometer, utilizing 2 sandstone and 2 limestone rock samples. The image

resolutions effectively captured the pore space of the sandstone samples providing representative porosity values. The image resolutions were unable to accurately represent the pore space of the limestone samples. The microporosity exhibited within the limestone samples required image resolutions exceeding the limitations of the computed microtomography apparatus; as a result, porosity values were underestimated for the limestone samples. Because of computed microtomography limitations, Alyafei et al. (2015) reported poor correspondence between experimentally determined throat size distributions and throat size distributions determined from the maximal ball algorithm.

Alyafei et al. (2015) estimated permeability values utilizing the Navier-Stokes equations for direct simulation (finite difference method) and pore network constructed models. The direct simulation and the pore network methods gave comparable permeability results; as a result, one could conclude that the maximal ball algorithm pore network accurately identified the main flow paths (Alyafei et al., 2015). The image resolutions of the computed microtomography images were able to reproduce similar values between direct simulation and pore network constructed models; however, the constructed models were not comparable to experimental results.

The direct simulation and maximal ball algorithm methods were able to successfully represent porosity values for the sandstone samples; however, methods were unsuccessful at replicating porosity values for the limestone samples. Permeability values for the direct simulation and maximal ball algorithm methods were comparable, yet the methods were not comparable to experimentally determine permeability results. Decreased image resolution affects the permeability calculated for the direct simulation and maximal ball algorithm methods resulting in under or over predicted permeability estimates.

Caubit et al. (2009) used blind tests to estimate petrophysical parameters using pore networks models and imaging techniques; blind tests were performed by The Australian National University and Numerical Rocks research groups. Multiple samples

(six artificial and outcrop, and six unconsolidated and consolidated reservoir rocks) were used to determine the accuracy of pore network models constructed by The Australian National University and Numerical Rocks research groups. Numerical Rocks constructed pore network models using geologic processes and two-dimensional scanning electron microscopy images; however, The Australian National University constructed pore network models using three-dimensional microtomographic images.

The blind tests determined the effect of the pore network model construction methodology and imaging techniques on estimated petrophysical parameters; pore network model estimated petrophysical parameters were compared to laboratory measurements. Porosity estimates exhibiting minimal micro-porosity and clay content were reliable irrespective of pore network models and imaging techniques; however, The Australian National University permeability estimates exhibited uncertainty because of the three-dimensional imaging technique's ability to define microscopic heterogeneity within the rock volume (Caubit et al., 2013). Because of present permeability and porosity estimates, pore network models coupled with imaging techniques are not effective for estimating petrophysical parameters exhibiting variable pore structure.

Beckingham et al. (2013) used pore network models to determine the effect of two-dimensional and three-dimensional imaging techniques on permeability estimates. Two-dimensional imaging analysis was performed using scanning electron microscopy; however, three-dimensional imaging analysis was performed using X-ray computed microtomography. To determine the effect of imaging techniques, Beckingham et al. (2013) analyzed two samples to construct pore network models; sample one and sample 2 was a Viking sandstone sample from the Alberta sedimentary basin, and an experimental column of reacted Hanford sediments respectively. Beckingham et al. (2013) analyzed maximum and minimum image resolutions of 0.4 and 20 μm respectively.

Pore network model permeability estimates were compared to permeability estimates determined from experimental measurements. The analysis determined that the

permeability estimated from pore network models were impacted by the resolution of the two-dimensional or three-dimensional image used. Permeability estimates determined using high resolution imaging techniques were underestimated; however, permeability estimates determined using low resolution imaging techniques were slightly overestimated. High resolution imaging techniques results in the misinterpretation of porosity features as permeability-controlling features; however, low resolution imaging techniques excludes permeability-controlling features (Beckingham et al., 2013). To accurately determine pore network model permeability estimates, Beckingham et al. (2013) defined threshold image resolutions between 3 and 15 μm. Using equivalent image resolutions, two-dimensional and three-dimensional imaging techniques resulted in comparable permeability estimates.

Shah et al. (2016) analyzed the effect of image resolution on petrophysical properties using three-dimensional microcomputed tomography images and pore network or Lattice Boltzmann modeling. Three-dimensional pore scale reconstruction was used to estimate multiple petrophysical parameters, porosity, single-phase permeability, and multiphase relative permeability. High resolution microcomputed tomography imaging techniques were used to construct three-dimensional images pore scale images of the core samples; Shan et al. (2016) analyzed ten core samples: five sandstone samples (Bentheimer, Berea, Clashach, Doddington, and Stainton) and five complex carbonates (Ketton, Estaillades, Middle Eastern sample 1, Middle Eastern sample 5, and Indiana Limestone 1). Pore network and Lattice Boltzmann models were constructed using four different microcomputed tomography image resolutions: 4.4, 6.2, 8.3, and 10.2 μm.

Microcomputed tomography image resolution affected estimated macro-porosity and single-phase permeability for constructed pore network and Lattice Boltzmann models; however, image resolution effects were restricted to specific sandstone and carbonate samples. Resolution complications resulted in partial volume effects; partial volume effects are defined as image distortion of pore bodies and pore throats due to

representative volume element (Shan et al., 2016). Representative volume elements impacted the estimation of petrophyscial parameters using pore network and Lattice Boltzmann models.

2.2.3 Direct Simulation

Laboratory permeability measurements are resource-expensive; as a result, empirical relationships are often used. There are multiple empirical permeability relationships derived by different authors. Common empirical permeability relationships were derived assuming cylindrical pore geometries; however, common empirical permeability relationships provide minimal information regarding the correlation between pore geometry and permeability despite additional measurements required: specific surface area, formation factor, and calibrated curve fitting parameters (Walsh and Brace, 1984; Dullien, 1992). Despite the limitations of empirical permeability models, many researchers have used the models because of their simplicity (Dullien, 1992; Mavko and Nur, 1997). Numerical methods incorporate the correlation between pore geometry and transport properties such as permeability.

Multiple numerical models have been used to simulate fluid flow profiles in porous media; examples of models used by present and past researchers include pore network models; Lattice Boltzmann methods; Monte Carlo methods; particle methods, molecular dynamics and dissipative particle dynamics; and grid-based computational fluid dynamics, finite volume, finite difference, and finite element. Pore network models replicate the pore space of porous media as a network of pore volumes connected through multiple channels, pore volumes and pore channels exhibit simplified geometries. Lattice Boltzmann models simulate fluid flows through the use of Boolean variables and solution of the Lattice Boltzmann equation. Monte Carlo models replicate fluid flows through particles undergoing streaming and collision; particles exhibit constant velocities during simulation streaming. Molecular dynamics and dissipative particle dynamics particle

models simulate fluid flow dynamics using a collection of particles and Newton's second law of motion. Grid-based computational fluid dynamics, finite difference, finite volume, and finite element, simulate fluid flows through the solution of the Navier-Stokes equation. Despite the magnitude of numerical methods for fluid flow simulations, the Lattice Boltzmann method was used to perform numerical simulations of transport properties because of the method mitigated issues associated with referenced numerical models: inability to effectively simulate multiphase flows; confined systems, fractured porous media and porous media with small characteristic lengths; numerical convergence with complex geometries; divergence between macroscopic and microscopic molecular dynamics; and simplistic pore geometries.

2.2.4 Stochastic Model

Keehm et al. (2004) obtained thin section images of sandstones samples and reconstructed the thin section images to form a three-dimensional porous media utilizing the sequential indicator simulation method. The sequential indicator simulation is a geostatistical approach to reconstruct three-dimensional porous media from two-dimensional thin sections; the sequential indicator simulation requires nodes of the three-dimensional reconstruction to be visited along an arbitrary direction. The sequential indicator simulation algorithm estimates local conditional cumulative distribution functions for spatial locations within two-dimensional thin section images at the nodes. The cumulative distribution function is correlated to the two-dimensional image and previously stimulated nodes along the arbitrary direction; kriging is used to estimate the cumulative distribution function. Values for the spatial locations within two-dimensional thin section images are determined from local cumulative distribution functions; the values are retained as conditioning data as the algorithm progresses along the arbitrary direction (Keehm et al., 2004). The progression of the sequential indicator simulation algorithm along the nodes constructs a three-dimensional porous media.

To analyze the statistical variability of the constructed three-dimensional porous media, multiple stochastic models were constructed utilizing the two-dimensional thin section images. The Lattice Boltzmann method was used to estimate the permeability of the stochastic three-dimensional models; the absolute permeability estimate for the two-dimensional thin section images was determined by averaging the permeability estimate from the different stochastic models. Keehm et al. (2004) achieved good agreement between estimated and laboratory measured permeabilities for the two-dimensional thin section images analyzed.

Okabe and Blunt (2005) used multiple-point statistics to construct three-dimensional porous media. Multiple-point statistics is a geostatistical technique that uses pixel representations to replicate macroscopic pore space (Okabe and Blunt, 2005). Okabe and Blunt (2005) used two-dimensional thin-section images of Fontainebleau and Berea sandstones to define the statistical relationship between multiple geospatial locations. Inferring isotropic transport properties, two-dimensional images can be used to construct three-dimensional porous media; as a result, Fontainebleau and Berea sandstone cores were used. Fontainebleau and Berea sandstone cores were used because of the porous medias' isotropic properties and the ability of microtomography to effectively define the pore space of the porous media.

The three-dimensional reconstructed Fontainebleau and Berea sandstone porous media are compared to microtomography images of the Fontainebleau and Berea sandstone cores. The multiple-point statistic reconstructed Fontainebleau sandstone depicted poor agreement with the three-dimensional Fontainebleau sandstone constructed using two-dimensional microtomography images; however, the multiple-point statistic reconstructed Berea sandstone depicted good agreement with the three-dimensional Berea sandstone constructed using two-dimensional microtomography images. Okabe and Blunt (2005) proved the viability of multiple-point statistics to replicate microscopic pore space and connectivity in porous media.

Tahmasebi and Sahimi (2013) developed a new porous media reconstruction algorithm using cross-correlation functions and one-dimensional raster paths. An infinite set of n-point correlation functions are required to obtain a defined statistical characterization of heterogeneous porous media; however, the measurement of n-point correlation functions exceed five is impractical. Because of the difficulties associated with higher quantities of n-point correlation functions, Tahmasebi and Sahimi (2013) developed cross-correlation functions. The reconstruction algorithm uses a single two-dimensional image slice from a specified porous medium to replicate the three-dimensional porous medium irrespective of pore space geometries.

Multiple samples were used to analyze the capabilities of the numerical algorithm; the accuracy of the numerical models was determined from computed connectivity functions. The numerical models were able to accurately replicate three-dimensional porous media using two-dimensional image slices. Tahmasebi and Sahimi (2013) presented results for a Berea sandstone reconstruction exhibiting image resolution of 200 x 200 pixels and an open-cell copper foam reconstruction exhibiting image resolution of 128 x 128 pixels; the numerically reconstructed models depicted excellent agreement with physical models.

3. Methodology

I used the Lattice Boltzmann method to estimate the permeability of numerically constructed porous media. The Lattice Boltzmann method uses computational fluid dynamics to solve the Boltzmann equation. It was created to address the limitations of the Lattice Gas method: statistical noise, velocity dependent pressure, low and flow velocity restrictions. Both the Lattice Gas and Lattice Boltzmann models require multiple conditions to accurately represent fluid flow phenomena: adequate symmetry of the constructed lattice; conservation of mass, momentum, and energy; and the existence of local equilibrium restricted to mass, momentum, and energy (Sahimi, 2011). The advantage of the Lattice Gas and the Lattice Boltzmann methods are the models' ability to model fluid flow through a wide variety of pore geometry configurations.

3.1 Lattice Boltzmann Method

The Lattice Boltzmann method is an evolution of the Lattice Gas method constructed to mitigate the complications associated with the Lattice Gas method. These complications include statistical noise, velocity dependent pressure, and the requirement for laminar flow. Lattice Boltzmann models mitigate complications associated with Lattice Gas models through the Lattice Boltzmann method's lattice point definitions. Lattice points are defined as a collection of particles; particle behaviors are described through a collection of particle distribution functions (Gabbana, 2015). Particle distribution functions provide the Lattice Boltzmann method with enhanced accuracy in comparison to the Lattice Gas method.

Multiple researchers have used the Lattice Boltzmann method to simulate single phase and multiphase fluids in one-dimensional, two-dimensional, and three-dimensional fluid models. The applications studied include steady state fluid flows, unsteady state fluid flows, phase separation, evaporation, condensation, cavitation, solute transport, heat transport, buoyancy, and fluid-surface interactions. The capability of the Lattice

Boltzmann method to replicate multiple fluid flow problems has resulted in researchers creating multiple different Lattice Boltzmann algorithms. The Shan and Chen (1993) Lattice Boltzmann algorithm combined with the Bhatnagar, Gross, and Krook (BGK) collision operator (Bhatnagar et al., 1954) were used to analyze porous media models; the collision operator governs particle collisions between fluid particles.

Bounce-back boundary conditions are conveniently implemented within Lattice Boltzmann simulations. Bounce-back boundary conditions categorize lattice nodes variously as boundary solids, solids along the solid-fluid interface; isolated solids, solids excluded from fluid contact; and fluid particles. Figure 3.1 depicts an image of node classifications implemented through bounce-back boundary conditions; to define the nodes depicted in Figure 3.1, black nodes represent boundary solids, checkered nodes represent isolated solids, and white nodes represent fluid particles.

Bounce-back boundary conditions use collision rules to define the interface between fluid and solid particles; collision rules used to define bounce-back boundary conditions reflect fluid particles contacting solid particles during collision events. This allows accurate fluid dynamics simulations in media exhibiting complex geometries, such as natural porous media.

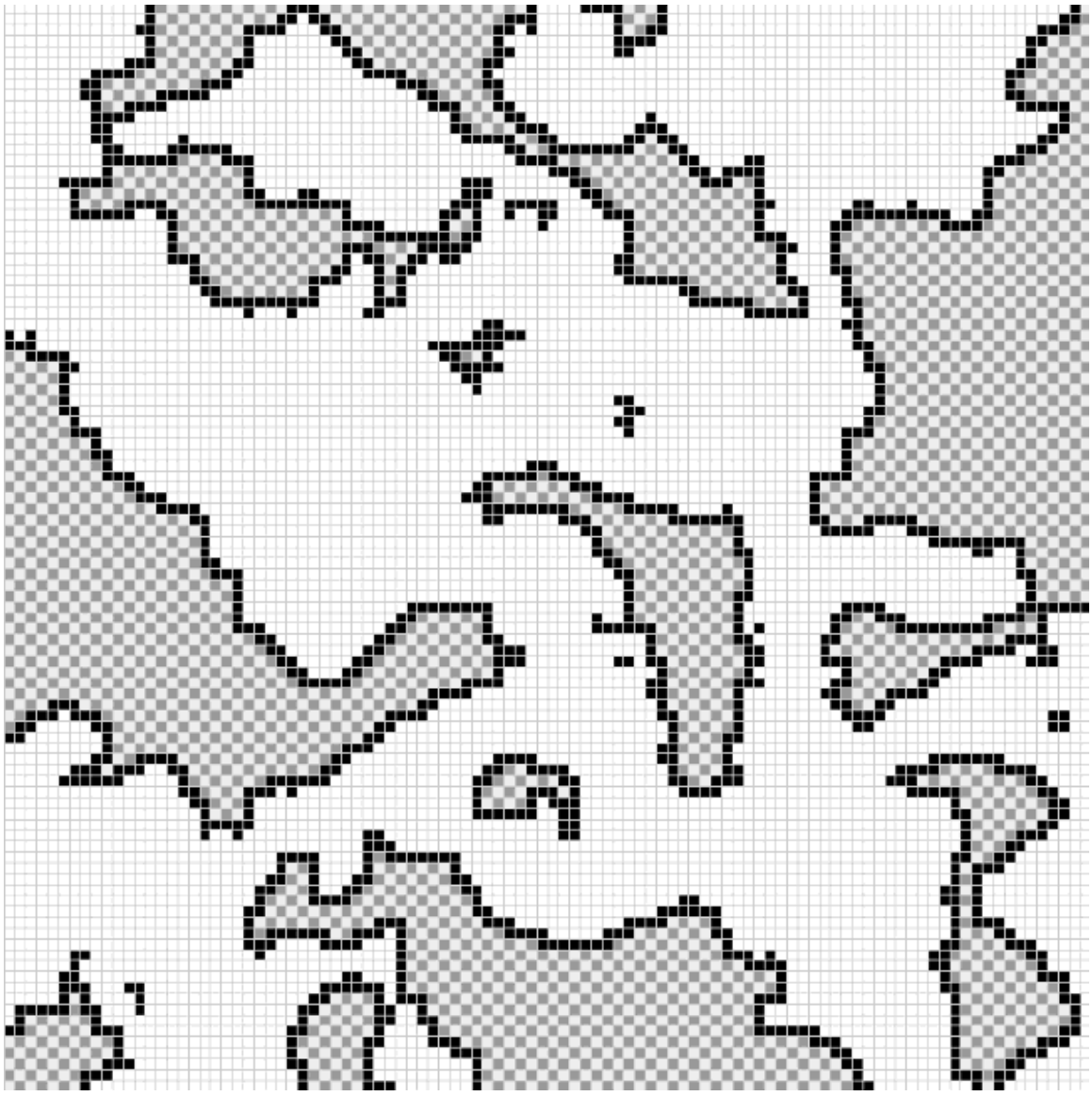

Figure 3.1: Node classification: black nodes represent boundary solids, checkered nodes represent isolated solids, and white nodes represent fluid particles (Sukop and Thorne, 2005)

3.1.1 Lattice Boltzmann Equation

The Lattice Boltzmann equation is derived from the Boltzmann transport equation; analyzing a system of particles excluding external forces, the Boltzmann transport equation is depicted in Equation 3.1:

$$\frac{\partial f}{\partial t} + v \bullet \nabla_x f = \Omega, \tag{3.1}$$

where $f(x, v, t)$ represents the particle distribution function (the particle distribution function represents a fraction of particles at time t with positions in the interval $[x, x + dx]$ and particle velocities in the interval $[v, v + dv]$); and Ω represents the collision operator. Because the collision operator, depicted in Equation 3.2, is a function of the particle distribution function, the analytical solution of Equation 3.1 is complicated; as a result, the collision operator is frequently approximated with the BGK approximation depicted in Equation 3.3:

$$\Omega = \int_{R^3}^{\infty} \int_{S^2}^{\infty} \sigma(\alpha)|v - w| \left[f(x, v', t) f(x, w', t) - f(x, v, t) f(x, w, t)\right] d\alpha dw, \tag{3.2}$$

$$\Omega = \frac{1}{\tau}(f^{eq} - f) = \omega(f^{eq} - f). \tag{3.3}$$

Equation 3.2 defines the expansion of the collision operator; α represents solid angles, $\sigma(\alpha)$ represents the differential cross section, f represents the particle distribution function, v and w represent particle velocities pre-collision, v' and w' represent particle velocities port-collision, x represents position, and t represents time. In Equation 3.3, Ω represents the collision operator, τ represents the relaxation factor, f^{eq} represents the local equilibrium distribution function, f represents the particle distribution function, and ω represents the collision frequency; using the BGK collision operator approximation, Equation 3.1 becomes Equation 3.4:

$$\frac{\partial f}{\partial t} + v \bullet \nabla_x f = \frac{1}{\tau}(f^{eq} - f). \quad (3.4)$$

To conserve energy and momentum in the three-dimensional lattice, particle collisions are modeled as elastic collisions; as a result, the realization of Equation 3.5 and Equation 3.6 are required (Heubes, 2010):

$$v + w = v' + w', \quad (3.5)$$

$$|v|^2 + |w|^2 = |v'|^2 + |w'|^2. \quad (3.6)$$

Analyzing a finite collection of particle velocities, particle distribution functions, and local equilibrium distribution functions, Equation 3.3 becomes the discrete Boltzmann transport equation depicted in Equation 3.7; the discretization of Equation 3.7 generates Equation 3.8:

$$\frac{\partial f_i}{\partial t} + v_i \bullet \nabla_{x_i} f_i = \frac{1}{\tau}\left(f_i^{eq} - f_i\right),\ i = 0 \ldots m-1\,, \quad (3.7)$$

$$\frac{f_i(x,t+\Delta t) - f_i(x,t)}{\Delta t} + v_i \frac{f_i(x+\Delta x, t+\Delta t) - f_i(x,t+\Delta t)}{\Delta x} = \frac{1}{\tau}\left(f_i^{eq}(x,t) - f_i(x,t)\right), i = 0 \ldots m-1,$$

$$v_i = \frac{\Delta x_i}{\Delta t},$$

$$\frac{f_i(x,t+\Delta t) - f_i(x,t)}{\Delta t} + \frac{f_i(x+v_i\Delta t, t+\Delta t) - f_i(x,t+\Delta t)}{\Delta t} = \frac{1}{\tau}\left(f_i^{eq}(x,t) - f_i(x,t)\right), i = 0 \ldots m-1,$$

$$\frac{f_i(x+v_i\Delta t) - f_i(x,t)}{\Delta t} = \frac{1}{\tau}\left(f_i^{eq}(x,t) - f_i(x,t)\right), i = 0 \ldots m-1,$$

$$f_i(x + v_i\Delta t, t + \Delta t) = f_i(x,t) + \frac{\Delta t}{\tau}\left(f_i^{eq}(x,t) - f_i(x,t)\right), i = 0 \ldots m-1. \quad (3.8)$$

The Lattice Boltzmann equation is depicted in Equation 3.8. The macroscopic rules defining fluid particles adhere to Equations 3.9 and 3.10 (Gabbana, 2015):

$$\rho = \sum_i f_i, \tag{3.9}$$

$$\rho u = \sum_i f_i v_i, \tag{3.10}$$

where ρ represents the fluid density, u represents the fluid velocity, f_i represents particle distribution functions, and v_i represents particle velocities.

3.1.2 Lattice Boltzmann Models

Associated with the Lattice Boltzmann models and collision rules presented from numerous researchers, multiple Lattice Boltzmann algorithms have been developed. Three-dimensional Lattice Boltzmann algorithms, D3Q15, D3Q19, and D3Q27, are differentiated through the number of allowable particle velocity directions and the numeric value of weighing factors. In the algorithm naming conventions, "D3" refers to the use of a 3-dimensional lattice, while the number following "Q" refers to the number of velocity directions. Particle velocities used throughout Lattice Boltzmann models enhance the accuracy of the model; however, additional particle velocities increase the computational demand of the fluid flow simulation.

The particle velocities associated with the Lattice Boltzmann models have lengths of $\sqrt{3}$, $\sqrt{2}$, and 1; the particle velocities associated with the D3Q19 Lattice Boltzmann model are $\sqrt{2}$ and 1. The allowable velocity vectors originating from (0,0,0) are:

- $c_0 = (0,0,0)$
- $c_1 = (1,0,0)$
- $c_2 = (0,1,0)$
- $c_3 = (-1,0,0)$
- $c_4 = (0,-1,0)$
- $c_5 = (0,0,1)$
- $c_6 = (0,0,-1)$
- $c_7 = (1,1,0)$
- $c_8 = (-1,1,0)$
- $c_9 = (-1,-1,0)$
- $c_{10} = (1,-1,0)$
- $c_{11} = (1,0,1)$
- $c_{12} = (-1,0,1)$
- $c_{13} = (-1,0,-1)$
- $c_{14} = (1,0,-1)$
- $c_{15} = (0,1,1)$
- $c_{16} = (0,-1,1)$
- $c_{17} = (0,-1,-1)$
- $c_{18} = (0,1,-1)$.

The weighing functions associated with the D3Q19 Lattice Boltzmann model have magnitudes of $\frac{1}{3}$, $\frac{1}{18}$, and $\frac{1}{36}$:

$$\omega_i = \begin{cases} \frac{1}{3} & i = 0 \\ \frac{1}{18} & i = 1,2,3,4,5,6 \\ \frac{1}{36} & i = 7,8,9,10,11,12,13,14,15,16,17,18 \end{cases}.$$

The selection of three-dimensional Lattice Boltzmann models defines the local equilibrium distribution function, f_i^{eq}, depicted in Equation 3.11:

$$f_i^{eq} = \rho\omega_i \left[1 + \frac{v_i \bullet u}{c_s^2} + \frac{(v_i \bullet u)^2}{2c_s^4} - \frac{u^2}{2c_s^2}\right], i = 0 \ldots m-1, \quad (3.11)$$

where f_i^{eq} represents the local equilibrium distribution function, ρ represents the fluid density, ω represents the model specific weighing functions, v represents velocity vectors, u represents fluid velocity, and c_s represents the speed of sound. The speed of sound, c_s, is a lattice constant equivalent to $\frac{1}{\sqrt{3}}$, irrespective of the three-dimensional Lattice Boltzmann algorithm used.

To determine the permeability of the numerically simulated porous media, the Shan and Chen (1993) D3Q19 Lattice Boltzmann method was used.

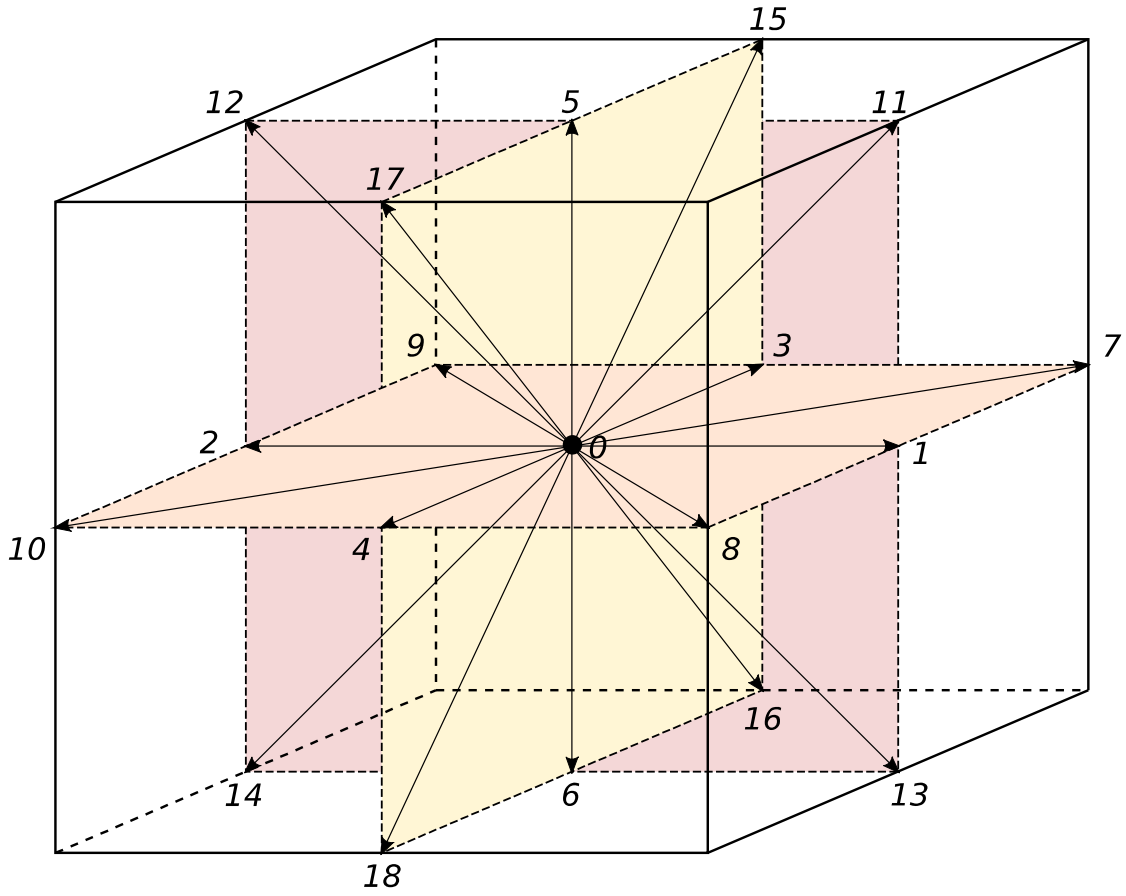

Figure 3.2: D3Q19 Lattice Boltzmann model (Gabbana, 2015)

Figure 3.2 depicts the D3Q19 Lattice Boltzmann model; Palabos was used to determine permeability estimates for the numerically constructed porous media. The Shan and Chen and D3Q19 Lattice Boltzmann method was used because of the algorithm's accuracy and

moderate computational requirements. Together with the Shan and Chen Lattice Boltzmann model, the BGK collision operator approximation and bounce-back boundary conditions were used. The collision operator is depicted in Equation 3.2; the BGK collision operator approximation is depicted in Equation 3.3. Bounce-back boundary conditions were used because of the boundary conditions' ability to replicate complex porous media geometries.

3.2 Porous Media Geometry Model Description

The proposed research topic was to analyze the relationship between grain size, mean grain size, median grain size, and mode grain size; grain size standard deviation; and absolute permeability through the amalgamation of numerical modeling and laboratory measurements for marine sands and muds with uni-, bi-, and tri-modal grain size distributions. I used the Lattice Boltzmann method to determine the absolute permeability of numerically constructed three-dimensional porous media with partially imbricated spherical grains exhibiting narrow grain size distributions. To construct the three-dimensional porous media, multiple variables were analyzed: experimental data, tessellation algorithm, Lattice Boltzmann models, boundary conditions, and representative volume element effects.

Laboratory measurements of mudstone core were used to construct porous media exhibiting narrow grain size distributions. Daigle and Screaton (2014) performed sieve analysis on the mudstone core sample to determine the grain size distribution of the core. Figure 3.3 depicts the grain size distribution of the core sample. I determined statistical parameters, including mean grain size (μ) and grain size standard deviation (σ), for the core sample using regression analysis assuming a lognormal distribution of grain size distribution (Equation 3.12):

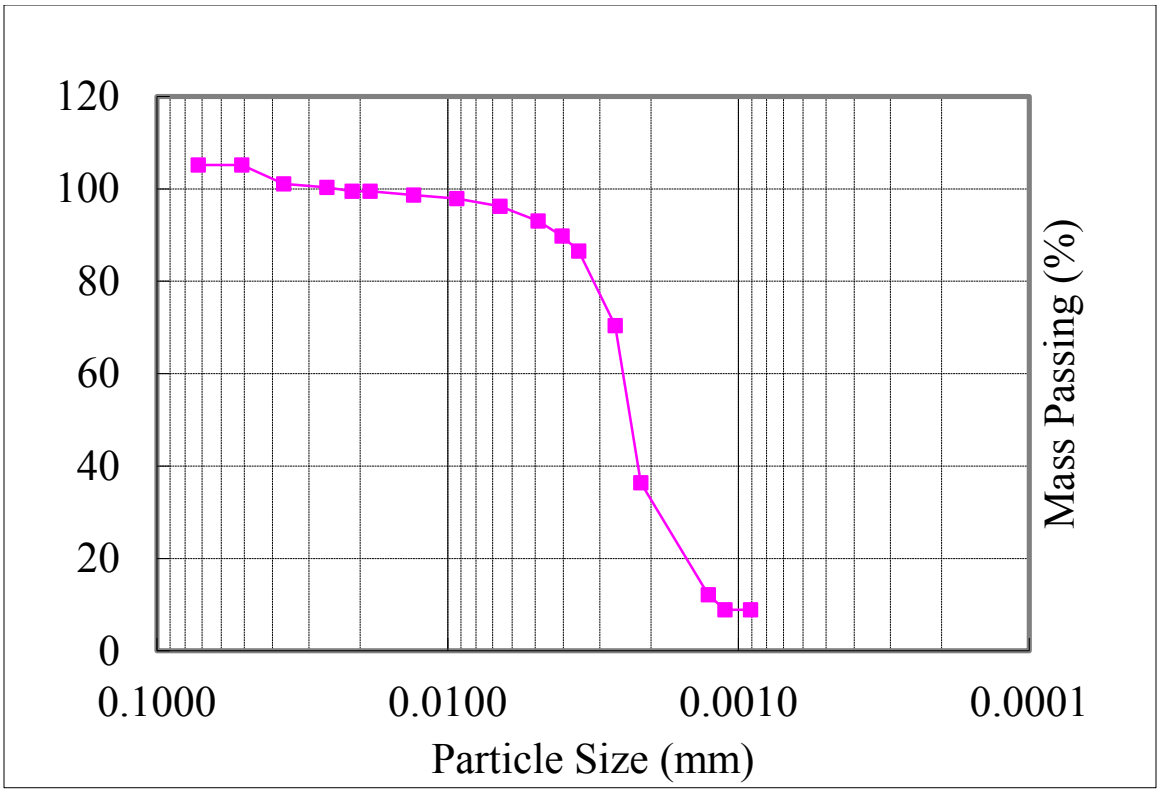

Figure 3.3: Grain size distribution for mudstone core exhibiting a narrow grain size distribution (Daigle and Screaton, 2014)

$$CDF(x) = \frac{1}{2} + \frac{1}{2}\mathrm{erf}\left[\frac{\ln(x) - \mu}{\sqrt{2}\sigma}\right], \tag{3.12}$$

where CDF represents the cumulative distribution function for grain size (x). Figure 3.2 depicts normalized grain radii for a Pacific Ocean mudstone core exhibiting a narrow grain size distribution; the length of the experimental core, 25.4 millimeters, was used to normalize grain radii values to define grain radii in lattice units. The normalized grain size mean and normalized grain size standard deviation for the data depicted in Figure 3.2 are 0.000044 and 0.4650 respectively. I used the mudstone core to determine reference parameters for the numerically simulated porous media. The standard deviations for numerically simulated porous medium models were 1σ, 0.75σ, and 0.50σ utilizing the

reference standard deviation, σ. I determined the reference standard deviation from the mudstone core; the reference standard deviation was determined to be approximately 0.4650. Statistical parameters are used in the algorithm to construct porous media of variable complexity exhibiting narrow grain size distributions; standard deviation values of 0.4650, 0.3488, and 0.2325 were used to construct porous media exhibiting variable narrow grain size distributions.

Complex geometries are represented in Lattice Boltzmann models through a three-dimensional cubic lattice. Lattice Boltzmann models emulate complex boundaries with elementary boundaries as depicted in Figure 3.4.

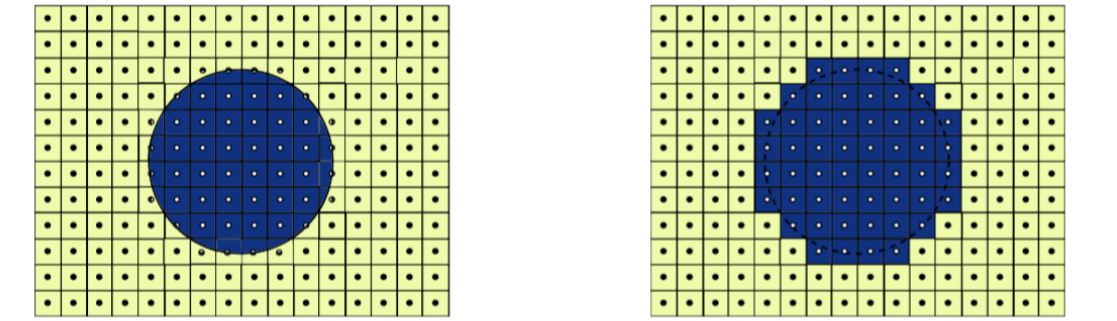

(a) Complex Boundary Conditions. **(b)** Elementary Boundary Conditions.

Figure 3.4: Complex boundaries represented as a series of elementary boundaries (Gabbana, 2015)

I used elementary boundaries to effectively represent numerically simulated three-dimensional porous media. To determine the minimum quantity of voxels required to effectively represent the porous media, a cubic packing model consisting of uniform spheres was used; Figure 3.5 depicts an image of the cubic packing model.

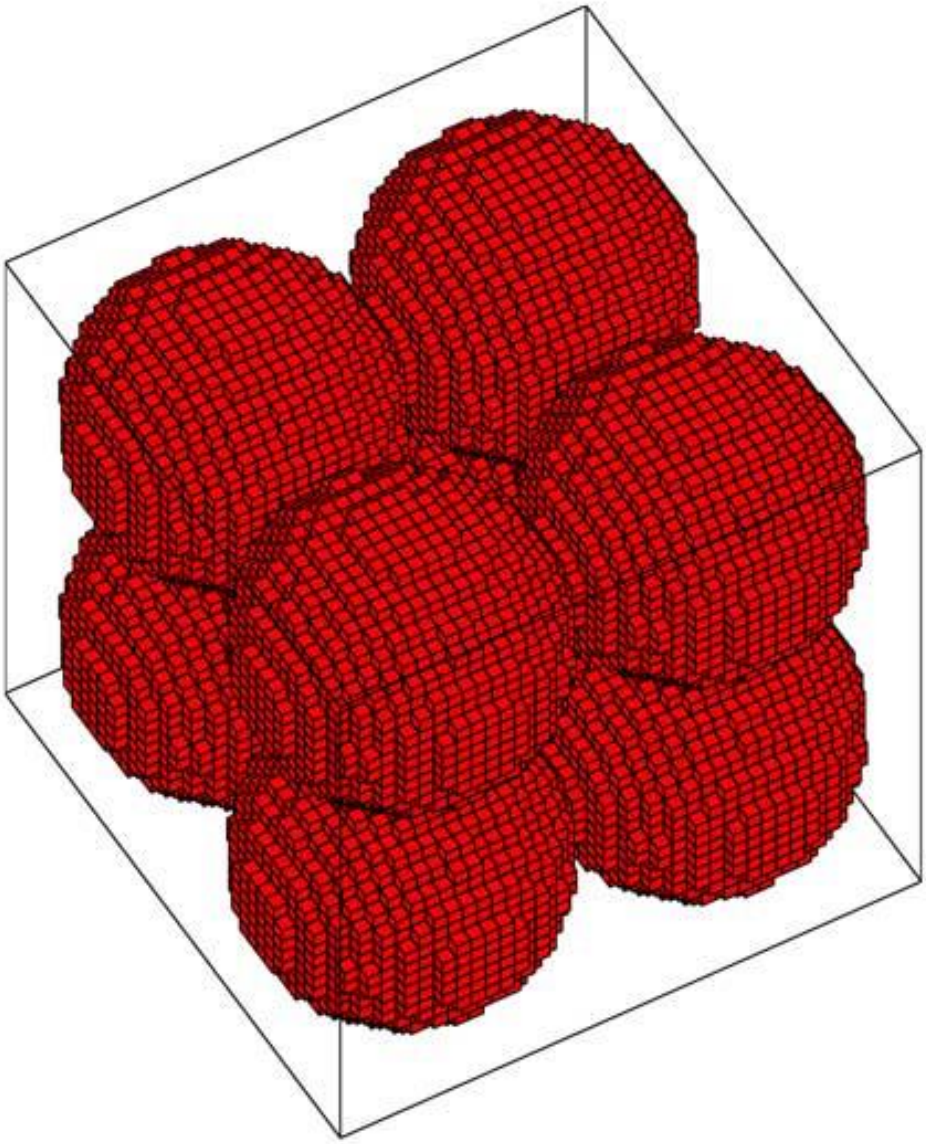

Figure 3.5: Cubic packing model (Pan et al., 2004)

I used the cubic packing model to determine the minimum voxel quantity required to obtain accurate porosity estimates because of the established properties of cubic packing models. Cubic packing models exhibit constant porosity values of approximately 0.467; as a result, the minimum voxel quantity required to obtain the derived porosity value was analyzed. Figure 3.6 analyzes the relationship between voxel quantity and numerically determined porosity values; analyzing Figure 3.6, a minimum pixel quantity of 248^3 is

required to minimize the error between the numerically determined porosity and the derived reference porosity for cubic packing models. Using a pixel quantity of 248^3 results in relative error of approximately - 0.00010; the voxel quantity was minimized to reduce the computational requirements of the numerical simulation.

The Lattice Boltzmann method uses cubic pixels to replicate complex boundaries; as a result, porous media simulations restricted grain diameters to a minimum length of 3 lattice units to maintain accurate representation of grain geometry. To achieve the minimum lattice sphere diameter of 3 lattice units, the mean of the normal distribution was shifted; the normal distribution defined the minimum sphere diameter as 3 standard deviations to the left of the mean. Integrating normalized standard deviation and normalized mean values, numerically simulated porous media were constructed; the porosity values of numerically simulated porous media varied between approximately 10 and 40 percent.

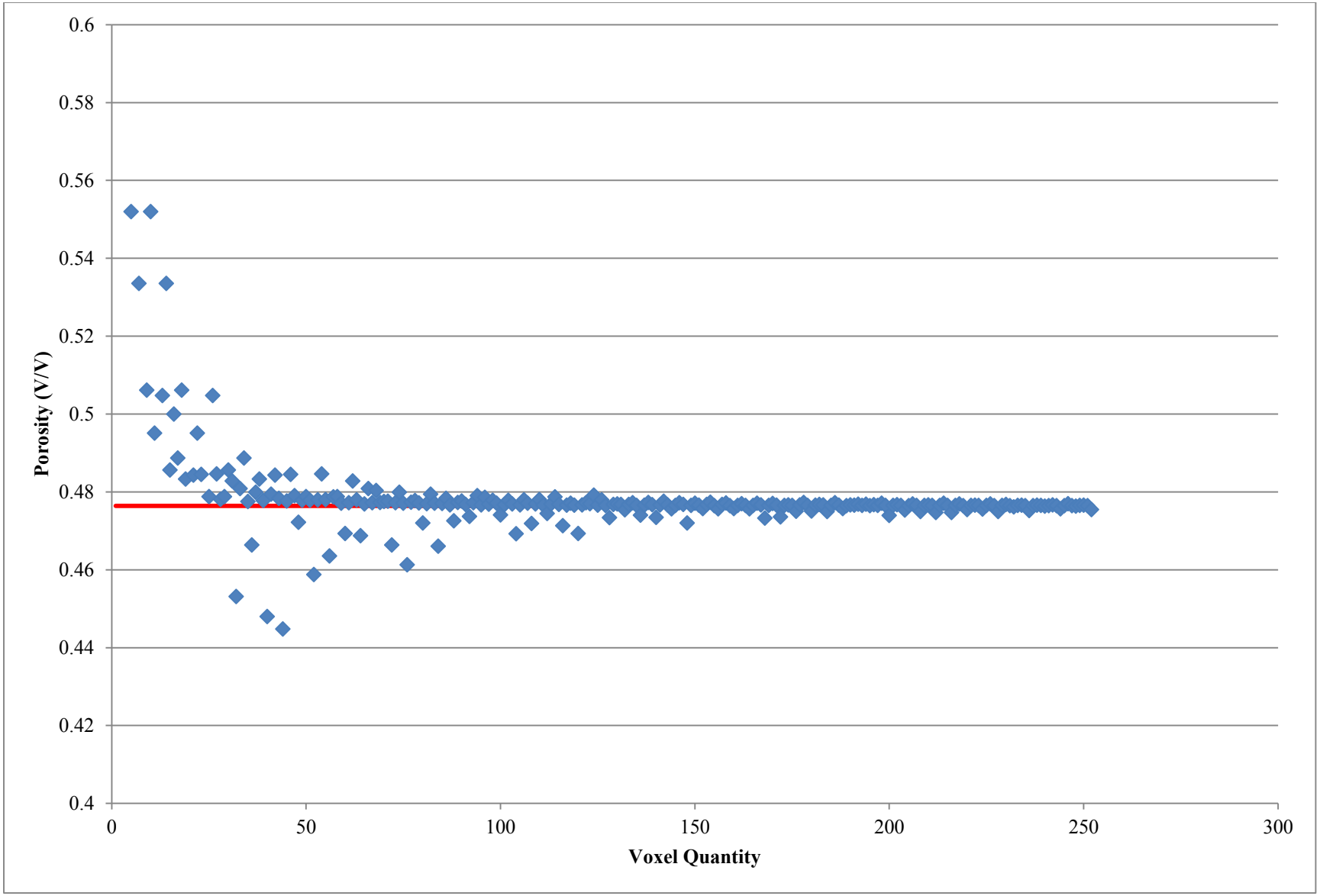

Figure 3.6: Minimum pixel quantity along the x-axis required to characterize the porosity of porous media

3.3 BOUNDARY CONDITIONS

Analogous to the boundary conditions defined between fluid and solid particles, boundary conditions between spherical grains and the lattice were required. Lattice boundary volumes define the interactions between spherical grains and three-dimensional lattice boundaries. To determine the appropriate lattice-grain interaction, multiple boundary volumes were analyzed, lattice constrained, centroid constrained, and lattice unconstrained; sphere packing models used to analyze boundary volumes were constructed using Illustration 1 in the Appendix.

Lattice constrained boundary volumes restrict spherical grains' positions within the defined lattice. Lattice constrained boundary volumes preclude the imbrication of spherical grains and lattice boundaries (cubic lattice). Figure 3.7 depicts an image of lattice constrained boundary volumes.

The lattice boundary volumes depicted in Figure 3.7, exhibit abnormal fluid dynamics. Figure 3.8 depict the velocity magnitudes for permeability simulations; Figure 3.9 and Figure 3.10 depict the velocity distributions for flow regimes through the inlet and center of the porous media along the x-axis; the porous media exhibit porosity values of 0.4018 and 0.2107 respectively.

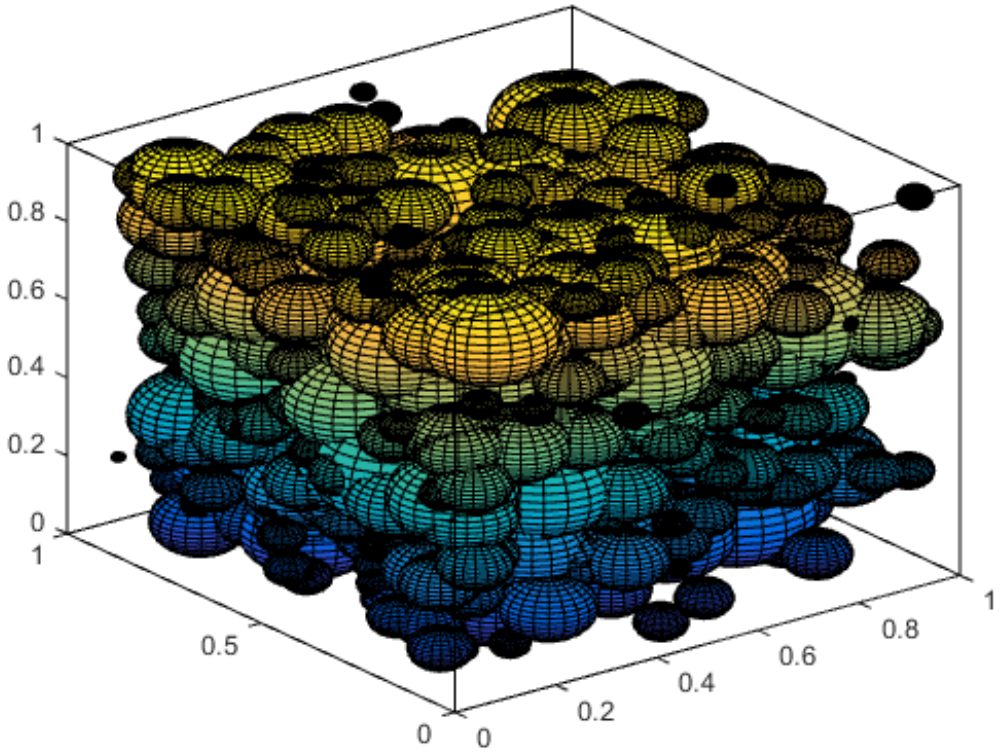

Figure 3.7: Porous medium constructed utilizing lattice constrained boundary conditions exhibiting a porosity of 0.4018

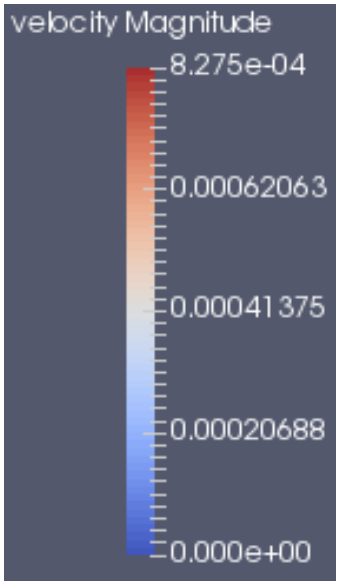

Figure 3.8: Velocity magnitude for permeability simulations

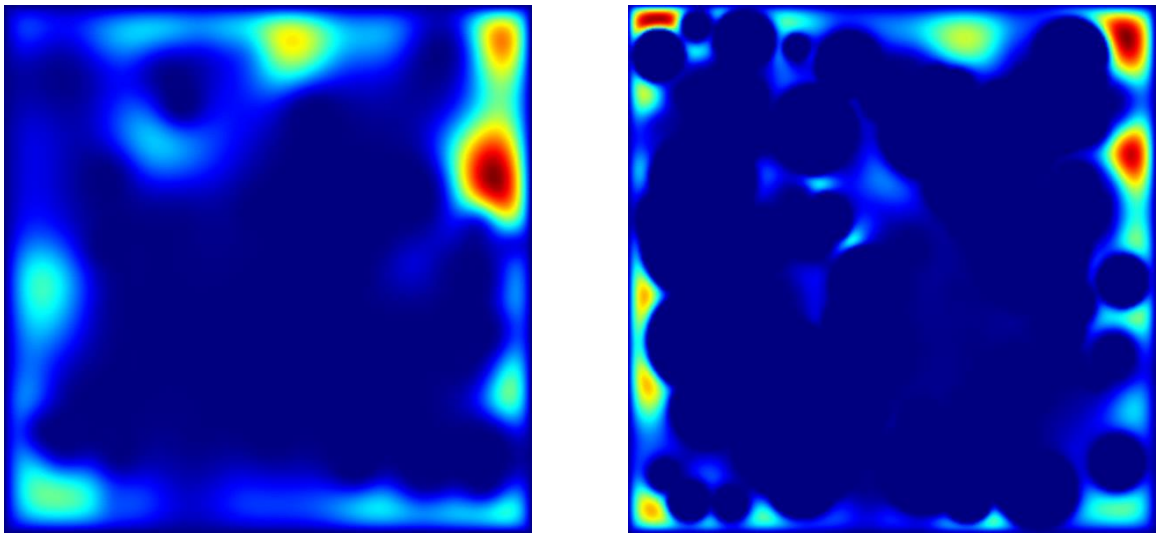

Figure 3.9: Inlet (left) and median (right) velocity profiles at iteration 7500 for porous medium exhibiting a porosity of 0.4018

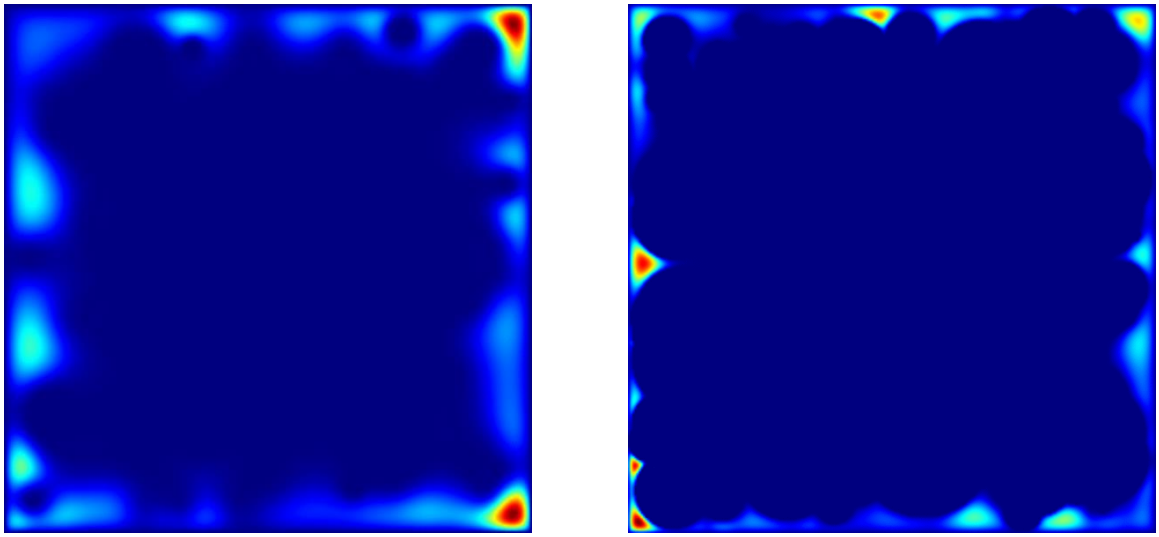

Figure 3.10: Inlet (left) and median (right) velocity profiles at iteration 180500 for porous medium exhibiting a porosity of 0.2107

Figure 3.9 depicts an amalgamation of wall flow and body flow; however, as the porosity decreases the porous media exhibit wall flow, fluid flows along the interface of the lattice face and spherical grains, exclusively. Figure 3.10 exhibits wall flow exclusively because of the reduced porosity value. Lattice constrained boundary volumes exhibited abnormal

fluid dynamics; as a result, lattice constrained boundary volumes were determined to be inappropriate for the numerical models.

Centroid constrained boundary volumes restrict the centroid of spherical grains within the defined lattice. Centroid constrained boundary volumes facilitate the imbrication of spherical grains and lattice boundaries; Figure 3.11 depicts an image of centroid constrained lattice boundary volumes.

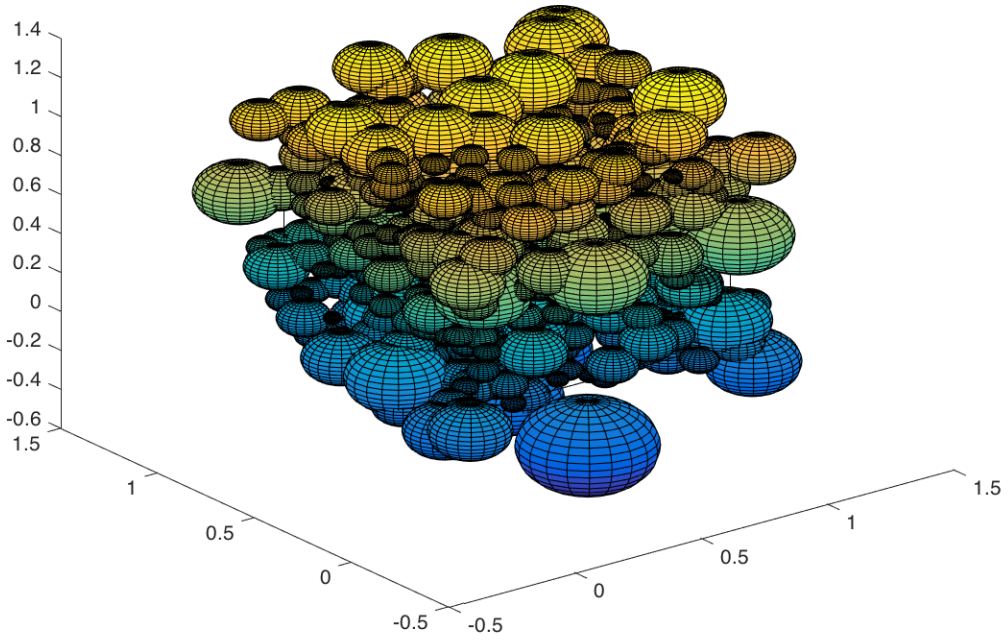

Figure 3.11: Porous medium constructed utilizing centroid constrained boundary conditions exhibiting a porosity of 0.3892

The lattice boundary volumes depicted in Figure 3.11 exhibit anticipated fluid dynamics. Figures 3.12 through Figure 3.14 depict the velocity distributions for flow regimes through the inlet and centroid of the porous media along the x-axis; the porous media exhibit porosity values of 0.3892, 0.2089, and 0.0996 respectively.

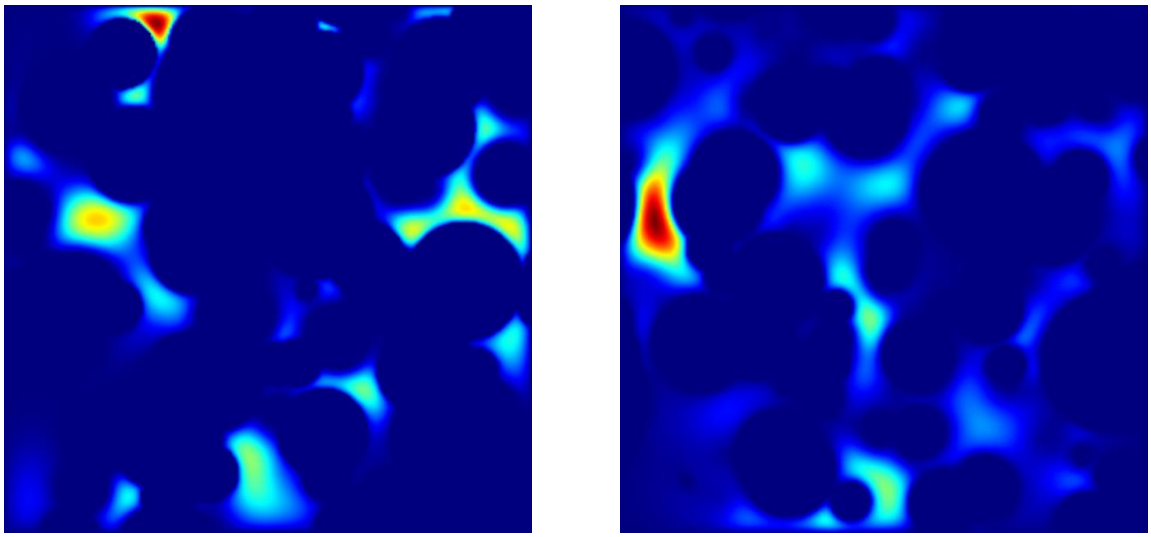

Figure 3.12: Inlet (left) and median (right) velocity profiles at iteration 38500 for porous medium exhibiting a porosity of 0.3892

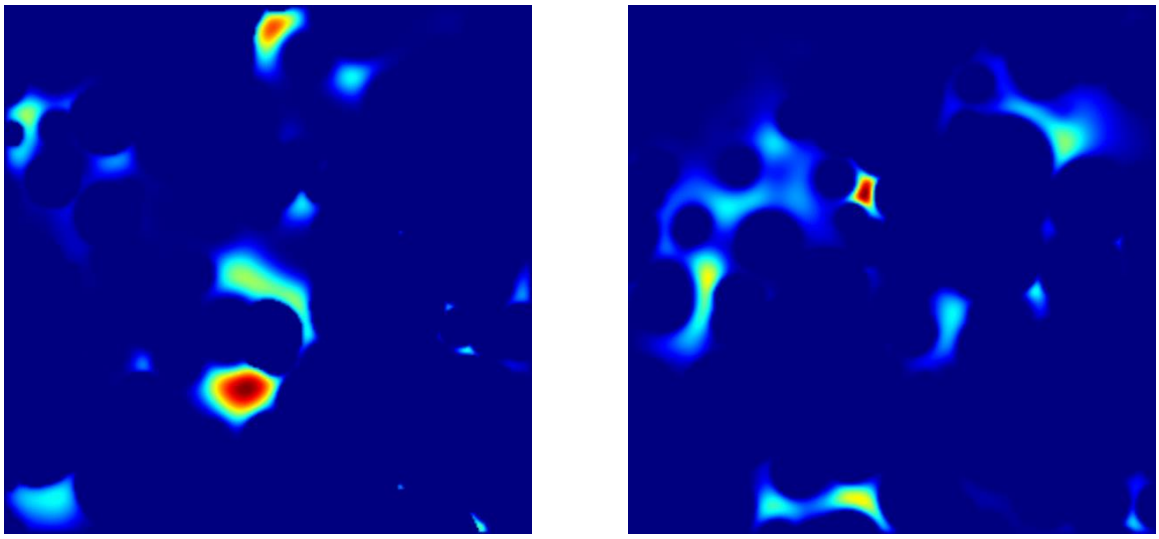

Figure 3.13: Inlet (left) and median (right) velocity profiles at iteration 141000 for porous medium exhibiting a porosity of 0.2089

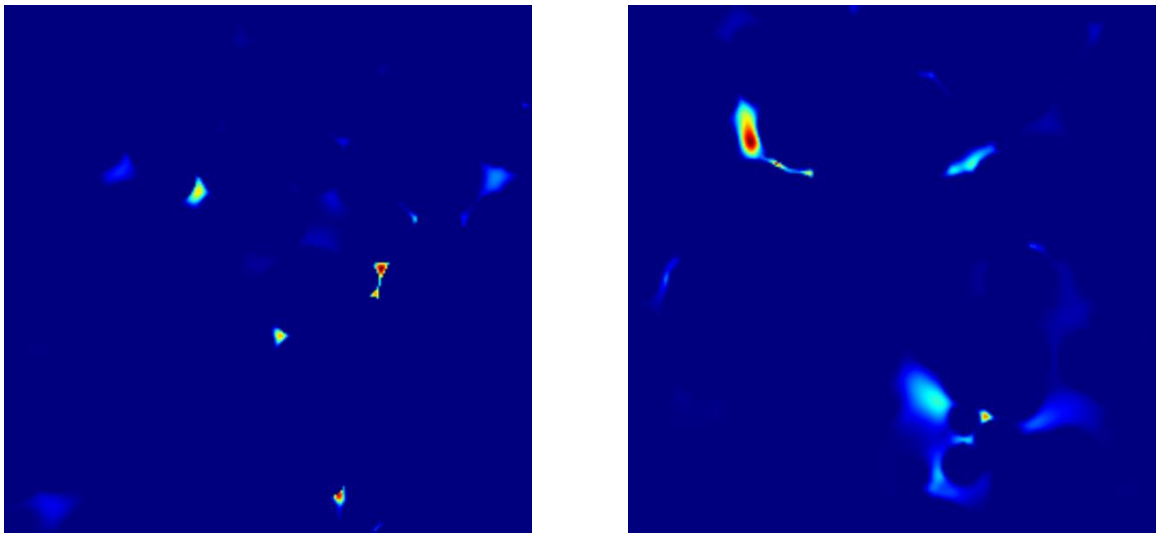

Figure 3.14: Inlet (left) and median (right) velocity profiles at iteration 652000 for porous medium exhibiting a porosity of 0.2089

Figures 3.12 through Figure 3.14 exhibit fluid dynamics governed principally through body flow irrespective of porous media porosity values; Figures 3.12 through Figure 3.14 exhibit minimal wall flow. Centroid constrained boundary volumes mitigate abnormal fluid dynamics; as a result, centroid constrained boundary volumes were determined to be appropriate boundary conditions for the numerical models.

Lattice unconstrained boundary volumes permits spherical grain centroids to be positioned internal or external to defined lattice boundaries. Lattice unconstrained boundary volumes permit the imbrication of spherical grains and lattice boundaries; Figure 3.15 depicts an image of lattice unconstrained boundary volumes.

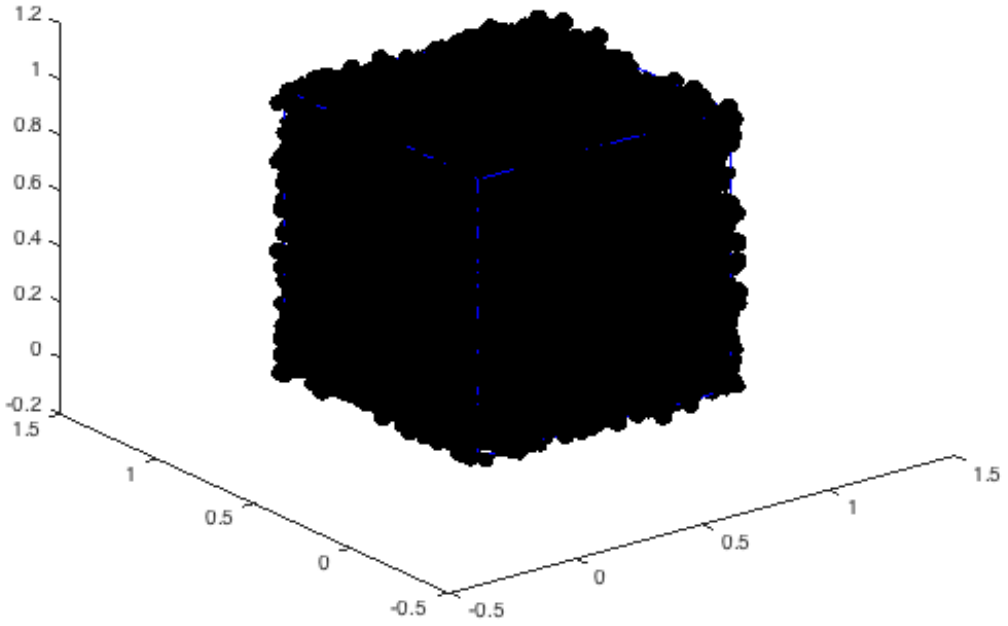

Figure 3.15: Porous medium constructed utilizing lattice unconstrained boundary conditions exhibiting a porosity of 0.4229

The lattice boundary volumes depicted in Figure 3.15 exhibit anticipated fluid dynamics. Figures 3.16 through Figure 3.18 depict the velocity distributions for flow regimes through the inlet and centroid of the porous media along the x-axis; the porous media exhibit porosity values of 0.4229, 0.2178, and 0.1365 respectively.

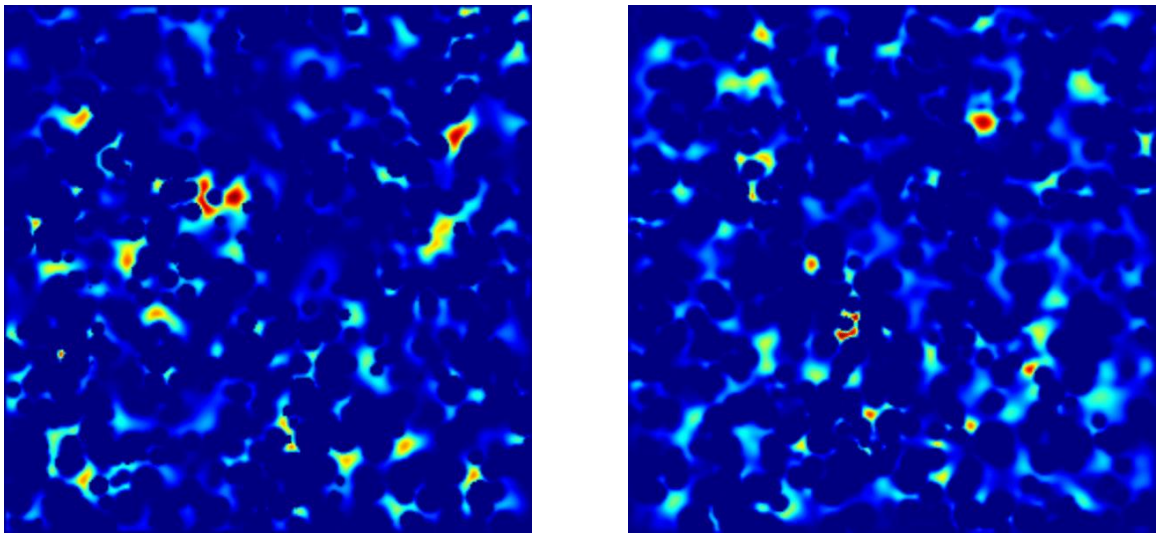

Figure 3.16: Inlet (left) and median (right) velocity profiles at iteration 177000 for porous medium exhibiting a porosity of 0.4229

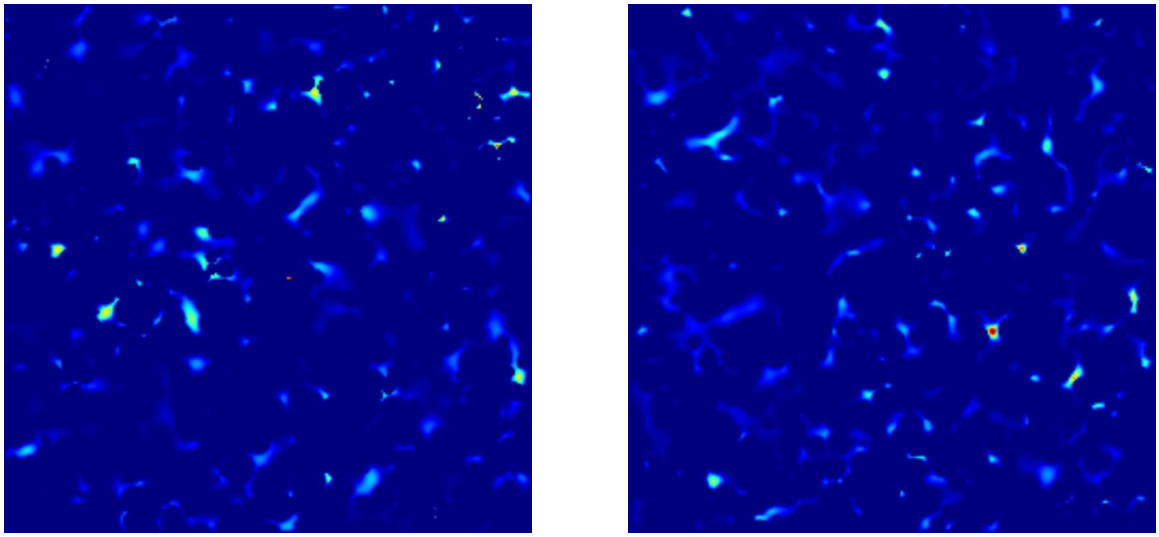

Figure 3.17: Inlet (left) and median (right) velocity profiles at iteration 533000 for porous medium exhibiting a porosity of 0.2178

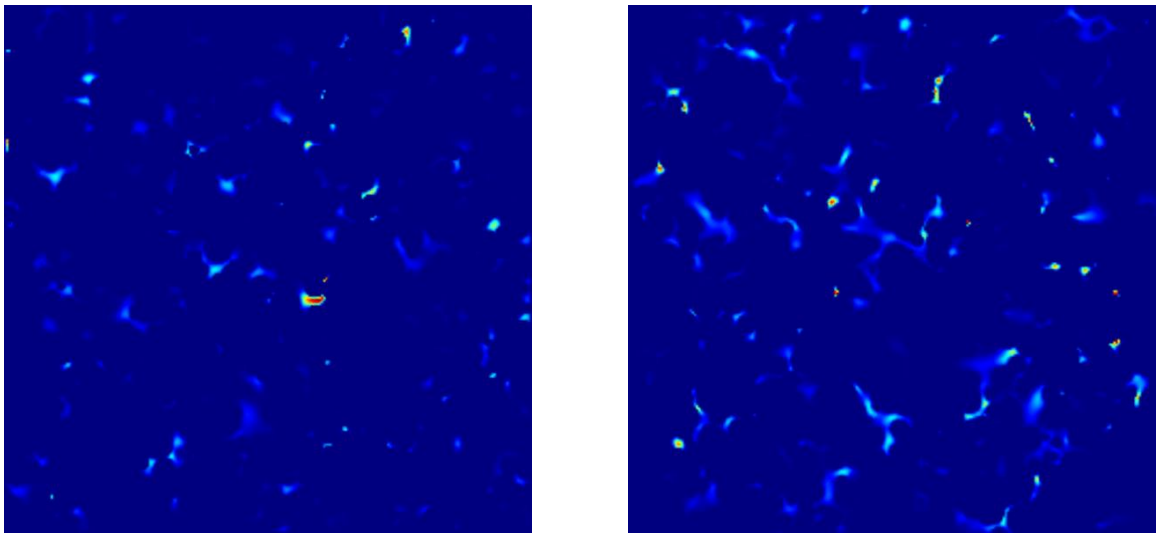

Figure 3.18: Inlet (left) and median (right) velocity profiles at iteration 470000 for porous medium exhibiting a porosity of 0.1365

Figures 3.16 through Figure 3.18 exhibit fluid dynamics governed principally through body flow irrespective of porous media porosity values; Figures 3.16 through Figure 3.18 exhibit minimal wall flow. Similar to centroid constrained boundary volumes, lattice unconstrained boundary volumes mitigate abnormal fluid dynamics; therefore, lattice unconstrained boundary conditions were determined to be appropriate boundary conditions for the numerical models.

Lattice unconstrained boundary volumes and centroid constrained boundary volumes exhibit fluid dynamics governed principally through body flow with minimal wall flow; however, lattice unconstrained boundary volumes physically replicate the core extraction procedure. Experimental cores are extracted from predefined locations; however, the geospatial positions of grain particles are ambiguous. To replicate the ambiguous geospatial positions of grain particles internal to experimental core, lattice unconstrained boundary volumes were used to construct numerical models.

Meticulous representation of spherical grains and lattice-grain interaction is essential to effectively represent the fluid dynamics of the numerical models; therefore, representative volume element effects were analyzed. Representative volume element

effects occur when image analysis is unable to accurately represent the pore space of the porous medium; subsequently, impractical fluid dynamics occur. The constructed numerical models represent unconsolidated porous media; therefore, estimated transport properties should depict approximately equivalent values along the x, y, and z flow directions. To mitigate representative volume element effects, the maximum grain diameter in reference to lattice length was determined for numerical models exhibiting standard deviations of 0.4650, 0.3488, and 0.2325 and porosities of approximately 0.40, 0.20, and 0.10; Figures 19 through Figure 21 depict permeability ratios of $\frac{k_x}{k_y}$, $\frac{k_x}{k_z}$, and $\frac{k_y}{k_z}$ used to determine the appropriate representative volume element for porous media simulations.

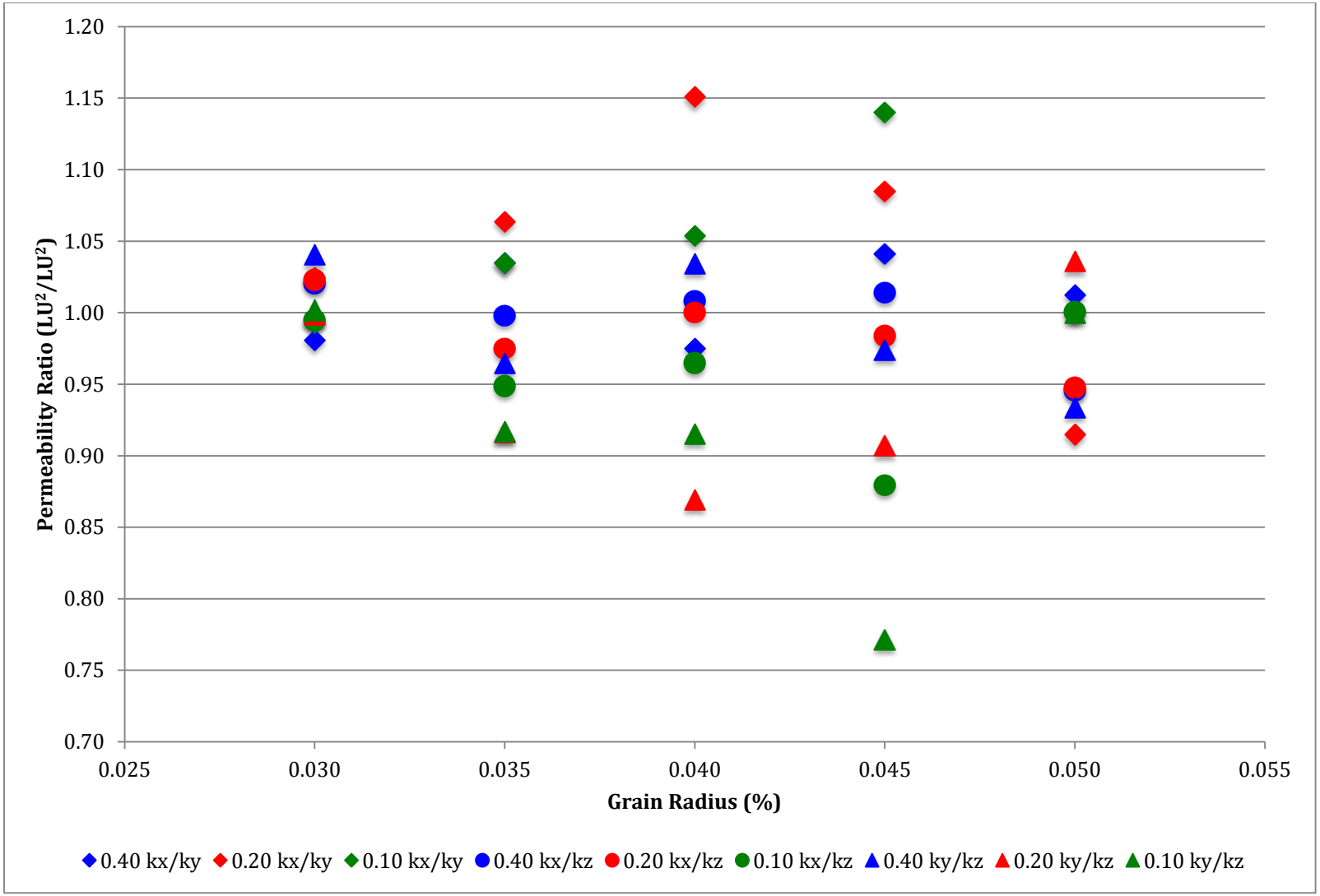

Figure 3.19: Maximum permitted grain radius as a percent of lattice length for porous media exhibiting an estimated standard deviation of 0.4650. The numbers in the symbol labels correspond to porosity values, while the ratio indicates which permeability components are being compared.

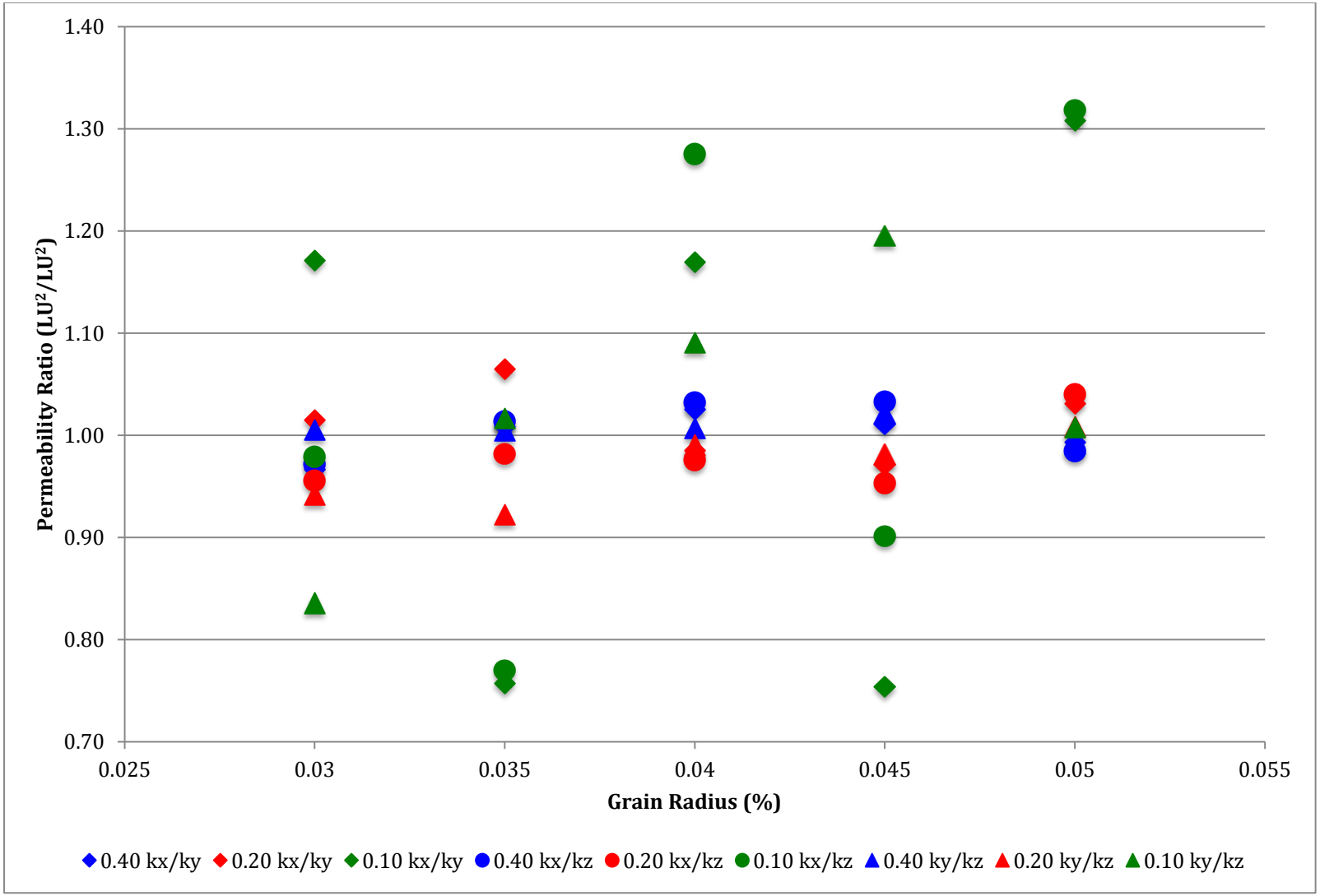

Figure 3.20: Maximum permitted grain radius as a percent of lattice length for porous media exhibiting an estimated standard deviation of 0.3488. The numbers in the symbol labels correspond to porosity values, while the ratio indicates which permeability components are being compared.

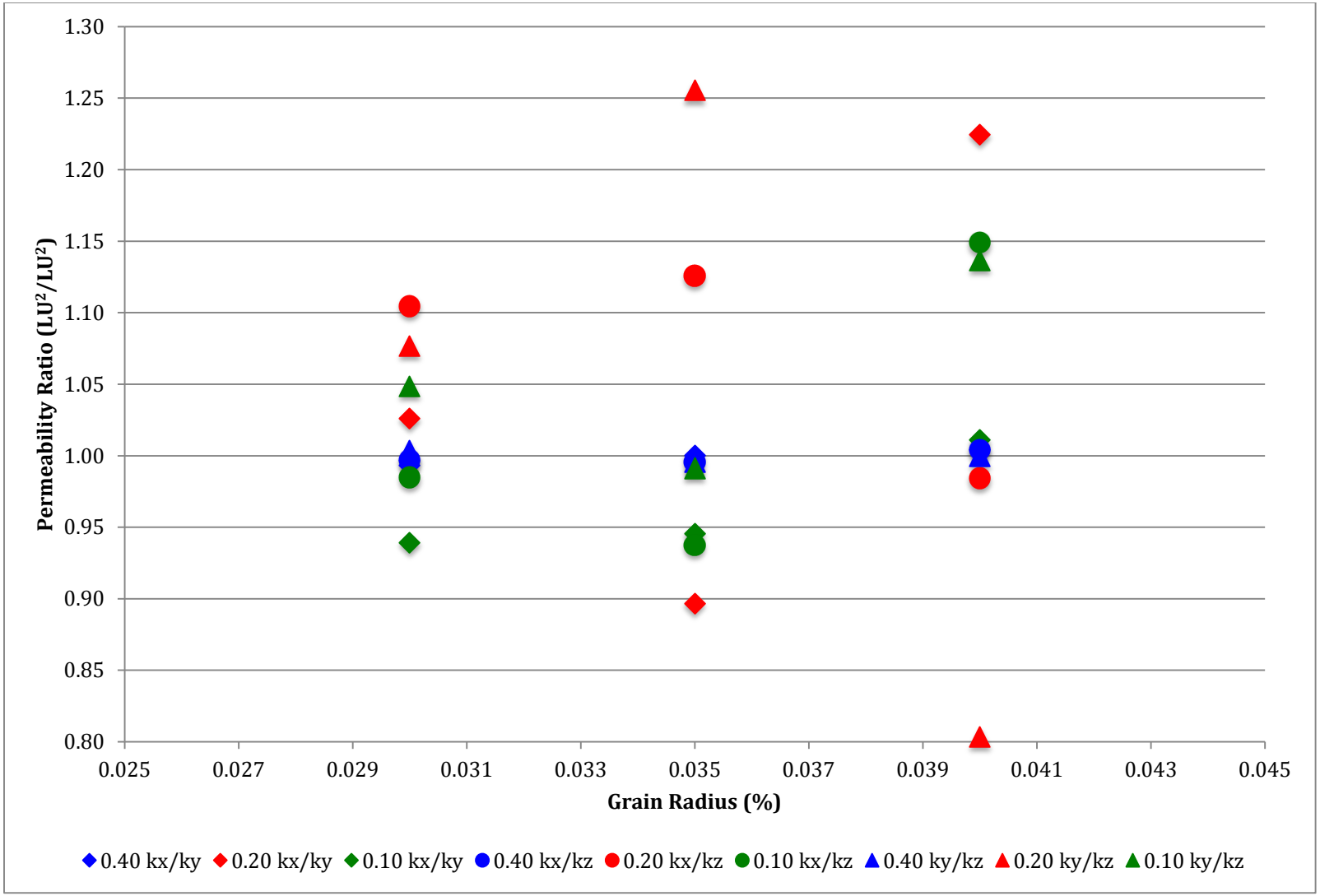

Figure 3.21: Maximum permitted grain radius as a percent of lattice length for porous media exhibiting an estimated standard deviation of 0.2325. The numbers in the symbol labels correspond to porosity values, while the ratio indicates which permeability components are being compared.

To mitigate representative volume element effects, the difference between transport properties along the x, y, and z flow directions is minimized; Figures 19 through Figure 21 depict ratios of permeability values in the x, y, and z flow directions. Analyzing Figures 19 through Figure 21, the maximum grain radii for numerical models exhibiting standard deviations of 0.4650, 0.3488, and 0.2325 mm was determined to be approximately 3 percent of the lattice length. The implementation of a maximum grain radius enables the numerical models to effectively represent the pore space of the porous media; as a result, estimated transport properties are enhanced.

The defined techniques were used to construct numerical models. Numerical models were constructed with grain size standard deviations of 0.4650, 0.3488, and 0.2325 mm and variable porosity values; porosity values exhibited maximum and minimum values of approximately 0.40 and 0.10 respectively. The Shan and Chen (1993) Lattice Boltzmann model and BGK collision operator were used to estimate permeability values for the numerical simulations.

4. Discussion and Results

I analyzed the relationship between grain size, mean grain size, median grain size, and grain size mode; grain size standard deviation; and absolute permeability through the amalgamation of numerical modeling and experimental core data for sediments from the Pacific Ocean and Gulf of Alaska exhibiting uni-, bi-, and tri-model grain size distributions. To define the mode for sediments exhibiting multiple modes in the grain size distribution, the minimum mode value was used. The Pacific Ocean mudstone core was extracted from the Equatorial Pacific; Gulf of Alaska cores were extracted offshore southern Alaska along the Bering Trough. The present research topic extends present permeability research correlating absolute permeability and grain size. The Pacific Ocean mudstone sample was selected to characterize porous media exhibiting narrow grain size distributions; the Gulf of Alaska samples were selected to characterize porous media exhibiting broad grain size distributions. I performed numerical simulations of fluid flow through sphere packings with grain size distributions similar to that exhibited by the Pacific Ocean mudstone, and determined relationships between absolute permeability and grain size distribution parameters (mean, standard deviation). I then compared these relationships with those observed in laboratory measurements of the Gulf of Alaska samples, which had considerably broader grain size distributions.

4.1 NUMERICAL SIMULATIONS

The Pacific Ocean mudstone core was used to construct numerical models exhibiting narrow grain size distributions with a range of standard deviation values; Table 4.1 depicts petrophysical and statistical parameters for the Pacific Ocean mudstone core.

Core, section, Interval (cm)	Standard Deviation (mm)	Porosity (V/V)	Permeability (m^2)
U1396C, 2H-2, 60-65	0.4650	0.82	2.21E-16

Table 4.1: Data from grain size measurements (Daigle and Screaton, 2014)

The mudstone core was used to represent numerical models exhibiting narrow grain size distributions because the core was extracted in an area extremely distant from any terrigenous sediment input; as a result, the mudstone core consisted of clay and silt particles. The standard deviation of the mudstone core was used to create numerical models exhibiting narrow grain size distributions and variable standard deviation values. The mudstone core's standard deviation of 0.4650 was manipulated to construct porous media with estimated standard deviation values of 0.4650, 0.3488, and 0.2325 (i.e., 100%, 75% and 50% of the original value) and variable mean grain size values. The estimated mean grain sizes of the numerical models were determined using the minimum grain diameter, 3 lattice units, and the representative standard deviation values; to calculate the mean grain radius for the numerical models, three standard deviations were added to the minimum grain radius for the respective estimated standard deviation values. To construct numerical porous media, grain capacity, grain quantity depicted in the porous media model, was estimated and porosity values numerically determined. Figure 4.1 depicts the relationship between grain capacity and porosity for the constructed

numerical models; numerical models exhibit minimum and maximum grain capacities of 24,151 and 265,626 respectively.

Textural rock properties (grain capacity and standard deviation) were used to estimate secondary rock properties (porosity and permeability) for the numerically constructed porous media. Standard deviation values were estimated numerically using lognormal probability distribution functions, porosity values were estimated using numerical tessellation, and permeability values were estimated using Equation 4.1. Numerical simulations were constructed using dimensionless units; as a result, the Palabos algorithm reports permeability units as lattice units squared. Equation 4.1 converts the permeability of the numerical model (l.u.^{2}) to m^2; Equation 4.1 was derived from Equation 2.9.

$$k = \frac{\Phi^3}{36k_0(1-\Phi)^2}d^2, \tag{2.9}$$

$$\frac{k_n}{k_s} = \frac{\frac{\Phi_n^3}{36k_{0,n}(1-\Phi_n)^2}d_n^2}{\frac{\Phi_s^3}{36k_{0,s}(1-\Phi_s)^2}d_s^2},$$

assuming $k_{0,n} \cong k_{0,s}$ and $\Phi_n \cong \Phi_s$,

$$\frac{k_n}{k_s} = \frac{d_n^2}{d_s^2},$$

$$k_s = \frac{k_n d_s^2}{d_n^2},$$

$$k_p = \frac{k_n d_s^2}{d_n^2}\left[\frac{L_p}{L_{LBM}}\right]^2, \tag{4.1}$$

where Φ represents total porosity of the numerical model, n, and representative sample, s, probability distribution functions; k_0 represents the Kozeny-Carman constant, d_s represents the mean, median, or mode grain diameter of the core sample's probability

distribution function; d_n represents the mean grain diameter of the numerical model's probability distribution function; k represents the permeability of the numerical model, n, and representative sample, s, probability distribution functions; k_p represents the physical lattice permeability, and L represents the lattice length of the numerical model, LBM, and the physical model, p. The values of L_p and L_{LBM} used in Equation 4.1 were 1 inch and 248 lattice units respectively. Equation 4.1 was used to determine the permeability of representative core samples exhibiting the original grain size distributions and variable standard deviation values. Table 4.2 depicts the petrophysical and statistical parameters for the numerical porous media models. Examining Table 4.2, the numerical models exhibited minimum and maximum standard deviation, porosity, and permeability values of approximately 0.22269 to 0.30843 mm, 0.10 to 0.40, and 4.28E-14 to 6.68E-9 m^2. Table 4.2 examines the calculated permeability values of Equation 4.1 using mean, median, and mode grain radii; Equation 4.1 was analyzed using the mean, median, and mode grain radii to determine the impact on estimated permeability values.

The variance between numerically determined maximum and minimum standard deviation values was anticipated; the maximum standard deviation values depicted in Table 4.2 were truncated to mitigate representative volume element effects. Standard deviation values were estimated to vary between a maximum of 0.4650 millimeters and a minimum of 0.2325 millimeters using input parameters for numerical models. To examine the depicted standard deviation variances, grain radii histograms of representative porous media were analyzed; representative porous media are defined as numerical models exhibiting porosity values of approximately 0.40, 0.20, and 0.10 for estimated standard deviation values of 0.4650, 0.3488, and 0.2325 mm.

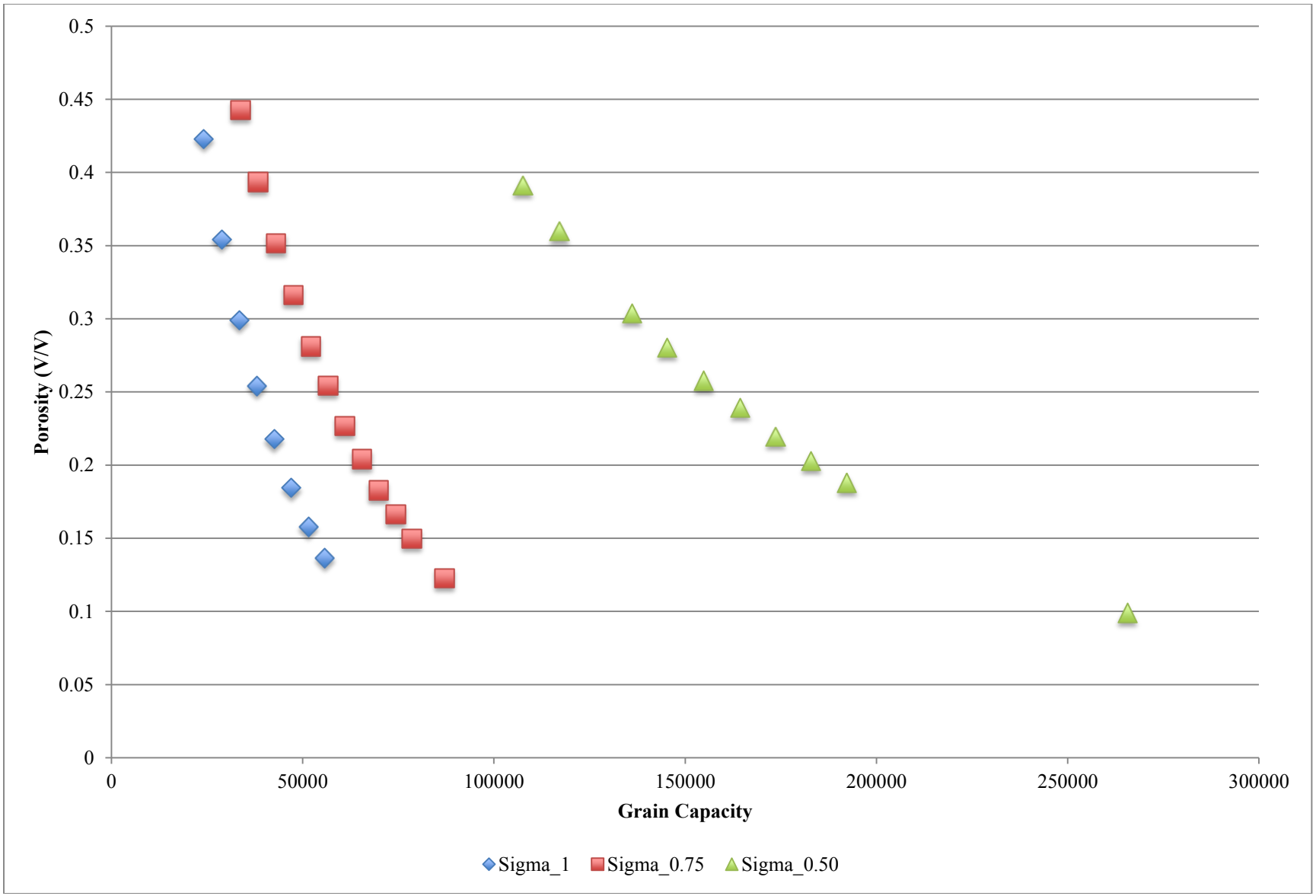

Figure 4.1: Grain capacity, porosity relationship for numerical model

Standard Deviation (mm)	Porosity (V/V)	Permeability-Mean (m^2)	Permeability-Median (m^2)	Permeability-Mode (m^2)
0.2267	0.3912	1.94E-14	7.56E-14	3.14E-15
0.2263	0.3598	1.46E-14	5.69E-14	2.37E-15
0.2258	0.3036	7.97E-15	3.11E-14	1.29E-15
0.2262	0.2805	6.09E-15	2.38E-14	9.87E-16
0.2256	0.2578	4.54E-15	1.77E-14	7.35E-16
0.2247	0.2393	3.81E-15	1.49E-14	6.17E-16
0.2242	0.2195	2.94E-15	1.15E-14	4.77E-16
0.2241	0.2029	2.11E-15	8.22E-15	3.41E-16
0.2230	0.1879	1.55E-15	6.06E-15	2.52E-16
0.2224	0.099	5.75E-19	2.24E-18	9.31E-20
0.3012	0.4427	2.68E-14	1.05E-13	4.35E-15

Table 4.2: Petrophysical and statistical parameters for numerical models

Standard Deviation (mm)	Porosity (V/V)	Permeability-Mean (m^2)	Permeability-Median (m^2)	Permeability-Mode (m^2)
0.3021	0.3935	1.75E-14	6.83E-14	2.84E-15
0.3019	0.3515	1.16E-14	4.53E-14	1.88E-15
0.2998	0.3161	8.69E-15	3.39E-14	1.41E-15
0.3007	0.2812	6.37E-15	2.48E-14	1.03E-15
0.3003	0.2543	4.37E-15	1.70E-14	7.08E-16
0.3020	0.2268	2.90E-15	1.13E-14	4.71E-16
0.2982	0.204	1.93E-15	7.52E-15	3.12E-16
0.2990	0.1827	1.44E-15	5.61E-15	2.33E-16
0.2959	0.1663	9.71E-16	3.79E-15	1.57E-16
0.2974	0.1497	7.53E-16	2.94E-15	1.22E-16
0.2945	0.1227	2.99E-16	1.17E-15	4.85E-17
0.3084	0.4229	2.22E-14	8.67E-14	3.60E-15
0.3083	0.3543	1.13E-14	4.42E-14	1.83E-15
0.3056	0.2990	6.45E-15	2.52E-14	1.05E-15
0.3071	0.2540	4.20E-15	1.64E-14	6.81E-16
0.3060	0.2178	2.36E-15	9.20E-15	3.82E-16
0.3053	0.1845	1.27E-15	4.95E-15	2.05E-16
0.3012	0.1579	6.68E-16	2.61E-15	1.08E-16
0.3018	0.1365	4.49E-16	1.75E-15	7.27E-17

Table 4.2: Petrophysical and statistical parameters for numerical models (cont.)

Figures 4.2 through Figure 4.10 depict grain radii histograms for numerical models exhibiting porosity values of 0.4229, 0.2178, 0.1365, 0.3935, 0.2040, 0.1227, 0.3912, 0.2029, and 0.0990, and estimated standard deviation values of 0.4650, 0.3485, and 0.2325 mm respectively.

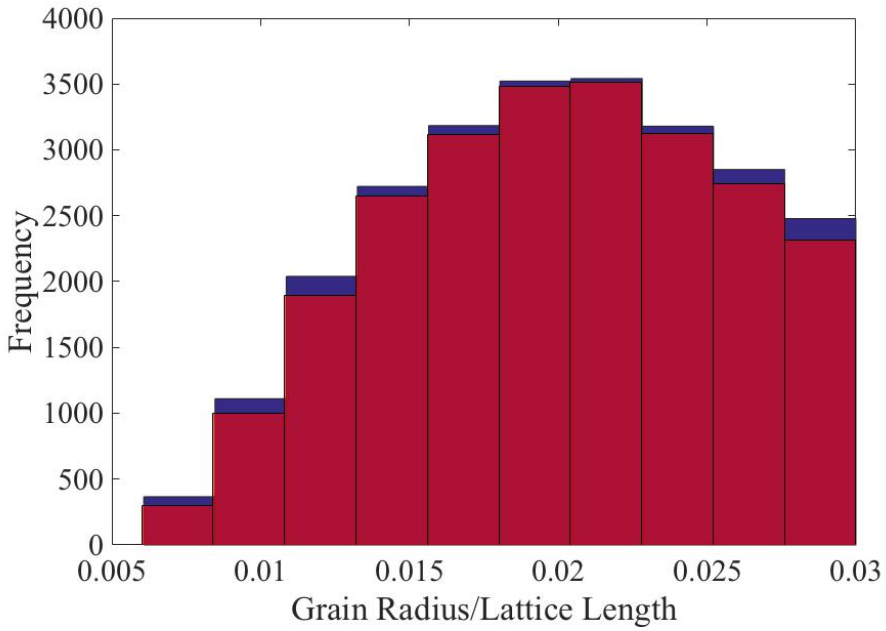

Figure 4.2: Initial (blue) and final (red) grain radius histograms for porous medium exhibiting standard deviation and porosity values of 0.4650 mm and 0.4229 respectively

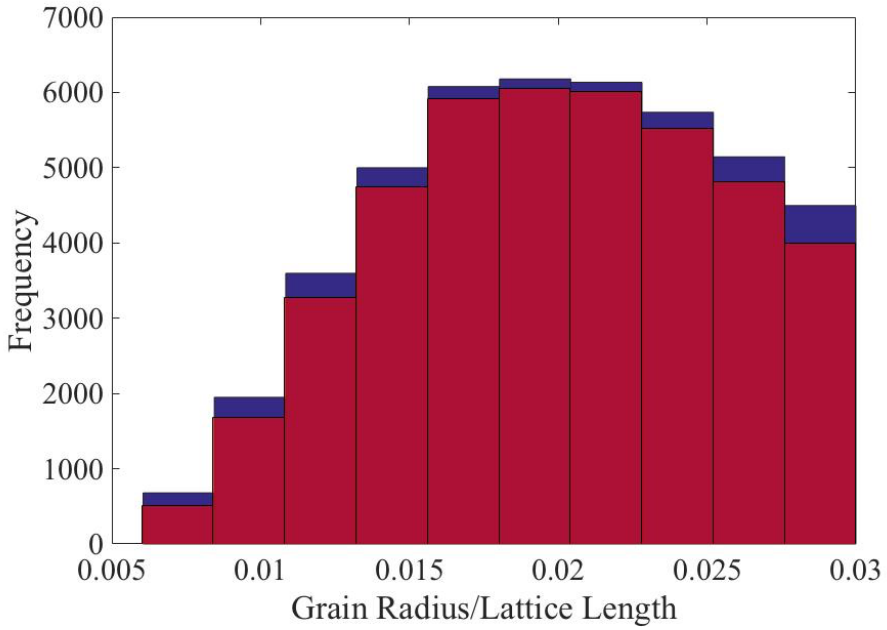

Figure 4.3: Initial (blue) and final (red) grain radius histograms for porous medium exhibiting standard deviation and porosity values of 0.4650 mm and 0.2178 respectively

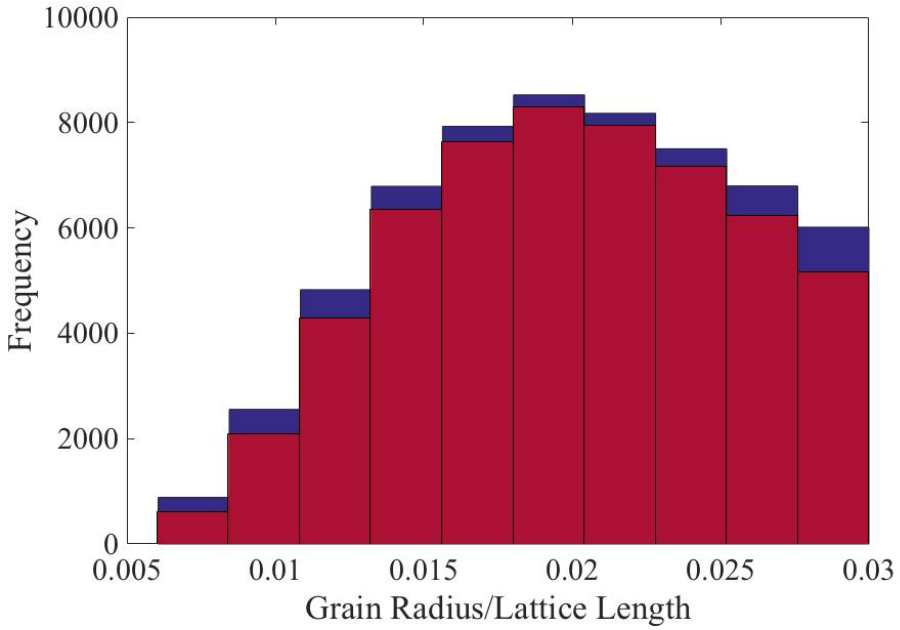

Figure 4.4: Initial (blue) and final (red) grain radius histograms for porous medium exhibiting standard deviation and porosity values of 0.4650 mm and 0.1365 respectively

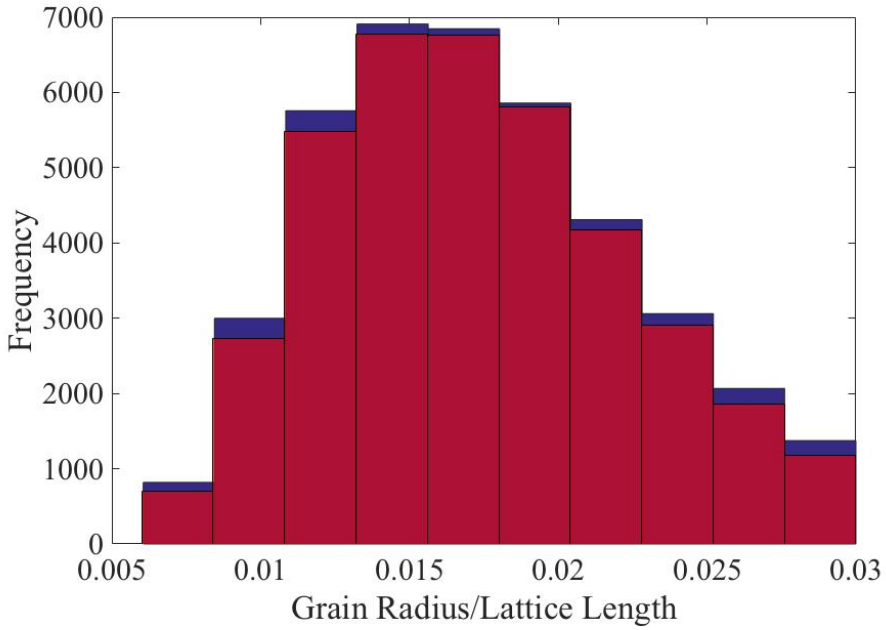

Figure 4.5: Initial (blue) and final (red) grain radius histograms for porous medium exhibiting standard deviation and porosity values of 0.3488 mm and 0.3935 respectively

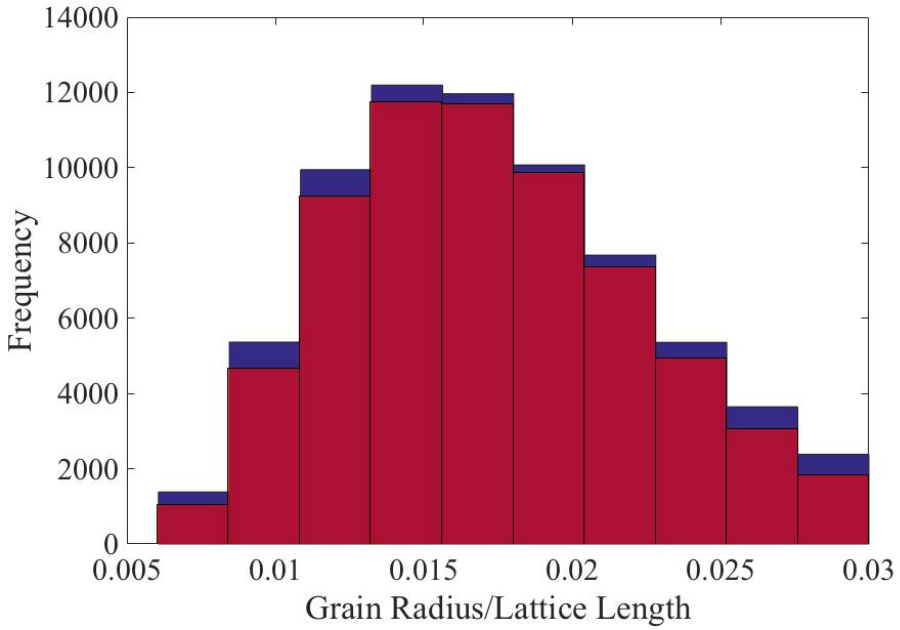

Figure 4.6: Initial (blue) and final (red) grain radius histograms for porous medium exhibiting standard deviation and porosity values of 0.3488 mm and 0.2040 respectively

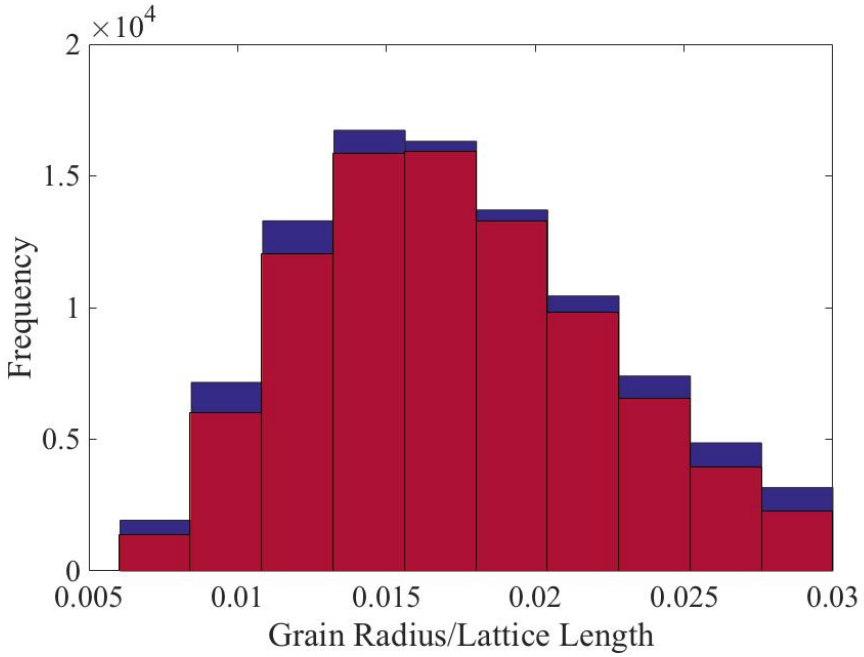

Figure 4.7: Initial (blue) and final (red) grain radius histograms for porous medium exhibiting standard deviation and porosity values of 0.3488 mm and 0.1227 respectively

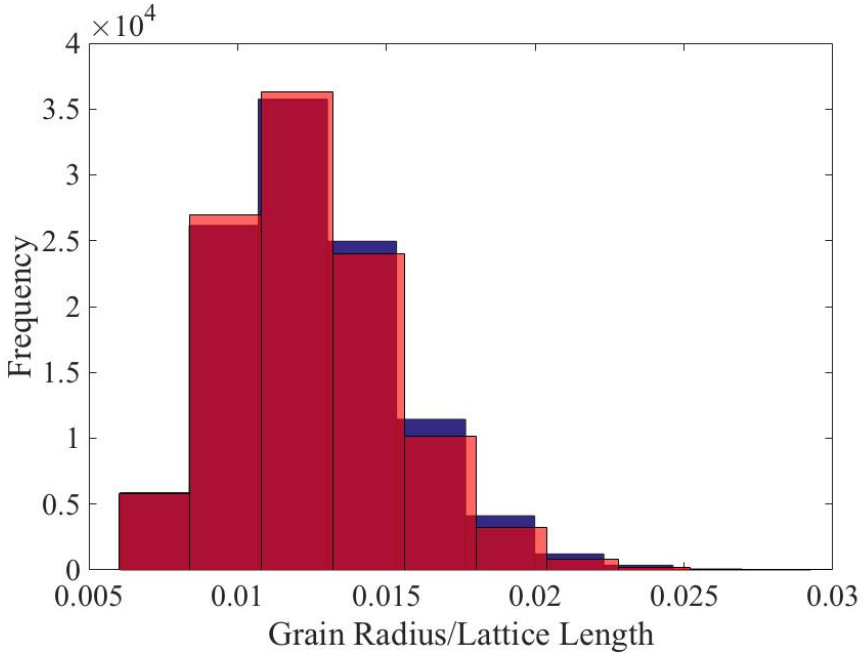

Figure 4.8: Initial (blue) and final (red) grain radius histograms for porous medium exhibiting standard deviation and porosity values of 0.2325 mm and 0.3912 respectively

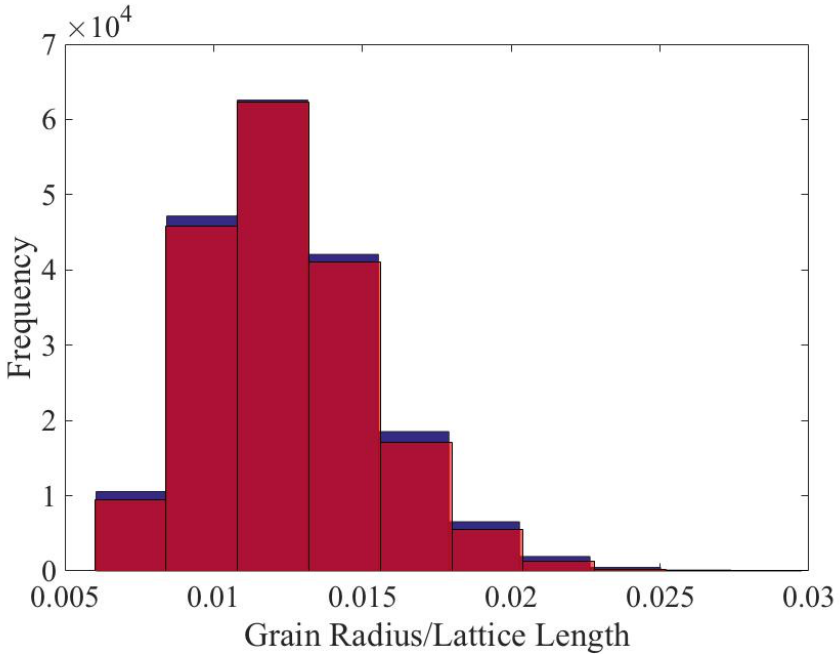

Figure 4.9: Initial (blue) and final (red) grain radius histograms for porous medium exhibiting standard deviation and porosity values of 0.2325 mm and 0.2029 respectively

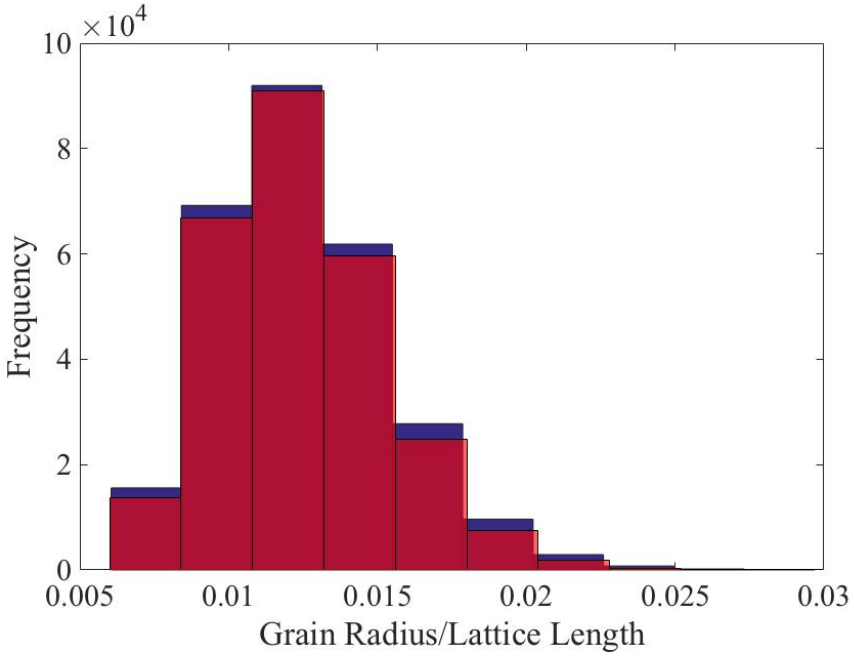

Figure 4.10: Initial (blue) and final (red) grain radius histograms for porous medium exhibiting standard deviation and porosity values of 0.2325 mm and 0.0990 respectively

The initial grain radii histogram represents the estimated grain capacity; the final grain radii histogram represents the grain capacity excluding completely imbricated spherical grains. Figures 4.2 through Figure 4.10 exhibit approximate skewness between initial and final radii histograms. The initial and final probability distributions for the numerical models were truncated at approximately 7 lattice units to mitigate representative element volume effects in the cubic lattice; however, grain radius truncation reduced the standard deviation of numerical models exhibiting estimated standard deviation values of 0.4650 and 0.3485 mm. The grain radius truncation did not influence the standard deviation of the numerical models exhibiting estimated standard deviation values of 0.2325 mm. The grain radius of the corresponding normal distribution positioned 3 standard deviations to the right of the mean was approximately 6 lattice units; as a result, minimal variance was exhibited between estimated and average standard deviation values for the numerical models exhibiting estimated standard deviation values 0f 0.2325. Because of grain radius truncation, the numerical models exhibited average standard deviations of 0.30547, 0.2994, and 0.2249 mm compared to the estimated standard deviations of 0.4650, 0.3485, and 0.2325 mm. Numerical models exhibited comparable initial and final mean grain radius values; numerical models exhibited average mean grain radii of 0.4854, 0.4200, and 0.3081 mm compared to estimated mean grain radii of 0.6199, 0.4374, and 0.3086 mm. The variance depicted between average and estimated standard deviation and mean grain radius values minimizes as the estimated standard deviation decreases; the results depicted are expected because decreases in estimated standard deviation values reduces the broadness of the grain size distribution and the estimated mean grain radius.

Approximate skewness depicted between initial and final grain radius histograms validate the method used to construct the numerical models. Despite estimated standard deviation values of 0.4650, 0.3488, and 0.2325 mm, the numerical models exhibited maximum and minimum standard deviation values of 0.3084 and 0.2227 mm

respectively. Grain radius truncation induced the variance between theoretical and actual standard deviation values. Figure 4.11 depicts the cumulative distribution functions of numerical models with theoretical standard deviation values of 0.4650, 0.3488, and 0.2325 mm.

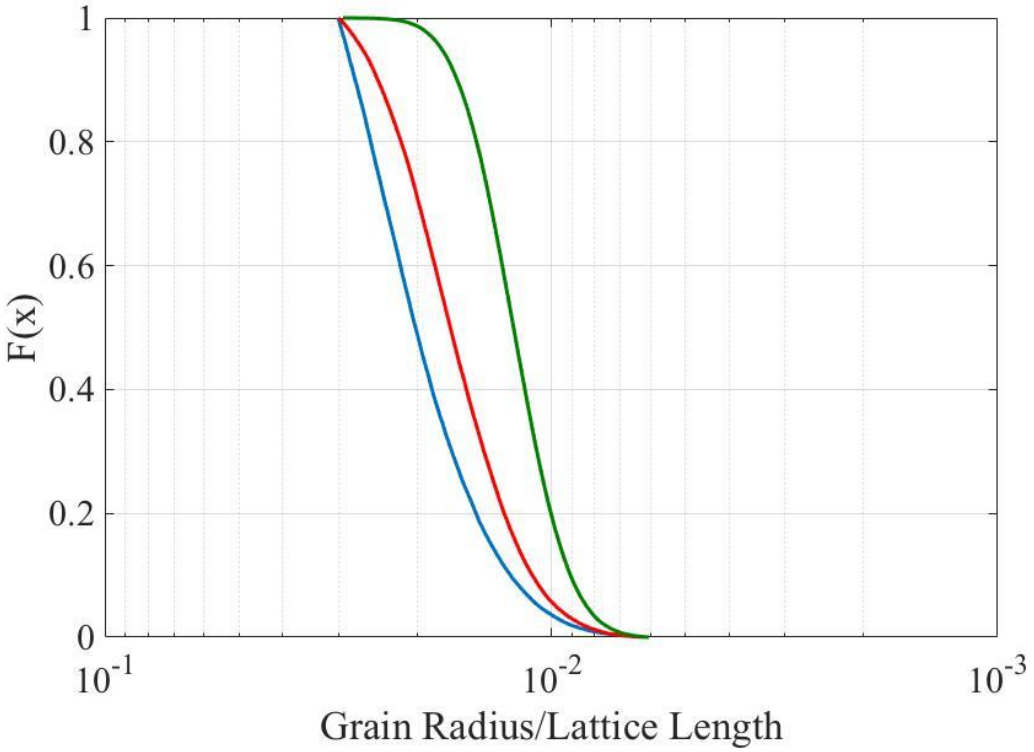

Figure 4.11: Cumulative distribution functions for representative porous media exhibiting porosity values of approximately 0.40 and estimated grain size standard deviation values of 0.4650 mm (blue), 0.3488 mm (red), and 0.2325 mm (green)

Figure 4.11 depicts representative cumulative distribution functions for the constructed numerical models exhibiting variable mean and standard deviation values. The Gulf of Alaska samples were used to represent porous media exhibiting broad grain size distributions. These samples were composed of variable combinations of clay, silt, and sand. Figure 4.12 depicts the cumulative grain size distribution for the Gulf of Alaska core samples. Figure 4.12 defines grain as sand, silt, or clay using grain size cutoffs:

clays are defined as particles with grain diameters below 0.002 millimeters, silts are defined as grain particles with grain diameters below and exceeding 0.0625 and 0.002 millimeters respectively, and sands are defined as grain particles with grain diameters exceeding 0.0625 millimeters. Table 4.3 depicts petrophysical and statistical properties for the analyzed core samples.

Core, section, Interval (cm)	Standard Deviation (mm)	Porosity (V/V)	Permeability (m^2)
341-U1420A-			
58R-1, 133-137.5	3.7	0.36	3.6E-17
65R-2, 134-138	3.5	0.37	7.8E-17
86R-1, 130-135	4.1	0.37	1.5E-17
92R-1, 129-133	2.3	0.41	1.2E-17
98R-2, 130-134.5	3.5	0.34	9.4E-17
106R-3, 47-52	3.2	0.33	2.0E-13
341-U1421A-			
62X-1, 130-135.5	4.0	0.41	4.5E-17
76X-1, 133-137	3.6	0.41	7.6E-15

Table 4.3: Data from consolidation and grain size measurements (Daigle and Piña, 2016)

The properties, porosity, standard deviation, mean diameter, and permeability, depicted in Table 4.2 exhibit minimum and maximum values of 0.33 to 0.41, 2.3 to 4.1 mm, 0.00232 to 0.0969 mm, and 1.2E-17 to 2.0E-13 m^2 respectively.

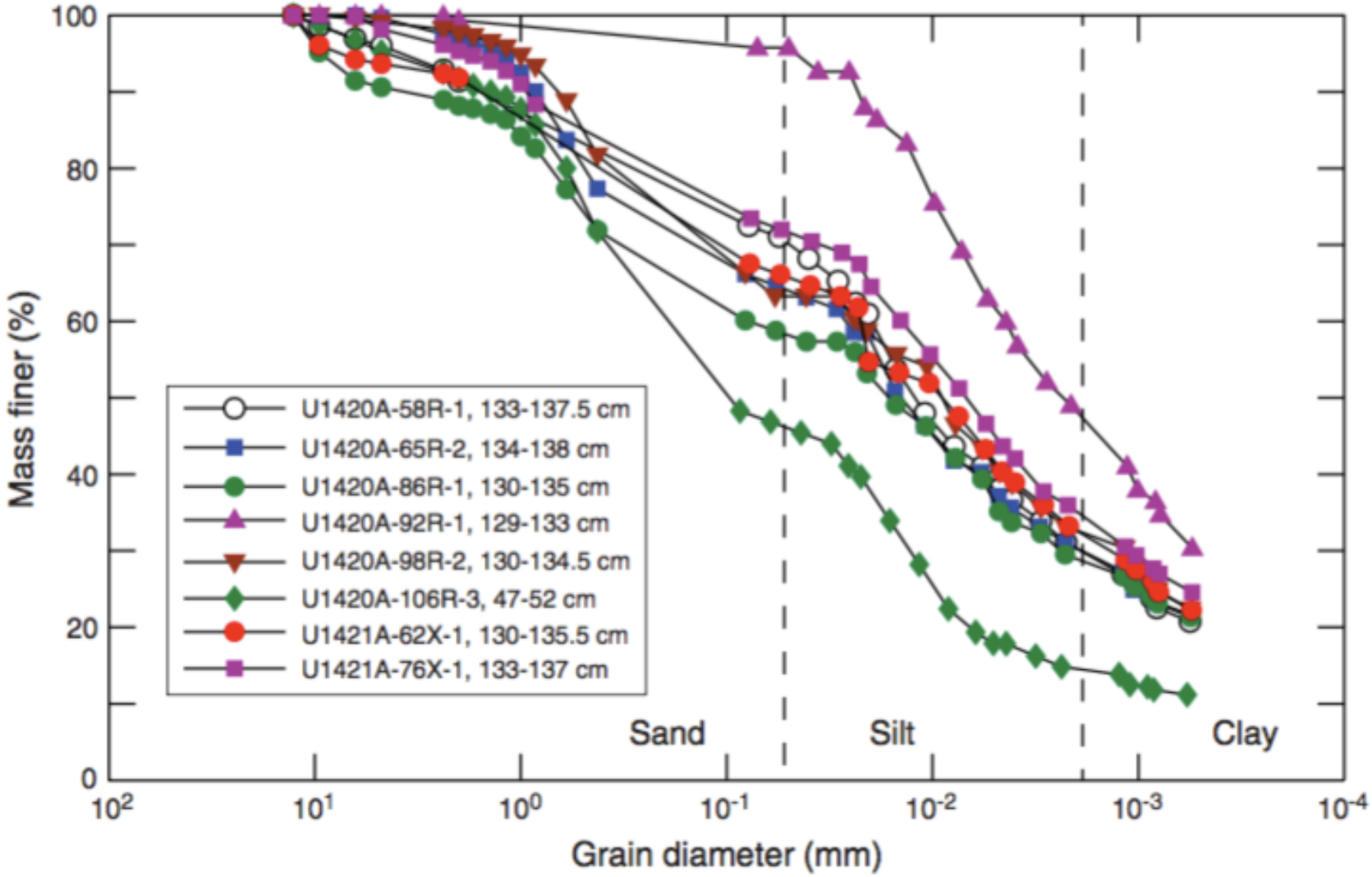

Figure 4.12: Cumulative grain size distribution for Gulf of Alaska core samples (Daigle and Piña, 2016)

4.2 ANALYSIS

Figures 4.13 through Figure 4.15 investigates the relationship between standard deviation and permeability for the numerical models and core experiments.

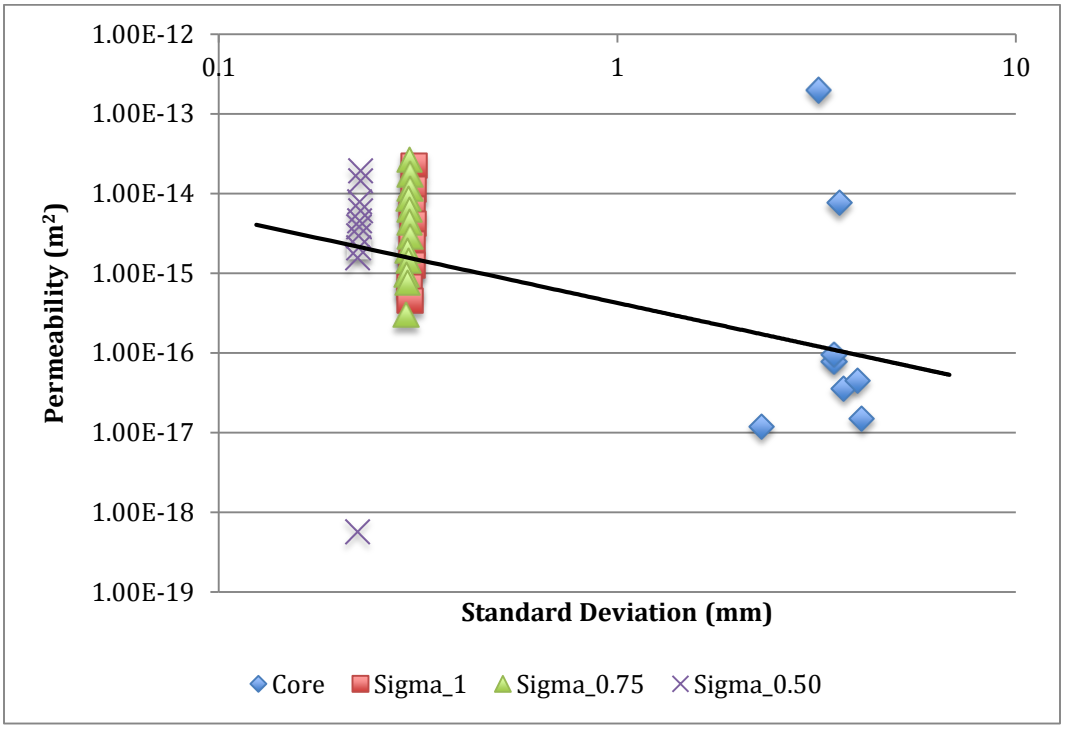

Figure 4.13: Standard deviation, permeability relationship using mean grain size diameter

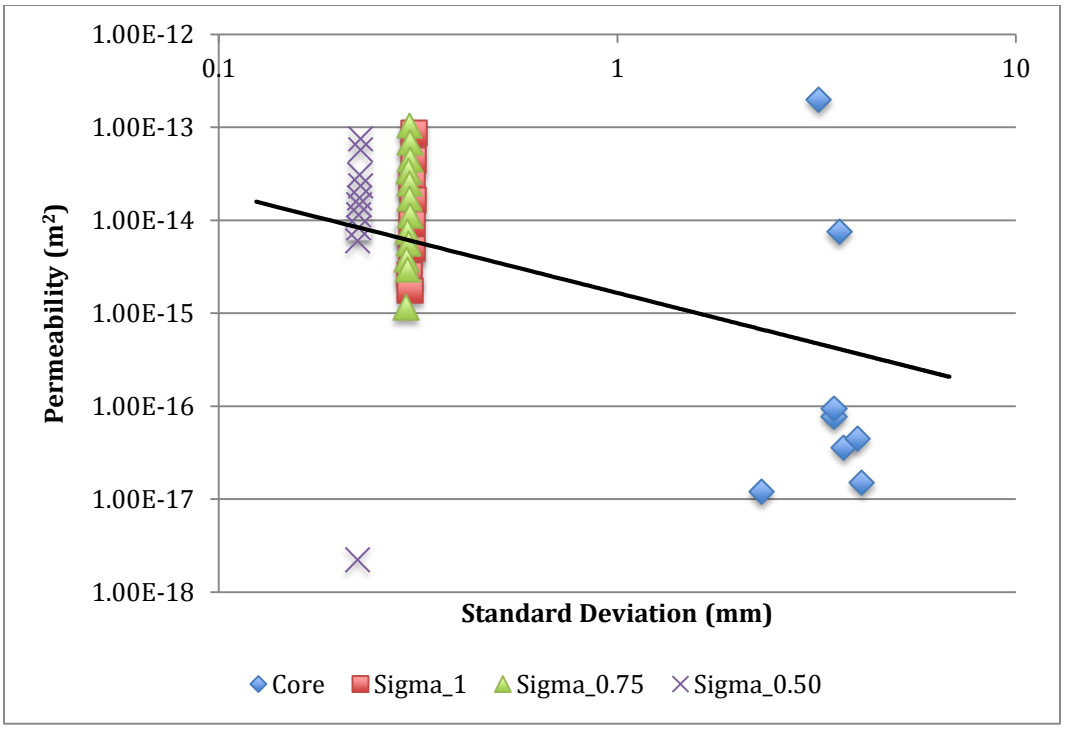

Figure 4.14: Standard deviation, permeability relationship using median grain size diameter

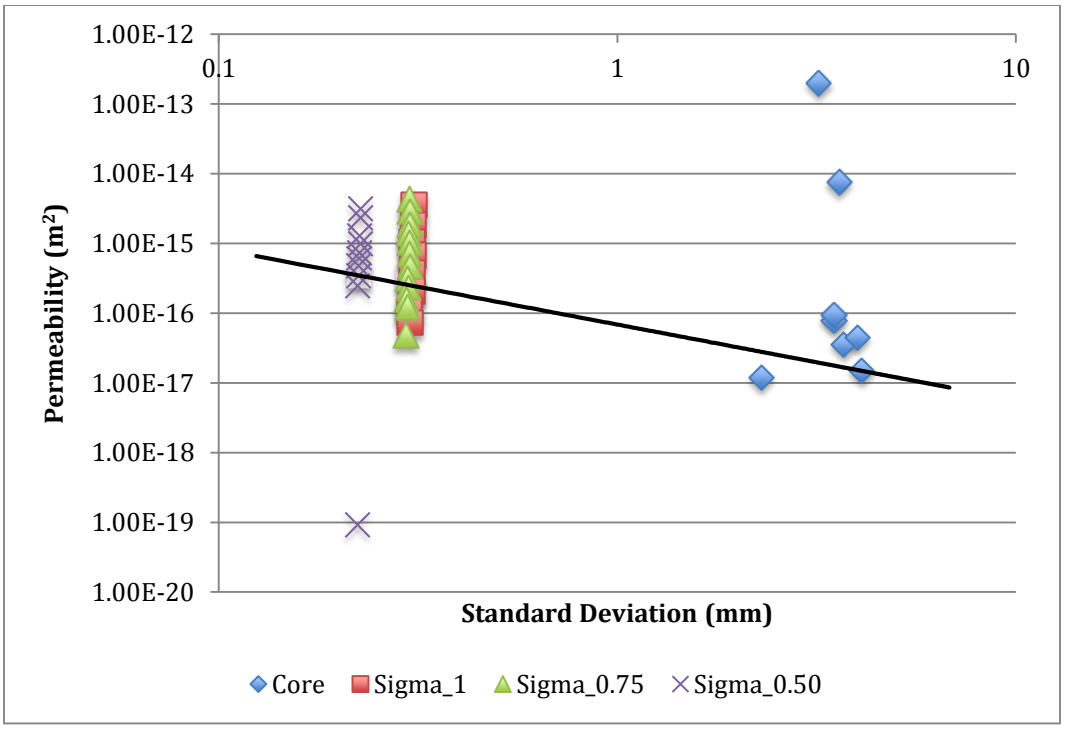

Figure 4.15: Standard deviation, permeability relationship using mode grain size diameter

Permeability estimates of the numerical models were determined using Equation 4.1; the permeability value depicted in Equation 4.1 was determined using the mean, median, and mode characteristic grain sizes. Multiple characteristic grain sizes were used to determine the effect of the mean, median, and mode characteristic grain size on permeability estimates and standard deviation, permeability relationships. The use of mean, median, and mode characteristic grain sizes modified the magnitude of permeability estimates. The standard deviation, permeability relationship remained constant irrespective of the characteristic grain size used for the numerical models; however, the slope of the trend between porous media exhibiting narrow and broad grain size distributions varied. The numerical models used to demonstrate porous media exhibiting narrow grain size distributions depicted in Figures 4.13 through Figure 4.15 exhibit a power law relationship between standard deviation and permeability values; however, Figures 4.13 through Figure 4.15 do not exhibit a conclusive correlation between narrow and broad grain size distributions. Inconclusive correlation is depicted between narrow and broad grain size distributions because of sparse core samples exhibiting broad grain size distributions; the standard deviations of the numerical and physical porous media exhibit maximum and minimum standard deviation values of 4.1 mm and 0.2227 mm respectively. The numerical models exhibit variable permeability values for specified standard deviation values. The permeability variance exhibited in Figures 4.13 through Figure 4.15 is the result of variable porosity values for the numerical and physical models; the numerical and physical models exhibit minimum and maximum porosity values of 0.10 and 0.40 respectively. The analysis concurs and extends the work of previous authors (Sprunt et al., 1970) depicting a power law relationship between permeability and grain size standard deviation. Previous authors determined a power law relationship between permeability and grain size standard deviation for minimum and maximum standard deviation values of 10 and 100 microns respectively; however, the

examined numerical models exhibit a minimum and maximum standard deviation values of 200 and 310 microns respectively.

Figures 4.16 through Figure 4.18 investigates the relationship between porosity and permeability for the numerical models and core experiments.

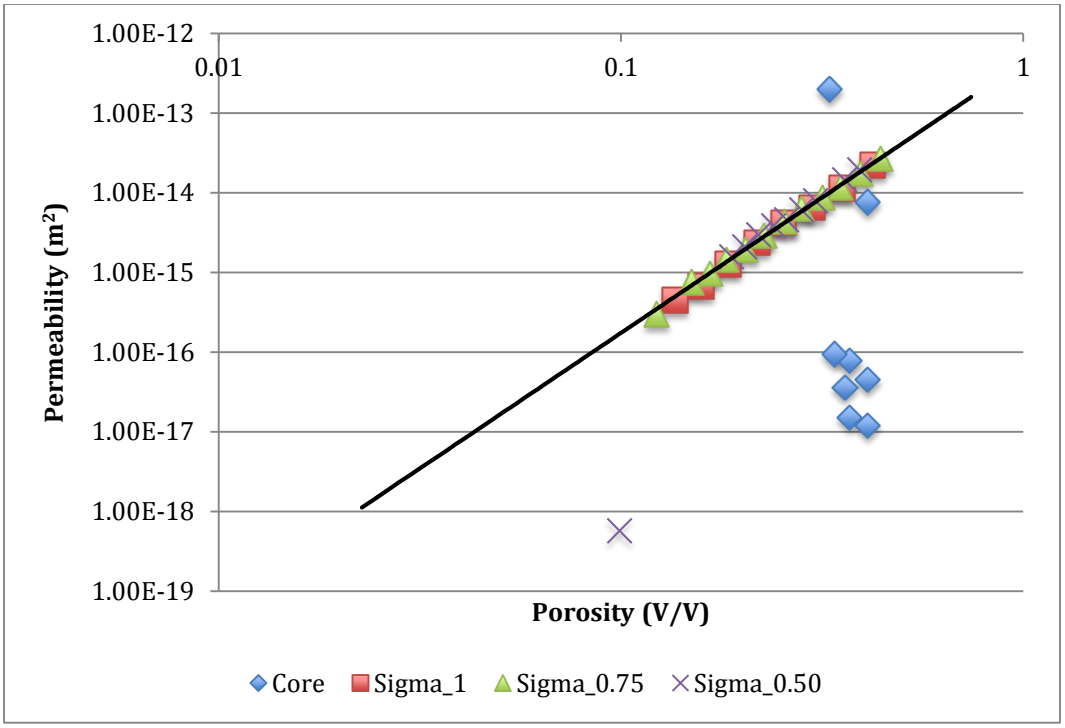

Figure 4.16: Porosity, permeability relationship using mean grain size diameter

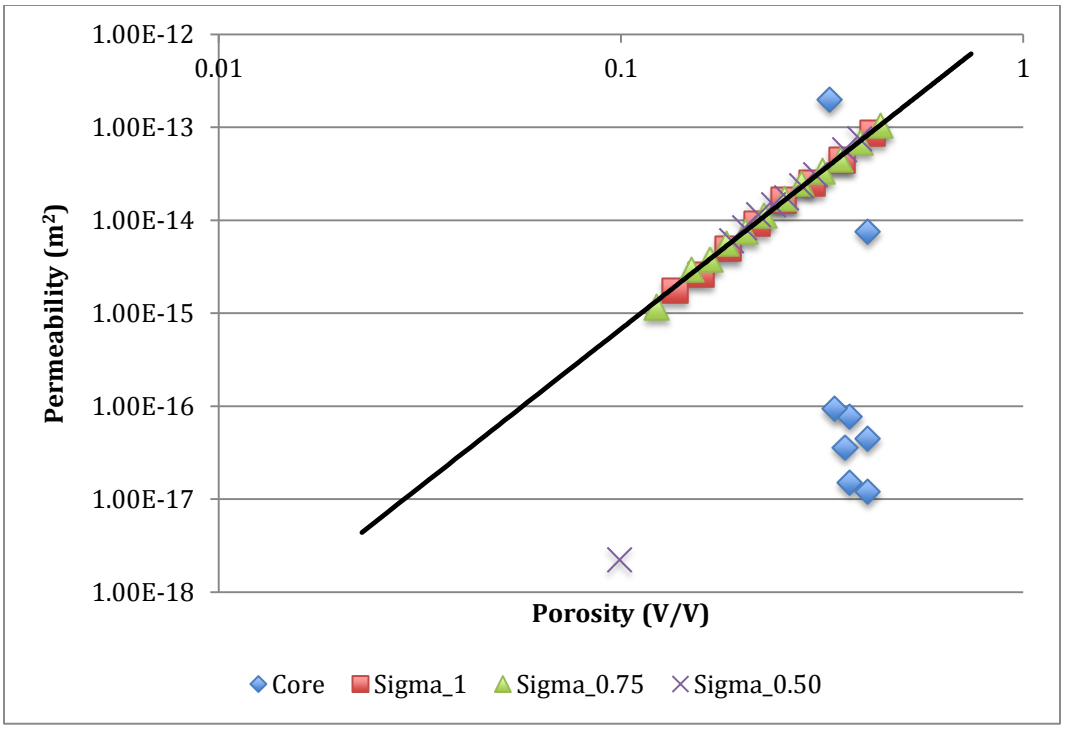

Figure 4.17: Porosity, permeability relationship using median grain size diameter

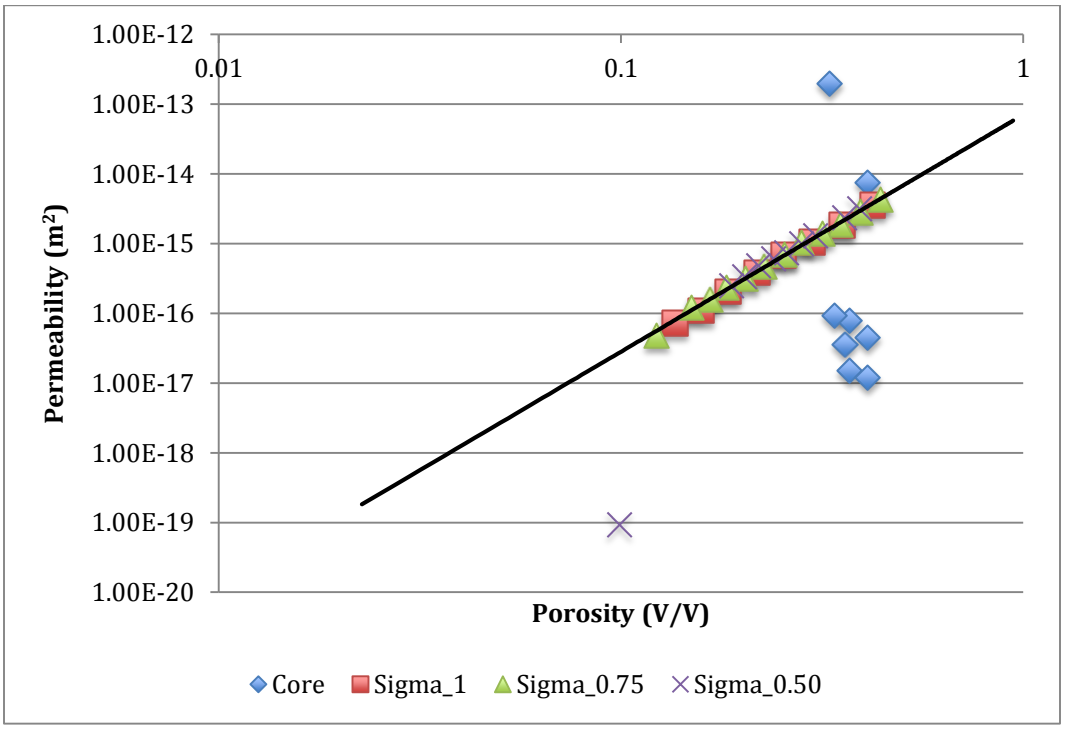

Figure 4.18: Porosity, permeability relationship using mode grain size diameter

Analogous to Figures 4.13 through Figure 4.15, Equation 4.1 and characteristic grain sizes, mean, median, and mode, were used to determine permeability estimates. The porosity, permeability relationships were comparable irrespective of the characteristic grain size used for the numerical models exhibiting narrow grain size distributions; however, the relationship between narrow and broad grain size distributions varied. The numerical and physical models used to demonstrate porous media exhibiting narrow and broad grain size distributions depicted in Figures 4.16 and Figure 4.17 using the mean and median characteristic grain radius did not exhibit a good correlation between narrow and broad grain size distributions; however, Figure 4.18 using the mode characteristic grain radius exhibited a moderate correlation between narrow and broad grain size distributions. Figure 4.18 exhibits a power law porosity, permeability relationship; the physical models exhibit scatter around the numerically constructed porous media. The depicted power law porosity, permeability relationship was unexpected; previous authors (Collins and Jordan, 1961) determined that porosity, permeability relationships exhibit power law trends in permeability compilations. The porosity, permeability relationship depicted in Figure 4.18 exhibits a single power law relationship for multiple permeability magnitudes. The power law trend depicted in Figure 4.18 exhibits minimum and maximum permeability values of 9.31E-20 and 2.0E-13 m^2 respectively. Irrespective of narrow or broad grain size distributions, the depicted power law relationship is governed by permeability magnitudes. The numerical model exhibiting porosity and permeability values of 0.0990 and 9.31E-20 m^2 was excluded from the porosity, permeability relationship depicted in Figure 4.18; the numerical model was excluded because the model approaches the percolation threshold of the constructed numerical models. The results determined that porosity, permeability relationships can be modeled irrespective of grain sorting; permeability, porosity relationships are influenced primarily by permeability magnitudes. Numerical and physical porous media determined that porosity, permeability relationships can exhibit moderate correlation spanning five orders of

permeability magnitudes; the percolation threshold is approached as the permeability magnitude increases.

Numerical and physical models demonstrating narrow and broad grain size distributions exhibited a power law porosity, permeability relationship irrespective of grain size sorting. Numerical models exhibiting narrow grain size distributions demonstrate larger permeability values than numerical models exhibiting broader grain size distributions. The permeability results were expected because narrow grain size distributions represent well-sorted rock, while broad grain size distributions represent poorly sorted rocks.

4.3 PERMEABILITY MODELS

Lattice Boltzmann permeability estimates were compared to permeability estimates derived from the Kozeny-Carman (Carman, 1956) model depicted in Equation 2.9; the Kozeny-Carman permeability estimates assumed distinctive Kozeny-Carman constants for the numerical models exhibiting estimated grain size standard deviations of 0.4650 mm, 0.3488 mm, and 0.2325 mm.

$$k = \frac{\Phi^3}{k_0(1-\Phi)^2 S^2}, \tag{2.9}$$

where k represents permeability, Φ represents total porosity, k_0 represents the Kozeny-Carman constant, S represents the specific surface area of particles exposed to the flowing fluid.

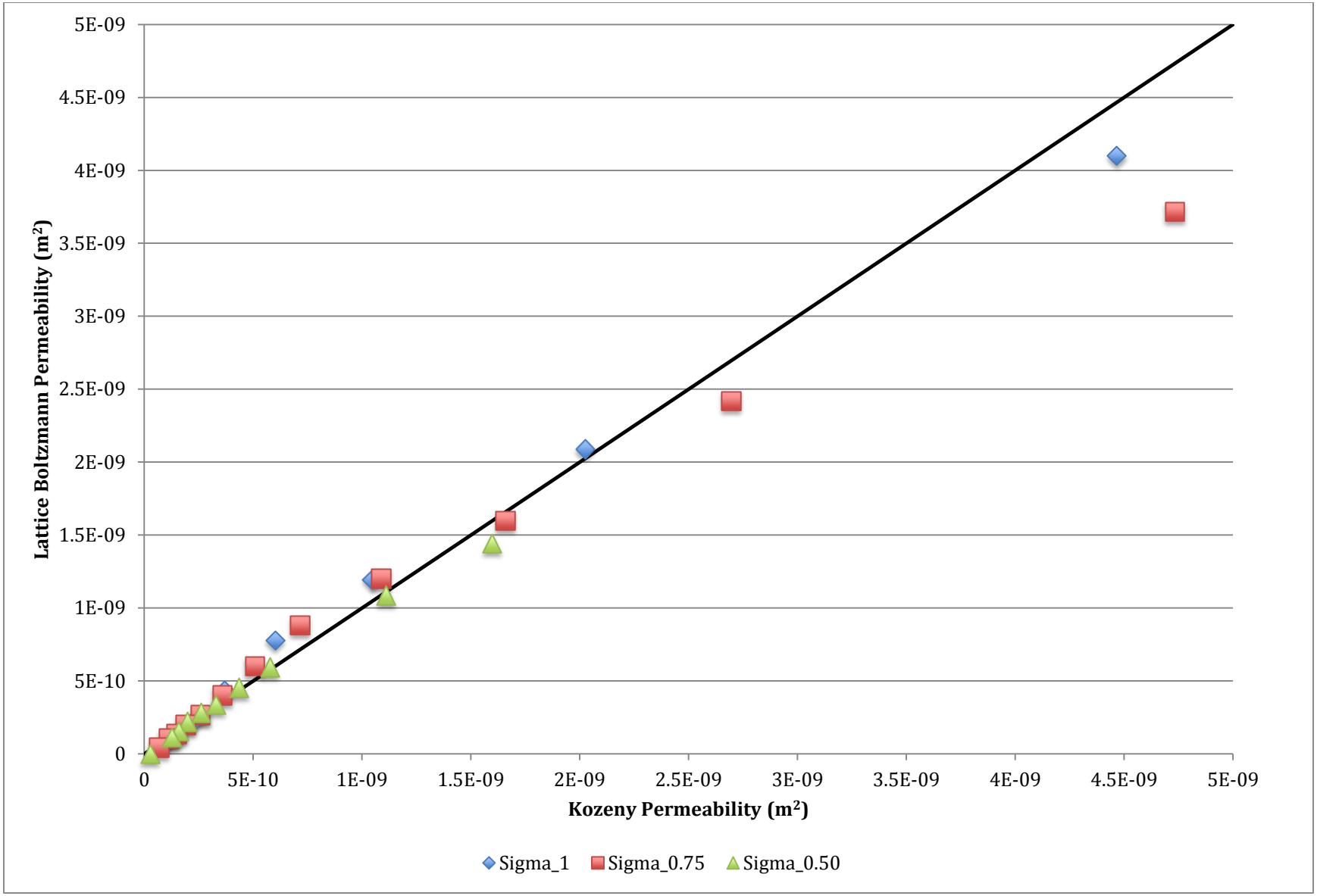

Figure 4.19: Comparison of Lattice Boltzmann and Kozeny-Carman permeability estimates

The specific surface area, S, is defined in Equation 4.2:

$$S = \sum_{i=1}^{248} P \left[\frac{L_p}{L_{LBM}}\right]^2, \tag{4.2}$$

where P represents the grain perimeter of two-dimensional image slices of the three-dimensional cubic lattice. Figure 4.19 depicts the comparison of Lattice Boltzmann and Kozeny-Carman permeability estimates.

Kozeny-Carman permeability estimates assume Kozeny-Carman constants of approximately 30.14, 28.57, and 25.24 for numerical models exhibiting estimated standard deviation values of 0.4650, 0.3488, and 0.2325 respectively. Lattice Boltzmann permeability estimates were determined using Equation 4.3:

$$k_p = k_n \left[\frac{L_p}{L_{LBM}}\right]^2, \tag{4.3}$$

Analyzing Figure 4.19, the numerical models exhibiting estimated standard deviation values of 0.4650, 0.34875, and 0.2325 mm, demonstrated good correlation between Lattice Boltzmann and Kozeny-Carman permeability estimates. The variance exhibited between the Lattice Boltzmann and Kozeny-Carman permeability estimates was expected because of the invariable Kozeny-Carman constants used in the Kozeny-Carman permeability model. The Kozeny-Carman permeability models assumed constant shape factor and tortuosity values; however, the numerical simulations exhibited variable shape factor and tortuosity values. The variable shape factor and tortuosity values demonstrated in the numerical simulations compared to the constant shape factor and tortuosity values used in the Kozeny-Carman permeability model produce the permeability variance depicted in Figure 4.19; nonetheless, strong correlation is exhibited between Lattice Boltzmann and Kozeny-Carman permeability estimates.

5. Conclusion

I analyzed the relationship between grain size, mean grain size, median grain size, and grain size mode; grain size standard deviation; and absolute permeability through the amalgamation of numerical modeling and experimental core data for sediments from the Pacific Ocean and Gulf of Alaska. The Pacific Ocean samples were selected to characterize porous media exhibiting narrow grain size distributions; the Gulf of Alaska samples were selected to characterize porous media exhibiting broad grain size distributions. The numerical models used to demonstrate porous media exhibiting narrow grain size distributions exhibited a power law relationship between standard deviation and permeability values; however, the analysis of standard deviation and permeability values did not exhibit a conclusive correlation between narrow and broad grain size distributions. The numerical and physical models used to demonstrate porous media exhibiting narrow and broad grain size distributions exhibited a power law porosity, permeability relationship using the characteristic mode grain radius. Irrespective of grain size distributions, the depicted power law porosity, permeability relationship was governed by permeability magnitudes. Standard deviation, permeability and porosity, permeability relationships were sensitive to the characteristic grain size, mean, median, and mode, used to determine permeability estimates.

5.1 Recommendations

The experimental design was modeled to analyze the relationships between absolute permeability, grain size, and grain size standard deviation for multiple rock models. Additional research developments are required to enhance investigations between grain size standard deviation and permeability: statistical distributions, grain orientation, variable grain architecture, multiphase and multicomponent flow, and numerical optimization techniques.

The numerically constructed porous media used a lognormal grain size distribution to populate the porous media with imbricated spherical grains; however, the grain size distributions of reservoirs are not restricted to lognormal distributions. Because of the complexity of petroleum reservoirs, multiple statistical distributions define different reservoir textures; beta, Birnbaum-Saunders, Burr Type XII, chi-square, exponential, extreme value, F, gamma, generalized extreme value, Gaussian mixture, generalized Pareto, inverse Gaussian, kernel, logistic, loglogistic, Nakagami, noncentral chi-square, noncentral F, noncentral t, normal, piecewise linear, Rayleigh, Rician, Student's t, t location-scale, triangular, and Weibull are statistical distributions to be implemented within the numerical models. The implemented statistical distributions will investigate the influence of statistical distributions on the relationship between permeability and grain size standard deviation. The influence of statistical distributions on transport properties investigates the impact of different reservoir textures.

Grain architecture is an additional textural property influencing secondary porous media properties. The numerically constructed porous media inferred spherical grains permeated throughout the porous media. Spherical grain architecture is a simplistic grain architecture used by multiple permeability models such as the Hazen and Kozeny-Carman permeability models; nonetheless, reservoir grain architecture is variable. Reservoir grain architecture is dependent of the constituents of the grain particles; as a result, sands, silts, and clays exhibit different grain architectures. To effectively construct numerical models of porous media, different grain architectures are required: cylinders, cubes, oblate ellipsoids, prolate ellipsoids, pyramids, spheres, and triangular prisms. Variable grain architectures enable the construction of very well sorted, well sorted, moderately sorted, poorly sorted, very poorly sorted, and laminated porous media. Variable grain architectures augment the defined texture of numerical porous media simulations; as a result, enhanced transport property estimates are determined.

Grain orientation is an additional textural property influencing secondary porous media properties. The used numerical simulation approximated imbricated spherical grain particles; as a result, grain orientation was inconsequential to the constructed porous media models. The implementation of variable grain architecture requires the application of grain orientation; the imbrication orientation of cylinder, cube, oblate ellipsoid, prolate ellipsoid, pyramid, sphere, and triangular prism grain particles influence estimated transport properties. Reservoir rocks exhibit a magnitude of grain architectures and orientations because of sorting and digenetic processes; as a result, the implementation of grain orientation enhances the precision of the numerical models and the estimate of secondary reservoir properties. Grain orientation augmented with grain architecture enables the investigation of relationship between fluid density, grain orientation, and grain architecture.

The investigation of the relationship between fluid density, grain orientation, and grain architecture enables the examination of multicomponent and multiphase transport phenomena. Shan and Chen (1993) developed Lattice Boltzmann algorithms to determine transport properties for immiscible multicomponent fluids and single component multiphase fluids. The implementation of multicomponent and multiphase flow profiles is fundamental to characterizing reservoir transport phenomena. Reservoirs exhibit multicomponent and multiphase flow profiles throughout primary, secondary, and tertiary recovery mechanisms; the multicomponent and multiphase Lattice Boltzmann algorithms facilitates the numerical investigation of oil reservoirs, wet gas reservoirs, depleted reservoirs, water flooding breakthrough, and enhanced oil recovery techniques. Oil reservoirs, wet gas reservoirs, water flood breakthrough, and enhanced oil recovery techniques exhibit multi-component transport phenomena; depleted reservoirs exhibit multiphase transport phenomena. The multicomponent and multiphase Lattice Boltzmann algorithms enable the estimate of relative permeability for petroleum reservoirs.

To effectively implement variable grain architecture, numerical optimization techniques are required. Numerical optimization techniques enable the utilization of additional lattice units; additional lattice units are required to replicate variable grain architectures. Furthermore, increased lattice units enable the minimization of the numerical simulations' aspect ratio between minimum grain size and lattice length. Examining laboratory core data, the aspect ratio between the minimum grain radius and the core length is approximately 0.000018; however, the aspect ratio of the numerical model is approximately 0.012. The degree of difference between the laboratory core and the numerical simulations were 3 orders of magnitude; the minimization of the difference between laboratory core and numerical simulation aspect ratios enhances reservoir characterization. Enhanced reservoir characterization enables improved estimates of primary and secondary reservoir properties: grain architecture, grain orientation, sorting, and transport properties.

6. Appendix

Diameter (mm)	Mass Finer (%)
0.07217	105.2
0.05103	105.2
0.03670	101.1
0.02603	100.3
0.02133	99.5
0.01847	99.5
0.01310	98.7
0.00929	97.9
0.00661	96.3
0.00489	93.0
0.00404	89.8
0.00355	86.6
0.00266	70.4
0.00217	36.4
0.00127	12.1
0.00111	8.9
0.00091	8.9

Table 6.1: Grain size distribution for mudstone core exhibiting a narrow grain size distribution

Porosity (V/V)	Standard Deviation (LU)	Grain Radius (%)	Permeability (LU^2)		
			x-direction	y-direction	z-direction
0.3916	0.4271	---	5.73E-01	5.96E-01	5.84E-01
0.4244	0.3969	0.050	6.75E-01	6.67E-01	7.14E-01
0.4156	0.3804	0.045	5.86E-01	5.63E-01	5.78E-01
0.4160	0.3609	0.040	5.05E-01	5.18E-01	5.00E-01
0.4270	0.3313	0.035	4.85E-01	4.69E-01	4.86E-01
0.3941	0.3009	0.030	2.90E-01	2.95E-01	2.84E-01
0.1961	0.4056	---	4.89E-02	4.75E-02	4.97E-02
0.2132	0.3851	0.050	5.45E-02	5.96E-02	5.75E-02
0.2100	0.3731	0.045	5.92E-02	5.46E-02	6.02E-02
0.2286	0.3568	0.040	6.78E-02	5.89E-02	6.78E-02
0.1975	0.3170	0.035	3.60E-02	3.39E-02	3.70E-02
0.2228	0.2946	0.030	4.65E-02	4.54E-02	4.54E-02
0.1034	0.4027	---	4.47E-03	5.12E-03	4.54E-03
0.1147	0.3795	0.050	6.78E-03	6.78E-03	6.78E-03
0.1189	0.3678	0.045	7.17E-03	6.29E-03	8.16E-03
0.1314	0.3497	0.040	9.64E-03	9.15E-03	9.99E-03
0.1292	0.3062	0.035	7.83E-03	7.57E-03	8.25E-03
0.1224	0.2851	0.030	5.54E-03	5.58E-03	5.57E-03

Table 6.2: Maximum permitted grain radius as a percent of lattice length for porous media exhibiting an estimated standard deviation of 0.4650

Porosity (V/V)	Standard Deviation (LU)	Grain Radius (%)	Permeability (LU^2)		
			x-direction	y-direction	z-direction
0.3986	0.3145	---	2.77E-01	2.66E-01	2.73E-01
0.3977	0.3124	0.05	2.64E-01	2.65E-01	2.68E-01
0.3814	0.3302	0.045	2.44E-01	2.42E-01	2.36E-01
0.3943	0.3230	0.04	2.66E-01	2.59E-01	2.57E-01
0.4076	0.3161	0.035	2.86E-01	2.83E-01	2.82E-01
0.394	0.3031	0.03	2.24E-01	2.31E-01	2.30E-01
0.2104	0.3210	---	3.16E-02	3.23E-02	3.42E-01
0.2153	0.3221	0.05	3.70E-02	3.59E-02	3.56E-02
0.2007	0.3224	0.045	2.76E-02	2.85E-02	2.90E-02
0.2055	0.3202	0.04	2.93E-02	2.97E-02	3.00E-02
0.2155	0.3125	0.035	3.60E-02	3.39E-02	3.67E-02
0.2036	0.2993	0.03	2.59E-02	2.56E-02	2.72E-02
0.1103	0.3163	---	3.10E-03	2.93E-03	3.13E-03
0.1234	0.3167	0.05	5.92E-03	4.52E-03	4.49E-03
0.1112	0.3147	0.045	2.79E-03	3.70E-03	3.10E-03
0.1083	0.3134	0.04	3.39E-03	2.90E-03	2.66E-03
0.1143	0.3088	0.035	2.94E-03	3.88E-03	3.82E-03
0.1227	0.2945	0.03	4.62E-03	3.95E-03	4.72E-03

Table 6.3: Maximum permitted grain radius as a percent of lattice length for porous media exhibiting an estimated standard deviation of 0.3488

Porosity (V/V)	Standard Deviation (LU)	Grain Radius (%)	Permeability (LU^2)		
			x-direction	y-direction	z-direction
0.4297	0.2275	0.04	1.79E-01	1.78E-01	1.78E-01
0.4244	0.2276	0.035	1.70E-01	1.70E-01	1.71E-01
0.4233	0.2279	0.03	1.69E-01	1.71E-01	1.70E-01
0.1958	0.2243	0.04	1.41E-02	1.15E-02	1.44E-02
0.1949	0.2240	0.035	1.24E-02	1.38E-02	1.10E-02
0.1935	0.2245	0.03	1.36E-02	1.33E-02	1.23E-02
0.0946	0.2221	0.04	1.74E-03	1.72E-03	1.51E-03
0.0963	0.2215	0.035	1.52E-03	1.61E-03	1.63E-03
0.0990	0.2224	0.03	3.82E-06	4.07E-06	3.88E-06

Table 6.4: Maximum permitted grain radius as a percent of lattice length for porous media exhibiting an estimated standard deviation of 0.2325

```
%The Porous_Medium simulation creates a porous medium with overlaping
%and point contact spherical grains. The spherical grains within the
%simulation is of a random size and placement distribution.

clc
clear all

diary on

e = [285000];

for xx = 1:size(e,1);
%% Latice Construction

%Comments enclosed by %'s represent simulation variables
%cx, cy, and cz represent the dimensions of the cubic lattice%
cx = 1;
cy = 1;
cz = 1;

%Vertex points for lattice defined by cx, cy, and cz
x = [0 cx cx 0 0 0; cx cx 0 0 cx cx; cx cx 0 0 cx cx; 0 cx cx 0 0 0];
y = [0 0 cy cy 0 0; 0 cy cy 0 0 0; 0 cy cy 0 cy cy; 0 0 cy cy cy cy];
z = [0 0 0 0 0 cz; 0 0 0 0 0 cz; cz cz cz cz 0 cz; cz cz cz cz 0 cz];
%% Porous Medium Construction

%Lognormal distribution

mu = log(3/248/2) + 0.4650*0.5*3;
%The mu (geometric mean) value was obtained from curve fitting
experimental
%data of a physical rock sample; the results are depicted in
%Grain_Size_Analysis_Lognormal m-file. Log of 0.0125
%was added to the normalized mu to truncate the lognormal distribution
%within the tessellation constraints. The quantity 0.0121 represents
%3*Rp; Rp is the pixel diameter. The pixel diameter is defined in the
%m-file as 1/voxel. The quantity of 0.4650*3 was added to log(0.0125)
to
%determine the shifted mean of the lognormal distribution.

sig = 0.4650*0.5;
%The sig (standard deviation) value was obtained from curve fitting
%experimental data of a physical rock sample, the results are depicted
in
%Grain_Size_Analysis_Lognormal m-file.

%Normal distribution

%mu = 0.0125 + 0.0090*3;
%The mu (geometric mean) value was obtained from cruve fitting
experimental
%t-curve data of a physical rock sample; the results are depicted in
%Grain_Size_Analysis_Normal m-file. The constant 0.0125 was added to
the
%normalized mu to truncate the normal distribution within the
```

```
tessellation
%constraints. The quantity 0.0121 represents 3*Rp; Rp is the pixel
%diameter. The pixel diameter is defined in the m-file as 1/voxel. The
%quantity of 0.0090*3 was added to 0.0125 to determine the shifted mean
of
%the normal distribution.

%sig = 0.0090;
%The sig (standard deviation) value was obtained from curve fitting
%experimental data of a physical rock sample, the results are depicted
in
%Grain_Size_Analysis_Normal m-file.

%Estimated total quantiy of grains within the porous medium
g = e(xx);
disp(['grains_initial = ' num2str(g)]);

%Radius matrix for the porous medium
radius = lognrnd(mu,sig,g,1);
%radius = normrnd(mu,sig,g,1);

%Upper and lower truncation of radius values
r = 1;

while r < (g+1);
    if radius(r,1) > (cx*.030) || radius(r,1) < (3/248/2);
    radius(r,1) = lognrnd(mu,sig);

    else
        r = r + 1;
    end
end

figure(1);
hist(radius);
%% Boundary Conditions

%Line 79 through line 95 determines if spherical grains exceed lattice
%boundaries, if grain exceeds lattice boundaries, new coordinates are
%generated within the cubic lattice. If line 79 through line 95 are
%commented out of the simulation, but line 71 is commented in the
%simulation, spherical grains are allowed to imbriate the lattice
boundary;
%however, the centroid of spherical grains are restircted to the
%constraints of the lattice boundary. If line 72 is commented out of
the
%simulation and Line 77 through Line 79 is commented in the simulation,
%the centroid of spherical grians are allowed to generated external to
the
%lattice boundary.

%Coordinate matrix for spherical grains
%c = unifrnd(0,cx,[g,3]);

c = zeros(g,3);
```

```
for ii = 1:g
    c(ii,:) = unifrnd((0 - radius(ii)), (cx + radius(ii)), [1,3]);
end

%Lattice constrained spherical grains
%for r = 1:g;
%    bou_x = [(cx - radius(r)), (cx - (cx - radius(r)))];
%    if radius(r) + c(r,1) > cx | c(r,1) - radius(r) < 0;
%        c(r,1) = unifrnd(min(bou_x), max(bou_x));
%    end

%    bou_y = [(cy - radius(r)), (cy - (cy - radius(r)))];
%    if radius(r) + c(r,2) > cy | c(r,2) - radius(r) < 0;
%        c(r,2) = unifrnd(min(bou_y), max(bou_y));
%    end

%    bou_z = [(cz - radius(r)), (cz - (cz - radius(r)))];
%    if radius(r) + c(r,3) > cz | c(r,3) - radius(r) < 0;
%        c(r,3) = unifrnd(min(bou_z), max(bou_z));
%    end

%end

%Determines if spherical grains are encapsulated; encapsulated
spherical
%grains are deleted.
a = 1;
%boundary = ones(g,1);

% parfor yy = 1:g
%     G = sqrt((c(yy,1)-c(:,1)).^2 + (c(yy,2)-c(:,2)).^2 + ...
%         (c(yy,3)-c(:,3)).^2) > abs((radius(yy,1)-radius(:,1))) | ...
%         sqrt((c(yy,1)-c(:,1)).^2 + (c(yy,2)-c(:,2)).^2 + ...
%         (c(yy,3)-c(:,3)).^2) == 0 & abs((radius(yy,1)-radius(:,1)))
== 0;
%
%     boundary = boundary.*G;
% end
%
% radius = radius .* boundary;
% [f,~] = find(radius == 0);
% radius(f,:) = [];
% c(f,:) = [];
% g = size(radius,1);

while a < (g+1)
    G = sqrt((c(a,1)-c(:,1)).^2 + (c(a,2)-c(:,2)).^2 + ...
        (c(a,3)-c(:,3)).^2) > abs((radius(a,1)-radius(:,1))) | ...
        sqrt((c(a,1)-c(:,1)).^2 + (c(a,2)-c(:,2)).^2 + ...
        (c(a,3)-c(:,3)).^2) == 0 & abs((radius(a,1)-radius(:,1))) == 0;

    radius = radius.*G;
    r = sum(radius(:) == 0);
    [f,~] = find(radius == 0);
```

```
    radius(f,:) = [];
    c(f,:) = [];

    a = a + 1;
    g = g - r;
end

figure(2);
hist(radius);

figure(3);

%Cubic lattice
%plot3(x,y,z,'black');
%hold on

%Sphere command initiator
[x,y,z] = sphere;

%Surface plot of porous medium
%for zz = 1:g;
%    surf(x*radius(zz,1)+c(zz,1), y*radius(zz,1)+c(zz,2),
z*radius(zz,1)+c(zz,3));
%end
%hold off
%% Tessellation

voxel = 248*cx;

%Quantity of cubes per horizontal or vertical row%
cubes = voxel;

%Cube dimensions (granularity)
gr = cx/cubes;
discretization = cubes^3;

%Volume discretization
%x discretization coordinates
A = linspace(gr/2, gr/2 + gr*(cubes - 1), cubes);
vdx = repmat(A', cubes^2, 1);

%y discretization coordinates
B = repmat(A, cubes, 1);
C = B(:);
vdy = repmat(C, cubes, 1);

%z discretization coordinates
D = repmat(A, cubes^2, 1);
vdz = D(:);
%% Palabos Vector

matrix = zeros(discretization,1);
```

```
for grains = 1:g
    G = sqrt((vdx(:)-c(grains,1)).^2+(vdy(:)-c(grains,2)).^2 ...
    +(vdz(:)-c(grains,3)).^2 )<=
ones(discretization,1)*(radius(grains));

    matrix = matrix + G;
end

matrix(matrix >= 1) = 1;
%% Porous Medium Properties

porosity = 1 - (sum(matrix)/discretization);

%Total lattice volume
vt = cx*cy*cz;

%Actual mu and sig values of the porous medium with a 100 percent
%confidence interval.
pdf = lognfit(radius,0);

disp(['grains = ' num2str(g)]);
disp(['porosity = ' num2str(round(porosity,4))]);
disp(['Mu = ' num2str(pdf(1,1))]);
disp(['Sigma = ' num2str(pdf(1,2))]);
%% Data Files

f = num2str(porosity,'%.4f');

saveas(figure(1), strcat('hist_', f(3:6), '_i.fig'));
saveas(figure(2), strcat('hist_', f(3:6), '_f.fig'));
%saveas(figure(3), strcat('0_', f(3:6), '.fig'));
%saveas(figure(3), strcat('0_', f(3:6), '.bmp'));

save(strcat('0_', f(3:6), '.mat'), 'c', 'radius');
save(strcat('matrix_', f(3:6), '.mat'), 'matrix');
save(strcat('x_', f(3:6), '.mat'), 'vdx');
save(strcat('y_', f(3:6), '.mat'), 'vdy');
save(strcat('z_', f(3:6), '.mat'), 'vdz');

close all
end

diary off
```

Illustration 1: Porous medium script

```
clc
clear all

%File reference
f = ['4427'; '3935'; '3515'; '3161'; '2812'; '2543'; '2268'; '2040';
'1827'
    '1663'; '1497'; '1348'; '1227'; '1143'];
f = cellstr(f);

for ii = 1:size(f,1);
    mkdir(strcat('0_', char(f(ii)), 'matrix'))

%% Load Data Set

%Loads the 1's and 0's array yielded from Palabos_Porous_Medium script.
load(strcat('matrix_', char(f(ii))));

%% Reconstruction of 3D Matrix

matrix = transpose(matrix);
matrix = vec2mat(matrix, 248);

M = zeros(248, 248, 248);

%% Construction of 2D image slices for Palabos

for n = 1:248
    M(:,:,n) = matrix((1 + 248*(n-1)):(248 + 248*(n-1)),:);
    M(:,:,n) = flip(M(:,:,n));

    I = mat2gray(M(:,:,n), [1 0]);

    if (n < 10)
      imwrite(I, strcat('0_', char(f(ii)), 'matrix/', 'z0_',
char(f(ii)), 'matrix000', num2str(n), '.bmp'));
    elseif (n < 100)
      imwrite(I, strcat('0_', char(f(ii)), 'matrix/', 'z0_',
char(f(ii)), 'matrix00', num2str(n), '.bmp'));
    else
      imwrite(I, strcat('0_', char(f(ii)), 'matrix/', 'z0_',
char(f(ii)), 'matrix0', num2str(n), '.bmp'));
    end
end

for n = 1:248
    I = mat2gray(squeeze(M(n,:,:)), [1 0]);

    if (n < 10)
```

```
      imwrite(I, strcat('0_', char(f(ii)), 'matrix/', 'x0_',
char(f(ii)), 'matrix000', num2str(n), '.bmp'));
    elseif (n < 100)
      imwrite(I, strcat('0_', char(f(ii)), 'matrix/', 'x0_',
char(f(ii)), 'matrix00', num2str(n), '.bmp'));
    else
      imwrite(I, strcat('0_', char(f(ii)), 'matrix/', 'x0_',
char(f(ii)), 'matrix0', num2str(n), '.bmp'));
    end
end

for n = 1:248
    I = mat2gray(squeeze(M(:,n,:)), [1 0]);

    if (n < 10)
      imwrite(I, strcat('0_', char(f(ii)), 'matrix/', 'y0_',
char(f(ii)), 'matrix000', num2str(n), '.bmp'));
    elseif (n < 100)
      imwrite(I, strcat('0_', char(f(ii)), 'matrix/', 'y0_',
char(f(ii)), 'matrix00', num2str(n), '.bmp'));
    else
      imwrite(I, strcat('0_', char(f(ii)), 'matrix/', 'y0_',
char(f(ii)), 'matrix0', num2str(n), '.bmp'));
    end
end
end
```

Illustration 2: Image slices script

7. References

Alyafei, N., Raeini, A. Q., Paluszny, A., & Blunt, M. J. (2015). A sensitivity study of the effect of image resolution on predicted petrophysical properties. *Transport in Porous Media*, *110*(1), 157–169. http://doi.org/10.1007/s11242-015-0563-0.

Ambegaokar, V., Halperin, B. I., & Langer, J. S. (1971). Hopping conductivity in disordered systems. *Physical Review B*, *4*(8), 2612–2620. http://doi.org/10.1103/PhysRevB.4.2612.

Amer, A. M. & Awad, A. A. (1974). Permeability of cohesionless soils. *J. Geotech. Eng. Div., Am. Soc. Civ. Eng.*, *100*(12), 1309-1316.

Bakke, S. (2002). Process based reconstruction of sandstones and prediction of transport properties. *Transport in Porous Media*, *46*(2), 311–343.

Bakke, S., Øren, P.-E., & A. (1997). 3-D pore-scale modelling of sandstones and flow simulations in the pore networks. *Society of Petroleum Engineers*, *2*(June), 136--149. http://doi.org/SPE 35479.

Beard, D. C., & Weyl, P. K. (1973). Influence of texture on porosity of unconsolidated sands. *AAPG Bulletin*, *57*(2), 349–369. http://doi.org/10.1306/819A4272-16C5-11D7-8645000102C1865D.

Beckingham, L. E., Peters, C. A., W. Um, Jones, K. W., & Lindquist, W. B. (2013). "2D and 3D Imaging Resolution Trade-Offs in Quantifying Pore Throats for Prediction of Permeability." *Advances in Water Resources* 62, Part A: 1 – 12. http://dx.doi.org/10.1016/j.advwatres.2013.08.010.

Berg, R. (1986). *Reservoir sandstones*. Englewood Cliffs, New Jersey: Prentice Hall.

Bhatnagar, P. L., Gross, E. P., & Krook, M. (1954). A model for collision processes in Gases. I. Small amplitude processes in charged and neutral one-component systems. *Phys. Rev.*, *94*(3), 511-525. http://doi.org/10.1103/PhysRev.94.511.

Bjorlykke, K., & Egeberg, P. K. (1992). Quartz cementation in sedimentary basins. *The American Association of Petroleum Geologists*, *77*(9), 1538–1548.

Blunt, M. J. (2001). Flow in porous media - pore-network models and multiphase flow. *Current Opinion in Colloid & Interface Science*, *6*(3), 197–207.

Bosl, W. J., Dvorkin, J., & Nur, A. (1998). A study of porosity and permeability using a Lattice Boltzmann simulation. *Geophysical Research Letters*, *25*(9), 1475–1478. http://doi.org/10.1029/98GL00859.

Brooks, R. H., & Corey, A. T. (1964). Hydraulic properties of porous media. *Hydrology Paper*, *3*, 27.

Brown, G. O. (2002). Henry Darcy and the making of a law. *Water Resources Research*, *38*(7), 1–12. http://doi.org/10.1029/2001WR000727.

Bryant, S., & Blunt, M. (1992). Prediction of relative permeability in simple porous media. *Physical Review A*, *46*(4), 2004–2011.

Bultreys, T., De Boever, W. & Cnudde, V. (2016). "Imaging and Image-Based Fluid Transport Modeling at the Pore Scale in Geological Materials: A Practical Introduction to the Current State-of-the-Art." *Earth-Science Reviews* 155 (April): 93–128. http://doi:10.1016/j.earscirev.2016.02.001.

Burdine, R. H. (1953). Relative permeability calculations from size distribution data. *Trans. Am. Inst. Min. Metall. Pet. Eng.*, *198*, 71-78.

Carman, P. C. (1956). *Flow of gasses through porous media*. New York, New York: Academic Press.

Carrier, W. D. (2003). Goodbye, Hazen; hello, Kozeny-Carman. *Journal of Geotechnical and Geoenvironmental Engineering*, *129*(11), 1054–1056. http://doi.org/10.1061/(ASCE)1090-0241(2003)129:11(1054).

Carsel, R. F., & Parrish, R. S. (1988). Developing joint probability distributions of soil water retention characteristics. *Water Resour. Res.*, *24*, 755-769.

Caubit, C., Hammon, G., Sheppard, A. P., & Øren, P. E. (2009). Evaluation of the reliability of prediction of petrophysical data through imagery and pore network modelling. *Petrophysics*, *50*(4), 322-334.

Cedergren, H. R. (1967). *Seepage, drainage, and flow nets*. New York, New York: Wiley.

Chen, S., & Doolen, G. D. (1998). Lattice Boltzmann method for fluid flows. *Annual Review of Fluid Mechanics*, *30*(1), 329–364.

Cihan, A., Sukop, M. C., Tyner, J. S., Perfect, E., & Huang, H. (2009). Analytical predictions and Lattice Boltzmann simulations of intrinsic permeability for mass fractal porous media. *Vadose Zone Journal*, *8*(1), 187. http://doi.org/10.2136/vzj2008.0003.

Civan, F. (2001). Scale effect on porosity and permeability: Kinetics, model, and correlation. *AIChE Journal*, *47*(2), 1167–1197. http://doi.org/10.1002/aic.690470206.

Coduto, D. P. (1999). *Geotechnical engineering: Principles and practice*. Upper Saddle River, New Jersey: Prentice-Hall.

Coleman, T. F., & Li, Y. (1996). An interior, trust region approach for nonlinear minimization subject to bounds. *SIAM J. Optim.*, *6*, 418-445.

Collins, R. E., & Jordan, J. K. (1961). Porosity and permeability distribution of sedimentary rocks. *Society of Petroleum Engineers*, (212), 27.

Costa, A. (2006). Permeability-porosity relationship: A reexamination of the Kozeny-Carman equation based on a fractal pore-space geometry assumption. *Geophysical Research Letters*, *33*(2), 1–5. http://doi.org/10.1029/2005GL025134.

Daigle, H., & Piña, O. L. (2016). Data report: Permeability, consolidation properties, and grain size of sediments from sites U1420 and U1421, offshore southern Alaska. *Proceedings of the Integrated Ocean Drilling Program*, *341*. http://doi.org/10.2204/iodp.proc.341.201.2016.

Daigle, H., & Reece, J. S. (2014). Permeability of two-component granular materials. *Transport in Porous Media*, (October 2014), 523–544. http://doi.org/10.1007/s11242-014-0412-6.

Darcy, H. (1856). *Les fontaines publiques de la ville de Dijon : Exposition et application des principes à suivre et des formules à employer dans les questions de distribution d'eau*. (V. Dalmont, Ed.).

Das, B. M. (1997). *Advanced soil mechanics*. Washington, D.C.: Taylor & Francis.

Davies, L., & Dollimore, D. (1980). Theoretical and experimental values for the parameter k of suspensions. *Journal of Physics D: Applied Physics*, *13*, 2013–2020.

Ferreol, B., & Rothman, D. H. (1995). Lattice-Boltzmann simulations of flow through Fontainebleu sandstone. *Transport in Porous Media*, *20*(1), 3–20.

Friedman, G. M. (2015). On sorting, sorting coefficients, and the lognormality of the grain-size distribution of sandstones. *The Journal of Geology*, *70*(6), 737–753.

Furnas, C. C. (1929). Flow of gasses through beds of broken solids. *U.S. Bur. Mines Bull.*, *307*, 144.

Gabbana, A. (2015). *Accelerating the D3Q19 Lattice Boltzmann model with OpenACC and MPI*. Umea University.

Gallivan, M. A., Noble, D. R., Georgiadis, J. G., & Buckius, R. O. (1997). An evaluation of the bounce-back boundary condition for Lattice Boltzmann simulations. *International Journal for Numberical Methods in Fluids*, *25*(June 1996), 249–263.

Ghanbarian, B., Daigle, H., Adler, P. M., Berkowitz, B., Al-Raoush, R., Thompson, K., … Esmail, K. (2016). Permeability in two-component porous media: Effective-medium approximation compared with Lattice-Boltzmann simulations. *Vadose Zone Journal*, *15*(2). http://doi.org/10.2136/vzj2015.05.0071.

Guarracino, L. (2007). Estimation of saturated hydraulic conductivity K_s from the van Genuchten shape parameter α. *Water Resources Research*, *43*(11), 15–18. http://doi.org/10.1029/2006WR005766.

Happel, J., & Brenner, H. (1965). *Low Reynolds Number hydrodynamics: With special applications to particulate media*. The Hague, Neatherlands: Martinus Nijhoff Publishers.

Hazen, A. (1892). Some physical properties of sands and gravels, with special reference to their use in filtration. *24th Annual Rep., Massachusetts State Board of Health*, Pub. Doc. No. 34, 539-556.

Hazen, A. (1911). Discussion of 'Dams on sand foundations' by A. C. Koenig. *Trans. Am. Soc. Civ. Eng.*, 73, 199-203.

Hazlett, R. D., Chen, S. Y., & Soll, W. E. (1998). Wettability and rate effects on immiscible displacement: Lattice Boltzmann simulation in microtomographic

images of reservoir rocks. *Journal of Petroleum Science and Engineering*, *20*(3–4), 167–175. http://doi.org/10.1016/S0920-4105(98)00017-5.

Hillel, D. (1971). *Soil and water: Physical principles and processes*. New York, New York: Academic Press.

Hoef, M. a. Van Der, Beetstra, R., & Kuipers, J. a. M. (2005). Lattice-Boltzmann simulations of low-Reynolds-number flow past mono- and bidisperse arrays of spheres: Results for the permeability and drag force. *Journal of Fluid Mechanics*, *528*(2005), 233–254. http://doi.org/10.1017/S0022112004003295.

Holtz, R. D. & Kovacs, W. D. (1981). *An introduction to geotechnical engineering*. Englewood Cliffs, New Jersey: Prentice-Hall.

Katz, A. J., & Thompson, A. H. (1985). Fractal sandstone pores: Implications for conductivity and pore formation. *Phys. Rev. Lett.*, *54*, 1325-1328.

Katz, A. J., & Thompson, A. H. (1987). Prediction of rock electrical conductivity from mercury injection measurements. *Journal of Physical Research*, *92*(6), 599–607. http://doi.org/10.1029/JB092iB01p00599.

Kaviany, M. (1995). *Principles of heat transfer in porous media*. New York, New York: Springer.

Keehm, Y. (2004). Permeability prediction from thin sections: 3D reconstruction and Lattice-Boltzmann flow simulation. *Geophysical Research Letters*, *31*(4), 3–6. http://doi.org/10.1029/2003GL018761.

Koponen, A., Kataja, M., & Timonen, J. (1997). Permeability and effective porosity of porous media. *Physical Review E*, *56*(3), 3319–3325. http://doi.org/10.1103/PhysRevE.56.3319.

Krumbein, W. C., & Monk, G. D. (1942). Permeability as a function of the size parameters of unconsolidated sand. *Petroleum Technology, AIME Tech. Pub. 1492*, *5*(4), 1-11.

Kyan, C. P., Wasan, D. T., & Kintner, R. C. (1970). Flow of single-phase fluids through fibrous beds. *Industrial & Engineering Chemistry Fundamentals*, *9*(4), 596–603. http://doi.org/10.1021/i160036a012.

Lambe, T. W. & Whitman, R. V. (1969). *Soil mechanics*. New York, New York: Wiley.

Leonards, G. A. (1962). Engineering properties of soils. G. A. Leonards, *Foundation engineering* (66-240). New York, New York: McGraw-Hill.

Madden, T. (1976). Random networks and mixing laws. *Geophysics*, *41*(6), 1104–1125. http://library.seg.org/doi/abs/10.1190/1.2035907.

Mansur, C. I., & Kaufman, R. I. (1962). Dewatering. G. A. Leonards, *Foundation engineering* (241-350). New York, New York: McGraw-Hill.

Manwart, C., Aaltosalmi, U., Koponen, A., Hilfer, R., & Timonen, J. (2002). Lattice-Boltzmann and finite-difference simulations for the permeability for three-dimensional porous media. *Physical Review E - Statistical, Nonlinear, and Soft Matter Physics*, *66*(1), 1–11. http://doi.org/10.1103/PhysRevE.66.016702.

Martys, N., & Chen, H. (1996). Simulation of multicomponent fluids in complex three-dimensional geometries by the lattice Boltzmann method. *Physical Review E*, *53*(1), 743–750. http://doi.org/10.1103/PhysRevE.53.743.

Mathavan, G. N., & Viraraghavan, T. (1992). Coalescence/filtration of an oil in water emulsion in a peat bed. *Water Research*, *26*, 91-98.

Meakin, P., & Tartakovsky, A. M. (2009). "Modeling and Simulation of Pore-Scale Multiphase Fluid Flow and Reactive Transport in Fractured and Porous Media." *Reviews of Geophysics* 47 (3). http://doi:10.1029/2008RG000263.

Mehmani, A., & Prodanović, M. (2014). "The Effect of Microporosity on Transport Properties in Porous Media." *Advances in Water Resources* 63 (January): 104–19. http://doi:10.1016/j.advwatres.2013.10.009.

Mavko, G., & Nur, A. (1997). The effect of a percolation threshold in the Kozeny-Carman relation. *Geophysics*, *62*(5), 1480–1482.

Michael, J. K., Edmund, C. S., Pachepsky, Y. A., & Choi, H. (2011). Geometric and hydrodynamic characteristics of three-dimensional saturated prefractal porous media determined with Lattice Boltzmann modeling. *Transport in Porous Media*, *90*(3), 831–846. http://doi.org/10.1007/s11242-011-9818-6.

Mishra, S., & Parker, J. C. (1990). On the relation between saturated conductivity and capillary retention characteristics. *Ground Water*, *28*, 775-777.

Mualem, Y. (1976). A new model for predicting the hydraulic conductivity of unsaturated porous media. *Water Resour. Res.*, *12*, 513-522.

Nasta, P., Vrugt, J. A., & Romano, N. (2013). Prediction of the saturated hydraulic conductivity from Brooks and Corey's water retention parameters. *Water Resources Research*, *49*(5), 2918–2925. http://doi.org/10.1002/wrcr.20269.

Nur, A., & Seeburger, D. A. (1984). A pore space model for rock permeability and bulk modulus. *Journal of Geophysical Research*, *89*(3), 527–536. http://doi.org/10.1029/JB089iB01p00527.

Okabe, H., & Blunt, M. (2005). "Pore Space Reconstruction Using Multiple-Point Statistics." *Journal of Petroleum Science and Engineering* 46 (1–2): 121–37. http://doi:10.1016/j.petrol.2004.08.002.

Øren, P.-E., Bakke, S., & Arntzen, O. J. (1998). Extending predictive capabilities to network models. *SPE Journal*, *3*(December), 324–336. http://doi.org/10.2118/52052-PA.

Pan, C., Luo, L. S., & Miller, C. T. (2006). An evaluation of Lattice Boltzmann schemes for porous medium flow simulation. *Computers and Fluids*, *35*(8–9), 898–909. http://doi.org/10.1016/j.compfluid.2005.03.008.

Pan, C. X., Hilpert, M., & Miller, C. T. (2004). Lattice-Boltzmann simulation of two-phase flow in porous media. *Water Resources Research*, *40*(2), W01501. http://doi.org/10.1029/2003WR002120.

Panda, M. N., & Lake, L. W. (1994). Estimation of single-phase permeability from parameters of particle-size distribution. *American Association of Petroleum Geologists Bulletin*, *78*(7), 1028-1039.

Pape, H., Clauser, C., Iffland, J., (2000). Variation of permeability with porosity in sandstone diagenesis interpreted with a fractal pore space model. *Pure Applied Geophysics*, *157*, 603–619. http://doi.org/10.1007/PL00001110.

Peters, E. J. (2012). *Advanced petrophysics volume1: Geology, porosity, absolute permeability, heterogeneity, and geostatistics* (1st ed.). Austin, Texas: Live Oak Book Company.

Peters, E. J. (2012). *Advanced petrophysics volume 2: Dispersion, interfacial phenomena/wettability, capillarity/capillary pressure, relative permeability* (1st ed.). Austin, Texas: Live Oak Book Company.

Piri, M., & Blunt, M. J. (2005). Three-dimensional mixed-wet random pore-scale network modeling of two- and three-phase flow in porous media. I. Model description. *Physical Review E - Statistical, Nonlinear, and Soft Matter Physics*, *71*(2), 1–30. http://doi.org/10.1103/PhysRevE.71.026301.

Purcell, W. R. (1949). Capillary pressures - their measurement using mercury and the calculation of permeability therefrom. *Journal of Petroleum Technology*, *1*(2), 1949. http://doi.org/10.2118/949039-G.

Rodriguez, E., Giacomelli, F., & Vazquez, A. (2004). Permeability-porosity relationship in RTM for different fiberglass and natural reinforcements. *Journal of Composite Materials*, *38*(3), 259–268. http://doi.org/10.1177/0021998304039269.

Sahimi, M. (2011). *Flow and transport in porous media and fractured rock* (2nd ed.). Weinheim: Wiley-VCH.

Schelle, H., Iden, S. C., Peters, A., & Durner, W. (2010). Analysis of the agreement of soil hydraulic properties obtained from multistep-outflow and evaporation methods. *Vadose Zone J.*, *9*, 1080-1091.

Shah, S. M., Gray, F., Crawshaw, J. P. & Boek, E. S. (2016). "Micro-Computed Tomography Pore-Scale Study of Flow in Porous Media: Effect of Voxel Resolution." *Advances in Water Resources*, Pore scale modeling and experiments, 95 (September): 276–87. http://doi:10.1016/j.advwatres.2015.07.012.

Shan, X., & Chen, H. (1993). Lattice Boltzmann model for simulating flows with multiple phases and components. *Phys. Rev. E.*, *47*(3), 1815-1819. http://doi.org/10.1103/PhysRevE.47.1815.

Shih, C.-H., & Lee, L. J. (1998). Effect of fiber architecture on permeability in liquid composite molding. *Polymer Composites*, *19*(5), 626–639. http://doi.org/10.1002/pc.10136.

Sprunt, E. S., Gilliland, R. E., & Barrett, M. L. (1970). Predicting the permeability of unconsolidated sediments from grain size measurements. *Gulf Coast Association of Geological Societies*, 2, 373–380.

Sukop, M. C., Huang, H., Alvarez, P. F., Variano, E. A., & Cunningham, K. J. (2013). Evaluation of permeability and non-Darcy flow in vuggy macroporous limestone aquifer samples with lattice Boltzmann methods. *Water Resources Research*, *49*(1), 216–230. http://doi.org/10.1029/2011WR011788.

Sukop, M. C., & Thorne, D. T. (2006). *Lattice Boltzmann modeling: An introduction for geoscientists and engineers*. New York, New York: Springer.

Tahmasebi, P., & Sahimi, M. (2013). "Cross-Correlation Function for Accurate Reconstruction of Heterogeneous Media." *Physical Review Letters* 110 (7): 078002. http://doi:10.1103/PhysRevLett.110.078002.

Taylor, D. W. (1948). *Fundamentals of soil mechanics*. New York, New York: Wiley.

Terzaghi, K. & Peck, R. B. (1964). *Soil mechanics in engineering practice* (2nd ed.). New York, New York: Wiley.

Terzaghi, K., Peck, R. B., & Mesri, G. (1996). *Soil mechanics in engineering practice* (3rd ed.). New York, New York: Wiley.

Torskaya, T., Shabro, V., Torres-Verdinn, C., Salazar-Tio, R., & Revil, A. (2014). Grain shape effects on permeability, formation factor, and capillary pressure from pore-scale modeling. *Transport in Porous Media*, *102*(1), 71–90. http://doi.org/10.1007/s11242-013-0262-7.

Valvatne, P. H., Piri, M., Lopez, X., & Blunt, M. J. (2005). Predictive pore-scale modeling of single and multiphase flow. *Transport in Porous Media*, *58*, 23–41. http://doi.org/10.1007/s11242-00405468-2.

van Genuchten, M. T. (1980). A closed-form equation for predicting the hydraulic conductivity of unsaturated soils. *Soil Sci. Soc. Am. J.*, *44*, 892-898.

Wagner, A. J. (2008). *A practical introduction to the Lattice Boltzmann method*. Fargo, North Dakota: North Dakota State University.

Wildenschild, D., & Sheppard, A. P. (2013). "X-Ray Imaging and Analysis Techniques for Quantifying Pore-Scale Structure and Processes in Subsurface Porous Medium Systems." *Advances in Water Resources* 51 (January): 217–46. http://doi:10.1016/j.advwatres.2012.07.018.

Worden, R. H., & Morad, S. (2000). Quartz cementation in sandstones. *The International Association of Sedimentologists*, *29*(Special Publication), 1–36.

Wyllie, M. R. J.; Gregory, A. R. (1955). Fluid Flow through Unconsolidated Porous Aggregates. *Industrial and Engineering Chemistry*, *47*(7) , 1379–1388.

Wyllie, M. R. J., & Rose, W. (1950). Some theoretical considerations related to the quantitative evaluation of the physical characteristics of reservoir rock from electrical log data. *Journal of Petroleum Technology*, *2*(4), 105–118. http://doi.org/10.2118/950105-G.

Xu, P., & Yu, B. (2008). Developing a new form of permeability and Kozeny-Carman constant for homogeneous porous media by means of fractal geometry. *Advances*

in Water Resources, *31*(1), 74–81. http://doi.org/10.1016/j.advwatres.2007.06.003.

Yu, B., & Li, J. (2001). Some fractal characters of porous media. *Fractals*, *9*(3), 365-372.